High-field charge transport and fluctuation phenomena in semiconductors from first principles

Thesis by
Benjamin Henrik James Hatanpää

In Partial Fulfillment of the Requirements for the
Degree of
Doctor of Philosophy

CALIFORNIA INSTITUTE OF TECHNOLOGY
Pasadena, California

2025
Defended September 6, 2024

Benjamin Henrik James Hatanpää
ORCID: 0000-0002-8441-0183

ACKNOWLEDGEMENTS

I would like to start by thanking my advisor, Professor Austin Minnich, for being a constant source of help and feedback. Whenever I had any questions, you would always be there for me, eager to guide me and help me figure them out. I appreciate the time and effort you put in with every student. Thank you to my committee members, Dr. Brent Fultz, Dr. Joseph Falson, and Dr. Linda Ye, for taking the time to review my work. I would also like to thank Dr. Negar Ehsan and everyone at NASA Goddard Space Flight Center for working with me for a few months.

Many different people in my research lab and at Caltech helped me in various ways along this journey. I would like to extend thanks to all of them, especially to Yang, Alex, and Peishi, for being patient with me as I was starting projects and had little to no idea what I was doing. I appreciated the office room talks I had with Jiayin, and the research talks I had with Justin. Extra thanks to Zac and Tomi for always being a source of support and humor throughout the years.

I also want to thank all of the SURF students that I worked with. At first, I wasn't very enthusiastic about the prospect of having to mentor an undergraduate student, but I quickly grew to view it as a positive experience. For being great students and fun to talk to about any topic, I extend my thanks to Anushikha, Dhruv, Juhi, and Ashutosh, and I hope you got something meaningful out of your time at Caltech.

The people who helped me with my jiu-jitsu throughout these years have a special place in my heart. Thank you to Alex for getting me back into it and having me appreciate the more technical aspects of the game. Thank you to Greg, for being so gracious opening your gym to me, and for going against the grain. Special thanks to Isaac, James, and Rehan, for investing a lot of time in me and being great examples for me to try to emulate (maybe not always in life, but certainly in jiu-jitsu). Chris, thanks for the hour-long political talks outside in the parking lot after training. Ian, thanks for giving me rides and always being a willing drilling partner. Winnie, I'll always remember our inside jokes and seeing you go from not training to being a champion. Thanks to everyone I've ever rolled with during my time here, especially the ones that beat me up — there's not a better learning experience out there.

Thank you to my sisters Carolina, Helena, and Rebecca. All of you make me so proud. And lastly, but most importantly, thank you to my parents Heikki and Robin, for always being there for me no matter what.

ABSTRACT

Charge transport and dynamics in semiconductors determine the limits of contemporary high-performance electronic devices. Previously, in order to understand the microscopic mechanisms underlying charge transport, and to efficiently find novel materials for new applications, computational methods were limited to using parameterized scattering rates and simplistic band structure models as inputs. However, with ab-initio methods, only the atomic identities and lattice vectors are needed as inputs. These methods have the capability of providing insights not possible with methods that rely on empirical data, and predicting properties for not-yet-synthesized materials.

While ab-initio computation of low-field transport properties have become common in recent years, these methods have not been extensively applied to non-equilibrium phenomena. In addition, the ab-initio simulation of fluctuational properties (such as the diffusion coefficient or power spectral density of current fluctuations) is an area that has been minimally explored. In order to approach quantum-limited noise levels in devices, a better understanding of the mechanisms that govern electronic noise away from equilibrium is needed.

Thus, motivated by this, the overarching goal of this work is to develop and use first-principles methods to gain insight into the scattering processes that govern high-field electronic transport and noise in well-known semiconductors, and to use the same approach to make predictions and identify promising device applications for novel materials.

The warm electron tensor is a quantity that describes the quadratic change of conductivity with electric field, which provides a quantitative way to examine the heating of the electron gas. However, this has not been examined from first-principles previously. In this work, we report the warm electron tensor of n-Si computed over a large temperature range, and find that the most commonly used order of perturbation theory only captures the qualitative change of the warm electron tensor with angle. However, by including the next-to-leading order two-phonon scattering term in our approach, we find near-quantitative agreement. This finding indicates that two-phonon scattering has a non-negligible role to play in transport in nonpolar semiconductors.

We continue our investigation of n-Si by examining the diffusion coefficient and its

anisotropy by applying our Boltzmann transport framework to fluctuational variables. We find that the qualitative features of the anisotropy are correct, but its magnitude is greatly underestimated in comparison to experimental data, while the onset of the noise is overestimated. While this suggests an incorrect description of f-type scattering in our work, by computing the frequency dependence of the diffusion coefficient as well as the piezoresistivity (two observables sensitive to the balance of f- and g-type scattering), we find that the qualitative agreement of these two observables with experiment shows that such a discrepancy cannot be due to an incorrect description. Instead, we suggest that the experiment contains charge transport phenomena not accounted for by our electron-phonon scattering framework.

Finally, we use the same approach to investigate the high-field transport and noise in the novel ultra-wide-bandgap semiconductor cubic boron nitride (c-BN). While c-BN is known for its excellent mechanical and thermal properties, its high predicted saturation velocity and breakdown field make it a promising candidate in high-power and high-frequency devices. However, very few experimental and theoretical studies have probed its transport properties. Here, we show that c-BN exhibits a negative differential resistance (NDR) region below 140 K, and show that the cause is due to an abrupt valley repopulation effect with applied electric field. We also show that the intervalley time in c-BN is extremely large, on the order of diamond, and that this large intervalley time causes a distinct noise peak, most prominent at low temperatures. We discuss how the NDR region and large intervalley time make c-BN a potential candidate for transferred-electron devices and Gunn oscillators, respectively.

PUBLISHED CONTENT AND CONTRIBUTIONS

[1] Alexander Y. Choi, Peishi S. Cheng, Benjamin Hatanpää, and Austin J. Minnich. Electronic noise of warm electrons in semiconductors from first principles. *Phys. Rev. Materials*, 5:044603, Apr 2021. https://link.aps.org/doi/10.1103/PhysRevMaterials.5.044603
B.H. co-wrote the code used in the manuscript.

[2] Benjamin Hatanpää, Alexander Y. Choi, Peishi S. Cheng, and Austin J. Minnich. Two-phonon scattering in nonpolar semiconductors: A first-principles study of warm electron transport in si. *Phys. Rev. B*, 107:L041110, Jan 2023. https://link.aps.org/doi/10.1103/PhysRevB.107.L041110
B.H. co-designed the research, conducted the calculations, analyzed the data, and wrote the manuscript.

[3] Benjamin Hatanpää and Austin J. Minnich. Hot electron diffusion, microwave noise, and piezoresistivity in si from first principles. *Phys. Rev. B*, 109:235201, Jun 2024. https://link.aps.org/doi/10.1103/PhysRevB.109.235201
B.H. co-designed the research, conducted the calculations, analyzed the data, and wrote the manuscript.

[4] Benjamin Hatanpää and Austin J. Minnich. Valleytronics and negative differential resistance in cubic boron nitride: a first-principles study, 2024. https://arxiv.org/abs/2408.08458
B.H. co-designed the research, conducted the calculations, analyzed the data, and wrote the manuscript.

TABLE OF CONTENTS

LIST OF ILLUSTRATIONS

Number *Page*

Chapter 1

INTRODUCTION

Semiconductor devices are ubiquitous in every aspect of modern technology and used in varied applications, such as solar cells [75], transistors, light-emitting diodes [150], and photodetectors [69]. As device sizes continue to get smaller, and new semiconducting materials are explored for their applications, understanding charge transport in semiconductors is paramount in order to design next-generation devices and identify new materials of interest for varied applications.

In order to accurately describe charge transport in semiconductors, the mechanisms that cause charge carriers to scatter from one electronic state to another must be captured accurately. For many decades, these processes were approximated by analytic forms such as the Brooks-Herring model for ionized-impurity scattering [131], or deformation potential scattering for acoustic phonons [13, 193]. Using these approximations limits the insight we can gain from computations, and prevents these methods from being truly predictive for new materials (as they rely heavily on empirical data). First-principles methods, however, do not rely on empirical data and instead start with a quantum-mechanical description of the system, based on their atomic identities and positions.

In many semiconductors, the dominant scattering mechanism that limits the electric mobility and other properties is scattering between electrons and phonons. Until relatively recently, computing these properties from first-principles was not possible, and these methods have still been rarely applied to problems where an applied electric field drives the electron gas far out of equilibrium. This thesis concerns first-principles computations of transport and noise properties of semiconductors away from equilibrium conditions, and the microscopic insight that is gained from these computations. In addition, this approach is used to investigate the ultrawide-band-gap semiconductor cubic boron nitride, and shows how its properties make it a promising candidate for novel applications. In this chapter, we introduce several key concepts fundamental to the computational approach used in this work, and further outline the central problem we aim to tackle in this work.

1.1 Computing transport properties in semiconductors from first-principles

Electron-phonon interaction

In this work, we only consider scattering between electrons and phonons, ignoring other sources of scattering such as electron-electron scattering, electron-defect scattering, and ionized-impurity scattering. However, for a semiconductor at room temperature that is defect-free (or has a low concentration of defects), it is well known that electron-phonon scattering is the main scattering type that limits the electron mobility [225]. In addition, the electron-phonon interaction is the only one of these scattering types that has been explored to the extent that first-principles predictive methods are widely used. Work on describing other types of scattering from first-principles is a burgeoning area [132, 133], but for simplicity we attempt to only examine systems in this work that are electron-phonon limited. Here, we take a short overview of the electron-phonon interaction. We may start with the Hamiltonian that describes a coupled electron-phonon system [136]:

$$\hat{H} = \sum_{n\mathbf{k}} \epsilon_{n\mathbf{k}} c^{\dagger}_{n\mathbf{k}} c_{n\mathbf{k}} + \sum_{\mathbf{q}\nu} \hbar\omega_{\mathbf{q}\nu} (a^{\dagger}_{\mathbf{q}\nu} a_{\mathbf{q}\nu} + 1/2) + N_p^{-1/2} \sum_{\substack{\mathbf{k},\mathbf{q} \\ mn\nu}} g_{mn\nu}(\mathbf{k},\mathbf{q}) c^{\dagger}_{m\mathbf{k}+\mathbf{q}} c_{n\mathbf{k}} (a_{\mathbf{q}\nu} + a^{\dagger}_{-\mathbf{q}\nu}) \tag{1.1}$$

where $\epsilon_{n\mathbf{k}}$ is the single-particle eigenvalue of an electron with crystal momentum $\mathbf{k}$ with band index n, and $c^{\dagger}_{n\mathbf{k}}$ and $c_{n\mathbf{k}}$ are its associated creation/annihilation operators. $\omega_{\mathbf{q}\nu}$ is the frequency of the lattice vibration with phonon branch index ν and crystal momentum $\mathbf{q}$, and $a^{\dagger}_{\mathbf{q}\nu}$ and $a_{\mathbf{q}\nu}$ its associated creation/annihilation operators. N_p is the number of cells in the Born-von Karman supercell, and $g_{mn\nu}(\mathbf{k},\mathbf{q})$ is the electron-phonon matrix element that describes the strength of the coupling between the electron and phonon subsystems [136]. In Eq. (1.1), the first two terms correspond to the terms for the individual electron and phonon subsystems, while the last line corresponds to the term describing coupling between the electrons and phonons, taken to first order with respect to the atomic displacements [74].

While Eq. (1.1) may look seemingly simple, chief among its difficulties is that there is no prescribed way of calculating the quantities of interest: $\epsilon_{n\mathbf{k}}$, $\omega_{\mathbf{q}\nu}$, and $g_{mn\nu}(\mathbf{k},\mathbf{q})$ [74]. For most of the early history of the electron-phonon coupling problem, various approximations were used for these three quantities [91]. Basic approximations of the first two were simple to obtain, for instance, by approximating the quasiparticle energies with the free electron gas model $\epsilon_{n\mathbf{k}} = \hbar^2\mathbf{k}^2/2m_e - \epsilon_f$, where ϵ_f is the

Fermi energy, and by using the Debye model $\omega_{\mathbf{q}\nu} = v_s|\mathbf{q}|$ for the lattice vibrations (where v_s is the speed of sound in the solid in question). However, obtaining a realistic approximation for the electron-phonon matrix elements $g_{mn\nu}(\mathbf{k}, \mathbf{q})$ proved to be more challenging [74].

The first expression of the electron-phonon matrix element g was done by Bloch, describing scattering from an initial electronic state with wavevector $\mathbf{k}$ to a final state with wavevector $\mathbf{k} + \mathbf{q}$, due to interaction with an acoustic phonon [23]. With modern notation, we may write it as:

$$g_{mn\nu}(\mathbf{k}, \mathbf{q}) = -i\left(\frac{\hbar}{2N_p M_\kappa \omega_{\mathbf{q}\nu}}\right)^{1/2} \mathbf{q} \cdot \mathbf{e}_{\kappa\nu}(\mathbf{q}) V_0 \tag{1.2}$$

Here, m and n are the band indices of $\mathbf{k}$ and $\mathbf{k} + \mathbf{q}$ respectively, $\omega_{\mathbf{q}\nu}$ is the frequency of the phonon with wavevector $\mathbf{q}$ and phonon branch index ν, M_κ is the mass of the κth nucleus, and $e_{\kappa\nu}(\mathbf{q})$ is the polarization of the acoustic wave in question [74].

One of the first computational approaches to tackling the problem of transport in semiconductors was the deformation potential, formalized by Bardeen and Shockley for materials with isotropic bandstructures in 1950 [13, 193]. Due to the fact that most carriers in semiconductors are close in energy to the conduction band minimum, it was assumed that small-wavevector phonons were the dominant electron-phonon scattering mechanism. They showed that the effective potential V_0 needed in Eq. (1.2) can be approximated by:

$$V_0 \rightarrow E_{1,n\mathbf{k}} = \Omega \partial \epsilon_{n\mathbf{k}} / \partial \Omega \tag{1.3}$$

Here, Ω is the volume of the unit cell, and $\epsilon_{n\mathbf{k}}$ are the electron eigenvalues of the conduction band minima or valence band maxima. Generally, these deformation potentials were determined empirically, by fitting to quantities such as the mobility. Later, Dumke improved on this by addressing the common case of anisotropic bandstructures using the effects of shearing deformations [51]. While this method has the obvious drawbacks of relying on empirical data, disqualifying it from being predictive for novel materials or under conditions that materials do not have a wealth of experimental data at, it nevertheless became the dominant way of calculating the electron-phonon interaction for the next decades.

For a long period of time, mainly Monte Carlo methods were used for the computation of transport properties in semiconductors, usually relying on deformation potentials and parametrized band structures. This method was introduced for the

simulation of hot holes in Ge by Kurosawa [118], and was quickly iterated upon and improved [119], investigating hot electron transport in semiconductors such as GaAs [24] and InAs [55]. Further developments were made to this method, such as including a magnetic field in the computation [2, 25], and examining the response to a time-dependent electric field [121, 168, 169].

An approach to solving for hot-electron transport properties that deals with the distribution function f directly has clear advantages over the Monte Carlo method, such as including phenomena that are nonlinear in f such as Fermi degeneracy and electron-electron scattering, and phenomena that are dependent on the low-population tails of f. However, two main obstacles have existed for this approach: the details of the band structure and scattering rates required to achieve computational accuracy may have not been feasible, and the amount of grid points required to represent f (both in grid density and energy window) may have additionally been computationally infeasible [170]. Such an approach dealing directly with f was first developed by Rees, exploiting the stability of the steady state [174, 175], and was used to compute high-field properties in GaAs [176]. However, at this time, the inputs to such a method were still crude — these problems used parabolic bands and deformation potentials as inputs.

With the development of density functional theory to accurately predict electronic band structures, and later density functional perturbation theory to predict lattice dynamics, an ab-initio description of the electron-phonon interaction was more computationally realistic. Recent advances in the first-principles treatment of charge transport in semiconductors have enabled the calculation of the low-field electrical mobility without any adjustable parameters [19, 74]. The method, based on Wannier interpolation of electron-phonon matrix elements [146, 162], allows the Boltzmann equation to be solved on a sufficiently fine grid to ensure converged transport properties. Calculations of low-field mobility have been reported for various semiconductors, including Si [57, 126, 163], GaAs [123, 129, 222], and others [122, 135, 201]. Methodological developments continue to be reported, including an ab-initio treatment of two-phonon scattering [123] and the quadrupole electron-phonon interaction [161]. A recent work has extended these methods to magnetotransport [49], high-field transport [137], and transport and noise of warm and hot electrons in GaAs [40, 43] and holes in Si [35]. We outline the general theory behind the calculations needed in this approach in the following subsections.

Density functional theory

The first step in the ab-initio approach mentioned previously is to compute the electronic band structure (and the crystal structure, if a relaxed lattice constant is used) using density functional theory (DFT). Hohenberg and Kohn in 1964 [92] proposed a formulation that applies to any system of interacting particles (in this case, electrons and fixed nuclei). We can write the Hamiltonian for this problem in the following manner:

$$\hat{H} = -\frac{\hbar^2}{2m_e}\sum_i \nabla_i^2 + \sum_i V_{\text{ext}}(\mathbf{r}_i) + \frac{1}{2}\sum_{i\neq j}\frac{e^2}{|\mathbf{r}_i - \mathbf{r}_j|} \tag{1.4}$$

Here, the first term represents the kinetic energy of the electrons, the second the potential energy due to the field of the fixed nuclei, and the third the electron-electron interaction. The two theorems of Hohenberg and Kohn are as follows. First, for any system of interacting particles subject to an external potential $V_{\text{ext}}(\mathbf{r})$, the ground-state particle density $n_0(\mathbf{r})$ determines uniquely (up to a constant) the potential $V_{\text{ext}}(\mathbf{r})$. It follows that all the properties of the system are determined solely by the ground-state density. Second, a universal functional for the energy $E[n]$ in terms of the density $n(\mathbf{r})$ can be defined that is valid for any external potential $V_{\text{ext}}(\mathbf{r})$, and the ground-state energy is the global minimum value of the functional. In addition, the ground-state density minimizes the functional. As a consequence of this, the functional $E[n]$ is enough to determine both the ground-state energy and density. However, these theorems do not give us any insight into a direct way of solving this many-body problem [138].

In 1965, Kohn and Sham proposed to replace the original many-body problem of Eq. (1.4) with an auxiliary independent-particle (non-interacting) system [112]. It is assumed that the density of the original system is equal to the non-interacting system. This leads to independent particle equations for this non-interacting system that are solvable numerically, thus giving us a way to approach the many-body problem in practice. Using a variational approach, it can be shown that the equations that must be solved are of the form:

$$(H_{\text{KS}}^{\sigma} - \epsilon_i^{\sigma})\psi_i^{\sigma} = 0 \tag{1.5}$$

Here, H_{KS}^{σ} is the effective Hamiltonian, ϵ_i are the Kohn-Sham eigenvalues, ψ_i are the eigenfunctions, and σ is an index representing the spin. The Kohn-Sham effective Hamiltonian is defined as follows (in Hartree atomic units):

$$H_{\text{KS}}^{\sigma}(\mathbf{r}) = -\frac{1}{2}\nabla^2 + V_{\text{KS}}^{\sigma}(\mathbf{r}) \tag{1.6}$$

Here, the Kohn-Sham potential $V^{\sigma}_{\mathrm{KS}}(\mathbf{r})$ is defined as:

$$V^{\sigma}_{\mathrm{KS}} = V_{\mathrm{ext}}(\mathbf{r}) + V_{\mathrm{Hartree}}(\mathbf{r}) + V^{\sigma}_{\mathrm{xc}}(\mathbf{r}) \tag{1.7}$$

where the three contributions correspond to the external potential of the nuclei, the Hartree contribution, and the exchange-correlation potential. It is important to note that the eigenvalues and eigenfunctions of the Kohn-Sham Hamiltonian do not directly correspond to the energies or wavefunctions of the many-body system [138]. However, the approach of interpreting these eigenvalues and eigenfunctions as quasiparticle energies and orbitals has led to wide success in predicting the properties of solids [102, 145].

Density functional perturbation theory

Once we have used DFT to solve for the quasiparticle energies and wavefunctions, the next step is to use density functional perturbation theory (DFPT) in order to solve for the phonon dispersion [16], and in particular for the perturbation potential due to lattice vibrations that is needed for the computation of the electron-phonon matrix elements [223].

Once we have completed the DFPT calculations, we can obtain the electron-phonon matrix elements. They are given by [223] as:

$$g_{mn\nu}(\mathbf{k},\mathbf{q}) = \sqrt{\frac{\hbar}{2\omega_{\nu\mathbf{q}}}} \sum_{\kappa\alpha} \frac{\mathbf{e}_{\kappa\nu\alpha}(\mathbf{q})}{\sqrt{M_\kappa}} \langle \psi_{m\mathbf{k}+\mathbf{q}} | \, \partial_{\mathbf{q},\kappa\alpha} V \, | \psi_{n\mathbf{k}} \rangle \tag{1.8}$$

Here, $|\psi_{m\mathbf{k}+\mathbf{q}}\rangle$ and $|\psi_{n\mathbf{k}}\rangle$ are the final and initial Bloch states obtained from the Kohn-Sham orbitals, and $\partial_{\mathbf{q},\kappa\alpha} V$ is the perturbation potential due to lattice vibrations. In this case, it is computed as the variation of the Kohn-Sham potential V with respect to the atomic displacement of atom κ with mass M_κ along the Cartesian axis α, which is obtained with negligible computational cost after the DFPT calculations are complete [223].

Wannier interpolation

Once the electronic structure is computed with DFT and the phonon dispersion is computed with DFPT, in principle, this is all that is needed to calculate the electron-phonon matrix elements and rates. However, in order to converge transport calculations using the matrix elements as inputs, a dense grid on the order of $100 \times 100 \times 100$ is usually needed. In particular, doing direct DFPT calculations

on such a dense grid is computationally prohibitive. In order to avoid this, Wannier interpolation is used to interpolate the electron-phonon matrix elements on a coarse grid (on the order of $10 \times 10 \times 10$) to a denser grid in a computationally tractable manner [223]. Wannier functions are orthogonal, real-space functions $F(\mathbf{R})$ used to represent a state in reciprocal space $f(\mathbf{q})$ (in this case, the Bloch states). They can be constructed with a unitary transformation from the Bloch states, chosen such that the real-space functions are maximally localized in real space. Due to this localization, $F(\mathbf{R})$ decays rapidly with $|R|$, and starting from this representation we can interpolate $f(\mathbf{q})$ on a much denser grid with computational ease [140].

Boltzmann transport equation

Once the electron-phonon matrix elements are obtained, we can calculate the electron-phonon scattering rates. With these, we are able to solve for observables of the bulk system such as the electron mobility and drift velocity, using the Boltzmann transport equation (BTE). The BTE describes the evolution of a distribution function f of particles, subject to external fields. A general form of the equation can be written as:

$$\frac{\partial f(\mathbf{r}, \mathbf{k}, t)}{\partial t} = \left(\frac{\partial f}{\partial t}\right)_{\text{drift}} + \left(\frac{\partial f}{\partial t}\right)_{\text{coll}} \tag{1.9}$$

Here, the two terms on the right side of the equation represent the effect of applied forces (e.g. an electric or magnetic field), and the effect of internal collision processes (in our case, scattering between electrons and phonons). By considering the drift of the distribution function from a small volume $d\mathbf{k}d\mathbf{r}$ to $d\mathbf{k}'d\mathbf{r}'$ in a time Δt, the drift term can be expanded and the BTE rewritten as:

$$\frac{\partial f(\mathbf{r}, \mathbf{k}, t)}{\partial t} + \frac{\partial f}{\partial \mathbf{r}} \cdot \mathbf{v} + \frac{\partial f}{\partial \mathbf{k}} \cdot \frac{1}{\hbar}\Big(e\mathbf{E} + \mathbf{v} \times \mathbf{B}\Big) = \left(\frac{\partial f}{\partial t}\right)_{\text{coll}} \tag{1.10}$$

Here, we assume the external field are coupled electric and magnetic fields. In this work, we only consider steady-state distributions, so $\partial f/\partial t$ on the left of Eq. (1.10) is set to zero, and by only considering homogeneous systems with no real-space dependence, we may ignore any dependence on $\mathbf{r}$. The chief difficulty in solving the BTE is the description of the collision term. In Section 2.3, we show how starting with Fermi's golden rule and the electron-phonon matrix elements, the collision term can be explicitly obtained for our case of electronic transport.

1.2 Noise in semiconductors

Computations using the ab-initio description of the electron-phonon interaction have mostly been applied to equilibrium observables such as the low-field mobility, and only recently to high-field properties such as drift velocity versus electric field curves. However, these methods have not been applied to the simulation of electronic noise until this work (and by others in the group [35, 40, 200]). Having a better understanding of the microscopic processes that underlie noise in semiconductor devices is crucial in order to progress to lower-noise devices. For instance, the noise performance of high electron mobility transistors (HEMTs), used frequently in radio astronomy and quantum computing applications at cryogenic temperatures, will set the noise floor of the entire device. The noise performance of an amplifier is characterized by its noise temperature, and the theoretical lower limit of such a device is set by quantum mechanics [36]. For instance, this lower bound is 0.3 K at a frequency of 6 GHz. Currently, state-of-the-art devices have a noise temperature approximately 5 to 10 times the quantum limit in the GHz range.

To model noise response in semiconducting devices, the traditional method is to use equivalent circuit models, such as the Pospieszalski model [166]. Here, the behavior of the device at the connecting terminals is represented by circuits of lumped two-terminal elements, representing inductance, capacitance, and resistance [84]. However, this sort of simplistic representation is limiting due to the wide range of complex phenomena that occur in both charge and heat transport in devices. Here, we focus on ab-initio calculations that represent atomistically pure and homogeneous semiconductors. This work will develop greater understanding of the fundamental mechanisms that contribute to noise in these more simplified cases, and then that knowledge can be applied to devices in the future.

We can divide the most important sources of electronic noise in semiconductors into five types; thermal, shot [22], $1/f$ [94], generation-recombination [111], and hot electron noise. The thermal noise is caused by the normal thermal motion of the carriers, and is given at equilibrium by the Nyquist theorem. However, if an electric field biases the distribution far from equilibrium, the electron temperature can be much greater than the lattice temperature and the properties of the noise are highly dependent on the nonequilibrium conditions. In this work, we focus on the description of hot electron noise. In most past works on hot electron fluctuational phenomena in semiconductors, the diffusion coefficient is what is computed or measured. The idea of a diffusion coefficient in electronic transport that is not

necessarily at equilibrium but driven by an electric field was first proposed by Wannier. Price derived that the diffusion coefficient and the power spectral density (PSD) of current fluctuations are linked by a fluctuation-diffusion relation.

When the electric field is small, the diffusion coefficient D is linearly proportional to the electron mobility μ, as given by the Einstein relation:

$$D = \frac{\mu k_B T}{q} \tag{1.11}$$

where T is the temperature and q the electronic charge. However, away from low fields this relation does not apply, as the distribution function is no longer near equilibrium and is not described by the Boltzmann distribution. Instead, a more generalized form for the diffusion coefficient can be derived [170]:

$$D = \frac{1}{2}\frac{d}{dt}\langle (x(t) - \langle x(t)\rangle)^2\rangle \tag{1.12}$$

where $x(t)$ is the position of the particle at time t, and the averages are over an ensemble of histories. This result follows from Fick's law [169]. However, this result is for the zero-frequency diffusion coefficient. To obtain the frequency dependence of the diffusion coefficient, one must utilize the following [84, 194]:

$$D(\omega) = \int_{-\infty}^{\infty} C(t) e^{-i\omega t} dt \tag{1.13}$$

Here, $C(t)$ is the autocorrelation function, defined as [213]:

$$C(t) = \langle \Delta v(t') \Delta v(t'+t)\rangle \tag{1.14}$$

where $\Delta v(t) = v(t) - \langle v(t)\rangle$. To remove the time-dependence of the autocorrelation function, the velocity calculated must be in steady-state.

Similarly to how problems of hot electron transport in semiconductors were solved with Monte Carlo methods chiefly starting in the 1960s, so too were computations of electronic fluctuations in semiconductors. Most often, the diffusion coefficient was the observable in question that was computed. As positional coordinates are easily included in a Monte Carlo scheme, we can easily use Eq. (1.12) for calculations of the diffusion coefficient, for instance. The variation of the diffusion coefficient with electric field was computed in such a manner for many semiconductors, such as GaAs [54, 216], CdTe [173], Si [29, 33, 117], InP [88], and Ge [34]. While these methods used limiting assumptions such as deformation potential scattering for acoustic phonons, dispersionless optical phonons, and simplified (spherical)

band structures, nevertheless reasonable agreement with experiment was obtained in many of these investigations [53, 88, 101, 117, 216].

Simultaneously in the 1960s, Lax's general kinetic theory for fluctuations in a Markovian system [120] was applied by Gantsevich and colleagues to dilute gases whose one-particle distribution function is governed by the linear Boltzmann equation. They showed that for such a system, the spectral density of current fluctuations could be obtained only using solutions of linear Boltzmann equations [66]. Using this general approach, Stanton and Wilkins were able to demonstrate qualitative agreement with experiment in GaAs for both one [197] and two [198] valley systems. However, these works too also relied on experimental parameters such as the measured low-field mobility, valley separation energies, and effective masses.

The limitation of the above approaches lies in their reliance on empirical data and parameterized band structures or scattering rates. By definition, the only materials that can be investigated using such an approach are those that have a wealth of empirical data about their scattering mechanisms. In this work, we use a method to solve for the spectral density of current fluctuations with ab-initio inputs, by solving a linear Boltzmann equation. By doing this, we are able to probe specific phenomena such as intervalley scattering in established semiconductors, as well as being able to examine the noise response of novel materials such as cubic boron nitride. In addition, because fluctuational variables are more sensitive to the exact description of the electronic band structure, phonon dispersion, and scattering rates (for instance), the noise-related aspect of this work serves as a further, more rigorous test of ab-initio methods in semiconductors.

In Fig. 1.1, the computational workflow for the approach that is used in this work is shown. First, the atomic identities and lattice vectors are specified in Quantum Espresso, which is then used to solve for the electronic structure via DFT. DFPT is used to solve for the lattice dynamics, and Perturbo calculates the electron-phonon matrix elements and interpolates them to a fine grid. Once the electron-phonon matrix elements are obtained, we use these to solve the Boltzmann transport equation for the distribution function (for transport observables), and for the fluctuation autocorrelation function (for fluctuational observables).

1.3 Outline of thesis

In this thesis, we show how our first-principles calculations give us insight into both low- and high-field transport phenomena, as well as fluctuational observables, in

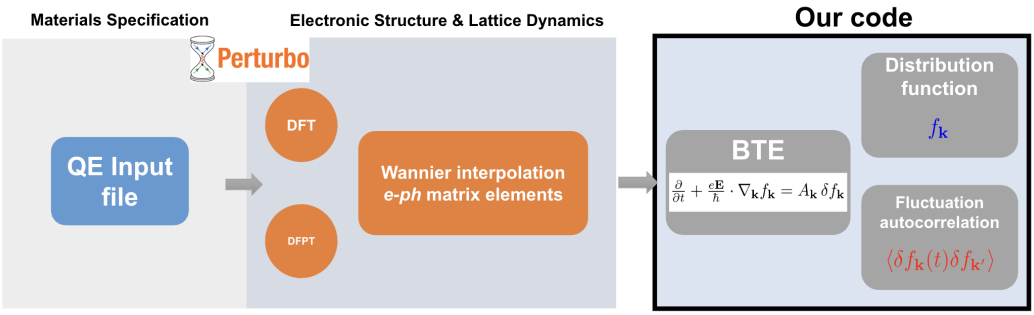

Figure 1.1: Computational workflow showing the approach used in this work. The material is specified by a QUANTUM ESPRESSO input file, which is then used to solve for the electronic structure. After DFPT is used to solve for the lattice dynamics, PERTURBO is used to obtain the Wannier-interpolated electron-phonon matrix elements. Our code then solves the Boltzmann transport equation, for the distribution function (for transport observables), and for the fluctuation autocorrelation function (for fluctuational observables).

both well-researched and novel semiconductors.

In Chapter 2, we demonstrate how our approach is used to solve the Boltzmann transport equation (BTE) for high-field transport properties, and use this approach to solve for the warm electron tensor in n-Si. We show that while the usual one-phonon (1ph) framework captures qualitative changes of the warm electron tensor with angle, including one-electron-two-phonon scattering (2ph) yields near-quantitative agreement. We find that the 2ph rates are comparable in size to the 1ph rates, contradicting conventional wisdom that the 1ph level of theory is sufficient to describe transport properties in nonpolar semiconductors.

Motivated by our results in Chapter 2, we further examine n-Si by focusing on the role of intervalley noise. We show how our BTE solver can also solve for fluctuational properties, and compute the dependence of the hot electron diffusion coefficient on electric field across a wide range of temperatures. We then use the frequency dependence of the diffusion coefficient and the piezoresistivity, two observables that are sensitive to the amount of f-type scattering, to show that an incorrect description of f-type scattering is not sufficient to explain the discrepancy between experiment and computation. This suggests that factors such as space charge effects have a large effect in experiment, indicating that caution must be taken when interpreting measurements of fluctuational variables in terms of charge transport processes.

In Chapter 4, we examine the novel ultra-wide-bandgap semiconductor cubic boron nitride (c-BN) and its high-field transport and noise properties, using the approach

outlined in Chapter 2 and Chapter 3. We find that c-BN demonstrates a distinct negative differential resistance region below 140 K, due to repopulation of inequivalent valleys. This effect may be utilized in transferred-electron devices. We also find that at low fields, the intervalley time in c-BN is on the order of microseconds, indicating that it could be promising in valleytronic applications. We demonstrate that these properties are the cause of the large intervalley noise peak in c-BN, a peak that has not been observed in other materials using our method, and suggest that our predictions may be tested by utilizing noise measurements.

Finally, in Chapter 5 we summarize the findings from the above work, and make suggestions as to avenues for future investigation.

Chapter 2

TWO-PHONON SCATTERING IN NONPOLAR SEMICONDUCTORS: A FIRST-PRINCIPLES STUDY OF WARM ELECTRON TRANSPORT IN SI

This chapter has been adapted, in part, from:

Alexander Y. Choi, Peishi S. Cheng, Benjamin Hatanpää, and Austin J. Minnich. Electronic noise of warm electrons in semiconductors from first principles. *Phys. Rev. Materials*, 5:044603, Apr 2021. https://link.aps.org/doi/10.1103/PhysRevMaterials.5.044603
B.H. co-wrote the code used in the manuscript.

Benjamin Hatanpää, Alexander Y. Choi, Peishi S. Cheng, and Austin J. Minnich. Two-phonon scattering in nonpolar semiconductors: A first-principles study of warm electron transport in si. *Phys. Rev. B*, 107:L041110, Jan 2023. https://link.aps.org/doi/10.1103/PhysRevB.107.L041110
B.H. co-designed the research, conducted the calculations, analyzed the data, and wrote the manuscript.

We have discussed in Chapter 1 how in recent years, the first-principles description of the electron-phonon interaction has become widespread. With this, the ability to calculate macroscopic transport properties has also become common [57, 122, 126, 135, 163, 201, 222]. The accuracy of first-principles theory has been tested primarily by computing the low-field mobility and comparing to the available experimental data at various temperatures and doping concentrations. However, there exists the possibility of cancellation of errors when comparing to drift velocity curves: if the drift velocity is underestimated, but the decrease in drift velocity with field is also underestimated, it can lead to apparent agreement with drift velocity versus field curves. Thus, it is preferable to use a quantitative measure of the change of mobility with field when comparing to experiment. To do this, we can examine the warm electron regime.

The warm electron regime is defined as the regime in which the next-to-leading order term of the expansion of current density with electric field is non-negligible. It is of interest because it contains information on the band structure anisotropy [189] and

energy relaxation [47] not evident in the low-field mobility. The non-Ohmic mobility of Ge and Si beyond the low-field regime was first reported by Shockley [184] and Ryder [183]. Subsequent investigation led to the prediction [192] and experimental observation [73, 79, 104, 106, 187] of the anisotropy of the mobility at high electric field in multi-valley semiconductors owing to the differential heating of transverse and longitudinal valleys, known as the Sasaki-Shibuya effect. In 1963, Schmidt-Tiedemann reported a theory of the warm electron tensor, showing that in cubic crystals the fourth-rank warm electron tensor can be completely described by two independent components owing to crystal symmetry [189]. The two independent components are denoted β and γ, with β describing the variation of conductivity with electric field and γ the non-parallelism of the current and electric field. Substantial experimental data versus temperature and crystallographic direction is available for both β and γ for electrons in Si [28, 73, 78, 106, 108].

Although scattering by the interaction of an electron with one phonon (1ph) has typically been employed in theoretical and Monte Carlo studies at low field and in the warm electron regime to interpret transport studies, [6, 45, 56, 78, 104] other experiments suggest a non-negligible role for higher-order processes [50, 61, 199, 207]. In Si, two-phonon (2ph) deformation potentials were extracted from second-order Raman spectra [177, 206], and calculations of charge transport properties based on these values have indicated that 2ph scattering may make a non-negligible contribution to scattering rates [3, 115, 153]. Recent ab-initio works have reported that two-phonon scattering plays a role in both low-field and high-field transport in the polar semiconductor GaAs [40, 123]. Despite these works, the accepted conclusion from ab-initio studies is that 1ph scattering is sufficient to describe the low-field mobility of non-polar semiconductors [135]. However, this conclusion has not been extensively tested away from the low-field regime.

In this chapter, we report first-principles calculations of the warm electron tensor in Si. At the 1ph level of theory, both the low-field mobility and β are overestimated, with a marked discrepancy of β at 300 K of over a factor of two. To address this discrepancy, we compute the scattering due to sequential 1ph processes, corresponding to one of the terms at second-order in the electron-phonon interaction. The scattering rates are found to be comparable to those of 1ph scattering over a range of energies, and their inclusion eliminates the discrepancy in β. The resulting $\sim$ 20% underestimate of mobility suggests that accounting for cancellations of the two second-order terms of the electron-phonon interaction may be necessary to

achieve quantitative agreement for both the mobility and β.

2.1 Crystal structure and band structure of Si

Silicon (Si) is an elemental semiconductor with the diamond cubic lattice structure. The experimental lattice parameter of Si is 5.43 Å [141]. Once the initial atomic positions and lattice vectors are specified, this is all that is needed for the first-principles analysis contained herein. The band structure of Si is shown in Fig. 2.1. Si is an indirect bandgap semiconductor, with its valence band maximum at Γ, but with its conduction band minimum lying between Γ and X, at approximately $0.85X$. Thus, Si has six equivalent minima in the conduction band. These bands have a longitudinal effective mass of $0.98m_0$, and a transverse effective mass of $0.19m_0$ [7]. We focus on the conduction band here, as we only consider the transport properties of electrons in this work.

One can see how these equivalent valleys with anisotropic effective masses can lead to anisotropy in transport properties away from equilibrium. To illustrate this, we have provided Fig. 2.2. Here, we have shown the valleys oriented along [100] and [010] ([001] omitted for ease of understanding). First, on the left we show a case where the field is oriented along a high-symmetry direction like the [111]. Here, the valleys do not change in their population from equilibrium, and make equal contributions to the drift velocity. However, on the right the field is now oriented along the [100]. The [100] valleys, now parallel to the field direction, present their heavier longitudinal effective mass along this direction, while the [010] valleys have their light transverse effective mass along this direction. This causes the [010] valleys to heat faster, and thus the probability for an electron in a hot (high energy, in red) valley to scatter to a cold (low energy, in blue) valley is higher than than the probability for an electron in a cold valley to scatter to a hot valley, causing a repopulation to the cold valleys along the [100]. This phenomena leads to a drop in the drift velocity in comparison to the case in which the field is applied along a high-symmetry axis. This repopulation effect is key to the anisotropy that is observed in the drift velocity [31], warm electron tensor [79], and diffusion coefficient [29] in n-Si.

One sees in Fig. 2.1 that further up the conduction band, Si possesses six equivalent minima directly at the X point, separated from the conduction band minima by an energy of approximately 135 meV. However, for the temperatures and fields considered in this work, a vast majority of the carriers will remain below this energy,

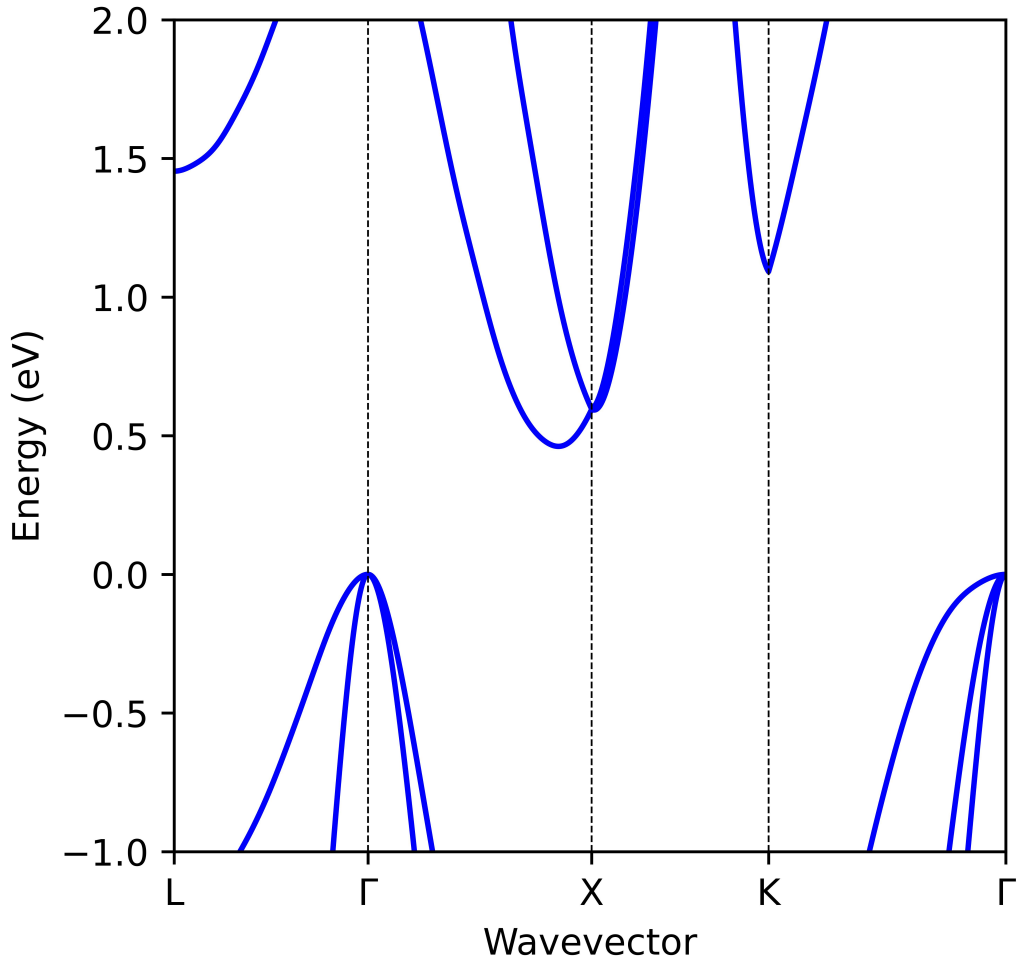

Figure 2.1: Wannier-interpolated band structure of silicon, showing the three highest valence bands and two lowest conduction bands. The conduction band minimum can be seen at 0.85X going from Γ-X, and the split-off bands are shown in the valence band with their maximum at Γ.

and other bands besides the lowest-lying conduction band are not considered.

2.2 The warm electron tensor

The warm electron regime is defined by electric fields for which the cubic term of the expansion of current density with electric field becomes non-negligible [189]. Mathematically, the current density vector **j** in the warm electron regime can be expanded in powers of the electric field of magnitude E as:

$$j_i = E\sigma_0 e_i + E^3 \sigma_{iklm} e_k e_l e_m + \ldots \tag{2.1}$$

where e_i are the components of the unit vector in the direction of the electric field along the Cartesian axis i and σ_{iklm} is the fourth-rank warm electron conductivity

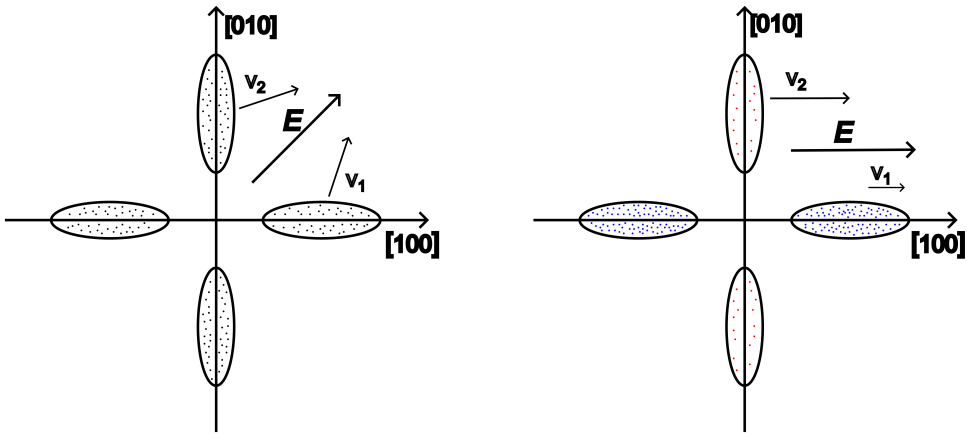

Figure 2.2: Schematic showing how anisotropy in drift velocity of n-Si at high fields occurs due to repopulation from "hot" to "cold" valleys when the electric field is applied along [100] (on the right), in comparison to the case where it is applied along the [111] and valleys are equivalent (on the left).

tensor. As this tensor is invariant under the point group transformations of the crystal lattice, this implies that a set of linear relations between the components of the tensor exist [189]. For cubic crystals with class 23 symmetry, we find that only three linearly independent components exist, by exploiting cyclic permutation properties and that the tensor in this case is invariant under an arbitrary permutation of the last three subscripts. These components are $\sigma_{1111}, \sigma_{1122}$, and σ_{2211}. Furthermore, for the materials we consider in this work, the fourfold axis guarantees complete equivalency of each coordinate axis, making the tensor invariant under arbitrary permutations of all four subscripts. This reduces the number of linearly independent components to just two: σ_{1111} and σ_{1122}. We can define the two variables β and γ in cubic crystals, to fully describe warm electron transport. Here, $\sigma_{1111} = \sigma_0\beta$ and $\sigma_{1122} = \frac{1}{3}\sigma_0(\beta - \gamma)$. Here, β describes the rate change of the conductivity, and γ describes the non-parallelism of the electric field and current density vectors. Equivalently, the warm electron tensor can be specified by the values of β along different crystallographic axes, and that is what is done in this work.

In Fig. 2.3, the experimental setup for measuring β (as well as γ, the non-parallelism) is shown. Here, the electric field is applied to a sample and then rotated, starting from the [001] direction through to the [110] direction. The angle θ measures the angle of the electric field vector and the [001] direction (at 0 deg, the electric field is oriented in the [001] and at 90 deg, the electric field is in the [110]), and the angle

ψ can be used to calculate γ, the non-parallelism of the field. In this work we do not calculate the non-parallelism, but we calculate β along this angle sweep.

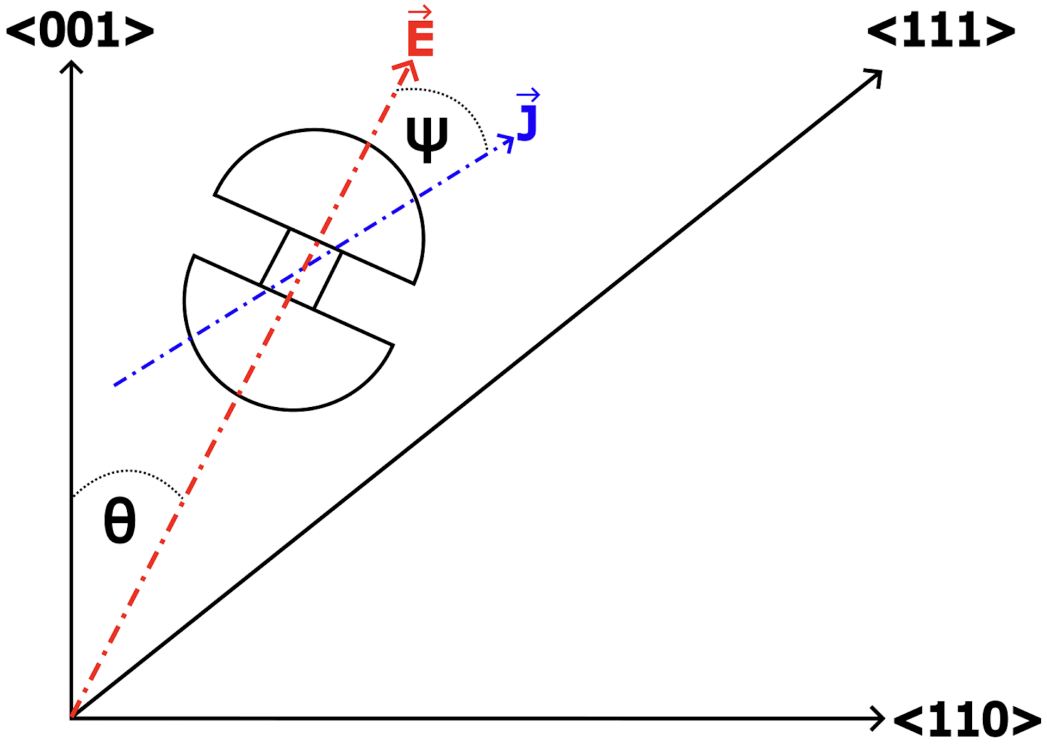

Figure 2.3: Schematic of experimental setup to measure β and γ, used (for instance) in Refs. [106, 189]. The electric field is rotated from the [001] to the [110] direction, and the value of β is recorded at intermediate angles, as well as the non-parallelism γ.

In the same way that the normal low-field conductivity is controlled by the momentum relaxation time τ_m (by "controlled" we mean that frequency dependence of the quantity in question is observed when the frequency ω is comparable to the inverse relaxation time that is relevant for the quantity), for warm electrons β is controlled by the energy relaxation time τ_e (due to the additional time that the electron energy needs to reach a stationary state at a given electric field strength) [100]. This quantity can be defined in a phenomenological way as follows:

$$ev_d E = \frac{\langle\epsilon\rangle - \langle\epsilon\rangle_0}{\tau_e} \tag{2.2}$$

where v_d is the drift velocity, $\langle\epsilon\rangle$ is the mean energy in the presence of the applied electric field, and $\langle\epsilon\rangle$ is the mean energy with no field present [100]. Thus, calculating β gives us additional insight into the relaxation times that govern semiconductor

transport, as opposed to simply calculating the low-field mobility. The warm electron tensor has not been calculated previously by ab-initio methods, but provides a more quantitative comparison between experiment and computation of how the mobility changes with applied electric field. For instance, at a glance computed mobility versus electric field results could closely resemble experimental data, but if the mobility is slightly underestimated but β is slightly underestimated as well, this perceived agreement is misleading.

If the addition of the 2ph rates to the 1ph causes a uniform scaling of the scattering rates by a factor ϵ, β is scaled by ϵ^{-2}, rather than ϵ^{-1}, as is the case for the mobility. However, the 2ph rates generally are not an exact scaling of the 1ph rates. Here, we derive the dependence of the warm electron coefficient β on the scattering rates at different energies, in comparison to the low-field mobility μ. We employ Boltzmann transport theory for charge transport assuming an isotropic crystal and the relaxation time approximation. An electric field is applied along some crystallographic axis, denoted x. Under these assumptions, the Boltzmann transport equation (neglecting real-space and time dependence) is:

$$e\mathcal{E}v_x\frac{\partial f}{\partial E} = -\frac{f - f_0}{\tau(E)} \tag{2.3}$$

The solution of this equation at first order in electric field yields the standard expression for the low-field solution of the Boltzmann equation under the relaxation time approximation:

$$f = f_0 - \tau v_x e\mathcal{E}\frac{\partial f_0}{\partial E} \tag{2.4}$$

from which the following expression for the low-field mobility is obtained [37]:

$$\mu_e = \frac{\frac{e}{3}\int_0^\infty v(E)^2\tau(E)(-\partial f_0/\partial E)D(E)dE}{\int_0^\infty f_0 D(E)dE} \tag{2.5}$$

where $v(E)$ is the magnitude of the group velocity, $\tau(E)$ is the electron relaxation time, f_0 is the equilibrium distribution function, and $D(E)$ is the density of states.

To find an analytic expression for the field-dependent mobility in the form $\mu(E) = \mu_0(1 + \beta\mathcal{E}^2)$ using Eq. 2.5, we replace the equilibrium distribution derivative term $(\partial f_0/\partial E)$ in Eq. 2.5 with the derivative of Eq. 2.4 repeatedly, retaining only terms

of $\mathcal{E}^2$ (terms of order $\mathcal{E}$ are dropped as the final expression for electric current must be odd in electric field). In more detail, if we take the derivative of Eq. 2.4 with respect to E, we get

$$\frac{\partial f}{\partial E} = \frac{\partial f_0}{\partial E} + e\mathcal{E}\frac{\partial}{\partial E}\left(\tau v_x \frac{\partial f_0}{\partial E}\right) \tag{2.6}$$

Plugging in the expansion in Eq. 2.4 again for the second derivative term, we obtain

$$\frac{\partial f}{\partial E} = \frac{\partial f_0}{\partial E} + e\mathcal{E}\frac{\partial}{\partial E}\left(\tau v_x \frac{\partial f_0}{\partial E} + e\mathcal{E}\frac{\partial}{\partial E}\left(\tau v_x \frac{\partial f_0}{\partial E}\right)\right) \tag{2.7}$$

Discarding the terms of order $\mathcal{E}$ due to symmetry, Eq. 2.7 becomes

$$\frac{\partial f}{\partial E} = \frac{\partial f_0}{\partial E} + (e\mathcal{E})^2 \frac{\partial^2}{\partial E^2}\left(\tau v_x \frac{\partial f_0}{\partial E}\right) \tag{2.8}$$

To simplify this expression, we assume that $f_0 \propto e^{-E/kT}$, $v_x \propto \sqrt{E}$ for a parabolic band, and $\tau \propto E^s$. The prefactors for these quantities are lumped into a constant, c_0. Plugging these expressions into Eq. 2.8, we obtain

$$\frac{\partial f}{\partial E} = \frac{\partial f_0}{\partial E} - \left(\frac{c_0}{kT}\right)(e\mathcal{E})^2 \frac{\partial^2}{\partial E^2}\left(E^{s+0.5}e^{-E/kT}\right) \tag{2.9}$$

Carrying out the second derivative with respect to energy E in Eq. 2.9, we obtain

$$\begin{gathered}\frac{\partial f}{\partial E} = \frac{\partial f_0}{\partial E} - \left(\frac{c_0 e^{-E/kT}}{kT}\right) \times (e\mathcal{E})^2 \times \\ \left((s+0.5)(s-0.5)E^{s-1.5} - \left(\frac{2}{kT}\right)(s+0.5)E^{s-0.5} + \left(\frac{1}{kT}\right)^2 E^{s+0.5}\right)\end{gathered} \tag{2.10}$$

We therefore identify an expression for β up to a prefactor as

$$\begin{gathered}\beta \propto \int_0^\infty v(E)^2 \tau(E) e^{-E/kT} \times \\ \left((s+0.5)(s-0.5)E^{s-1.5} - \left(\frac{2}{kT}\right)(s+0.5)E^{s-0.5} + \left(\frac{1}{kT}\right)^2 E^{s+0.5}\right) D(E)dE\end{gathered} \tag{2.11}$$

by the definition of mobility in Eq. 2.5 and gathering the terms at each order of electric field.

This expression can be simplified by substituting the energy dependencies of $v(E)$ and $D(E) \propto \sqrt{E}$ for a parabolic band and the assumed power law form for $\tau(E)$. For the mobility, we obtain

$$\mu_0 \propto \int_0^\infty E^{s+1.5} e^{-E/kT} dE \tag{2.12}$$

For β, we find

$$\begin{gathered}\beta \propto \int_0^\infty e^{-E/kT} \times \\ \left((s+0.5)(s-0.5)E^{2s} - \left(\frac{2}{kT}\right)(s+0.5)\, E^{2s+1} + \left(\frac{1}{kT}\right)^2 E^{2s+2} \right) dE\end{gathered} \tag{2.13}$$

Due to the terms with E^{2s} and E^{2s+1} in the expansion for β, the contribution to the integral from low energies is increased compared to that for the low-field mobility. For instance, for $s < 0$ as occurs for most semiconductors, the leading term in the integrand for β will have a negative exponent, causing β to depend on the low-energy scattering rates to a larger extent compared to the low-field mobility.

2.3 Solving the BTE for charge transport

Here, we will start with the BTE for a case with an applied electric field and no real-space dependency or time dependence (only solving for the steady-state distribution), and show how the BTE can be formulated in terms of a linear system and solved for charge transport observables of interest. For a spatially homogeneous, non-degenerate electron gas subject to an applied electric field, the Boltzmann equation is given by

$$\frac{q\mathbf{E}}{\hbar} \cdot \nabla_{\mathbf{k}} f_{\mathbf{k}} = \mathcal{I}\left[f_{\mathbf{k}}\right] \tag{2.14}$$

Here, the electronic charge is q, the applied electric field is $\mathbf{E}$, $f_{\mathbf{k}}$ is the electron occupation function at wavevector $\mathbf{k}$, and $\mathcal{I}$ is the collision integral that represents how electrons scatter from a state $\mathbf{k}$ to any other state $\mathbf{k}'$. In this work, we do not need to account for interband scattering, so the band index is neglected in the above equation and hence on. In this case, the scattering in the collision integral is solely

due to electron-phonon scattering, which is the dominant form of scattering at high enough temperatures, and at non-degenerate carrier concentrations. Initially, we consider only scattering for processes that involve one electron $\mathbf{k}$ and one phonon $\mathbf{q}$, causing scattering to a new electronic state $\mathbf{k}'$. Later in this work in Chapter 3, we also consider two-phonon scattering where one electron scatters with consecutive one-phonon events.

First, we show how to reduce the collision integral to a linearizable form in terms of the deviational occupation. In general, the collision integral is a nonlinear function of the distribution function, obtained from Fermi's Golden Rule [225]. We can write the collision integral in the following form:

$$\mathcal{I}[f_{\mathbf{k}}] = -\frac{2\pi}{N\hbar}\sum_{\mathbf{q}}\left|g_{\mathbf{k},\mathbf{k}+\mathbf{q}}\right|^2\left(\delta(\epsilon_{\mathbf{k}}-\hbar\omega_{\mathbf{q}}-\epsilon_{\mathbf{k}+\mathbf{q}})H_{\text{em}}+\delta(\epsilon_{\mathbf{k}}+\hbar\omega_{\mathbf{q}}-\epsilon_{\mathbf{k}+\mathbf{q}})H_{\text{abs}}\right) \quad (2.15)$$

Here, N is the total number of $\mathbf{q}$-points, $g_{\mathbf{k},\mathbf{k}+\mathbf{q}}$ is the electron-phonon coupling matrix element that couples an electron state $\mathbf{k}$ to another electron state $\mathbf{k}+\mathbf{q}$ (via emission or absorption of a phonon with wavevector $\mathbf{q}$), $\epsilon_{\mathbf{k}}$ is the energy of the electron state $\mathbf{k}$, $\omega_{\mathbf{q}}$ the frequency of phonon $\mathbf{q}$, and H_{em} and H_{abs} weights that account for the electron and phonon occupations for emission and absorption events, respectively. H_{em} and H_{abs} are nonlinear functions of the electron occupations, defined by

$$\begin{aligned} H_{\text{em}} &= f_{\mathbf{k}}(1-f_{\mathbf{k}+\mathbf{q}})(N_{\mathbf{q}}+1)-(1-f_{\mathbf{k}})f_{\mathbf{k}+\mathbf{q}}N_{\mathbf{q}} \\ H_{\text{abs}} &= f_{\mathbf{k}}(1-f_{\mathbf{k}+\mathbf{q}})N_{\mathbf{q}}-(1-f_{\mathbf{k}})f_{\mathbf{k}+\mathbf{q}}(N_{\mathbf{q}}+1) \end{aligned} \quad (2.16)$$

Here, $N_{\mathbf{q}}$ is the phonon distribution function, which we assume to be in equilibrium and thus given by the Bose-Einstein distribution. In order to solve the BTE as a linear system for the deviational occupation $\Delta f_{\mathbf{k}}$, we define $f_{\mathbf{k}} = f^0_{\mathbf{k}} + \Delta f_{\mathbf{k}}$, where $f^0_{\mathbf{k}}$ is the Fermi-Dirac distribution and $\Delta f_{\mathbf{k}}$ is the deviational occupation. This expansion assumes that the occupations do not change a significant degree from their equilibrium values — valid at equilibrium and in the warm electron region, but not at high electric fields. After substituting this expansion into Eq. (2.16), with a bit of algebra (keeping in mind the definitions of $N_{\mathbf{q}}$ and $f^0_{\mathbf{k}}$) we obtain:

$$\begin{aligned} H_{\text{em}} &= \Delta f_{\mathbf{k}}(N_{\mathbf{q}}-f^0_{\mathbf{k}+\mathbf{q}}+1-\Delta f_{\mathbf{k}+\mathbf{q}})-\Delta f_{\mathbf{k}+\mathbf{q}}(f^0_{\mathbf{k}}+N_{\mathbf{q}}) \\ H_{\text{abs}} &= \Delta f_{\mathbf{k}}(N_{\mathbf{q}}+f^0_{\mathbf{k}+\mathbf{q}}+\Delta f_{\mathbf{k}+\mathbf{q}})-\Delta f_{\mathbf{k}+\mathbf{q}}(1+N_{\mathbf{q}}-f^0_{\mathbf{k}}) \end{aligned} \quad (2.17)$$

By retaining only terms linear in $\Delta f_{\mathbf{k}}$ (terms of the type $\Delta f_{\mathbf{k}} \Delta f_{\mathbf{k+q}}$ can be assumed negligible if the deviational occupations are small, as is true in the low-field regime), this becomes

$$\begin{aligned} H_{\text{em}} &= \Delta f_{\mathbf{k}}(N_{\mathbf{q}} - f^0_{\mathbf{k+q}} + 1) - \Delta f_{\mathbf{k+q}}(f^0_{\mathbf{k}} + N_{\mathbf{q}}) \\ H_{\text{abs}} &= \Delta f_{\mathbf{k}}(N_{\mathbf{q}} + f^0_{\mathbf{k+q}}) - \Delta f_{\mathbf{k+q}}(1 + N_{\mathbf{q}} - f^0_{\mathbf{k}}) \end{aligned} \tag{2.18}$$

This approach is used (and valid) for all computations in this section. However, in Chapter 3, computations are extended to fields up to 10 kV cm^{-1}. For those sections, we note that all concentrations used are non-degenerate, and that the electron occupations $f_{\mathbf{k}}$ (and thus also the deviational occupations $\Delta f_{\mathbf{k}}$) are much less than the phonon occupations $N_{\mathbf{q}}$. Thus, we can take Eq. (2.17) and simplify it, using $f_{\mathbf{k}} \ll 1$ to obtain:

$$\begin{aligned} H_{\text{em}} &= \Delta f_{\mathbf{k}}(N_{\mathbf{q}} + 1) - \Delta f_{\mathbf{k+q}}(N_{\mathbf{q}}) \\ H_{\text{abs}} &= \Delta f_{\mathbf{k}}(N_{\mathbf{q}}) - \Delta f_{\mathbf{k+q}}(1 + N_{\mathbf{q}}) \end{aligned} \tag{2.19}$$

Using the linearization in Eq. (2.19), we can define a scattering matrix Θ, to take the place of the collision integral:

$$\begin{aligned} \mathcal{I}[f_{\mathbf{k}}] = \sum_{\mathbf{k}'} \Theta_{\mathbf{k},\mathbf{k}'} \Delta f_{\mathbf{k}'} = -\frac{2\pi}{N\hbar} \sum_{\mathbf{q}} \left|g_{\mathbf{k},\mathbf{k+q}}\right|^2 \times \\ \big((\delta(\epsilon_{\mathbf{k}} - \hbar\omega_{\mathbf{q}} - \epsilon_{\mathbf{k+q}})(N_{\mathbf{q}} + 1) + \delta(\epsilon_{\mathbf{k}} + \hbar\omega_{\mathbf{q}} - \epsilon_{\mathbf{k+q}})N_{\mathbf{q}})\Delta f_{\mathbf{k}} - \\ ((\delta(\epsilon_{\mathbf{k}} - \hbar\omega_{\mathbf{q}} - \epsilon_{\mathbf{k+q}})N_{\mathbf{q}} + \delta(\epsilon_{\mathbf{k}} + \hbar\omega_{\mathbf{q}} - \epsilon_{\mathbf{k+q}})(N_{\mathbf{q}} + 1))f_{\mathbf{k+q}}) \end{aligned} \tag{2.20}$$

Now that the right hand side of Eq. (2.14) is reduced to matrix form, we tackle the left side. The derivative of the equilibrium occupation function $f^0_{\mathbf{k}}$ with respect to $\mathbf{k}$ can be analytically computed:

$$\nabla_{\mathbf{k}} f^0_{\mathbf{k}} = \frac{df^0_{\mathbf{k}}}{d\epsilon_{\mathbf{k}}} \frac{d\epsilon_{\mathbf{k}}}{d\mathbf{k}} = -\frac{\hbar}{k_B T} \mathbf{v}_{\mathbf{k}} f^0_{\mathbf{k}}(1 - f^0_{\mathbf{k}}) \tag{2.21}$$

However, we must still compute the derivative of the deviational occupation $\Delta f^0_{\mathbf{k}}$ with respect to $\mathbf{k}$. We treat this term numerically with a finite difference approximation using a nearest-neighbors central difference scheme [140, 146]. This reduces the derivative to the form:

$$\nabla_{\mathbf{k}} \Delta f_{\mathbf{k}} = \sum_{\mathbf{b}} w_b \mathbf{b} (\Delta f_{\mathbf{k}+\mathbf{b}} - \Delta f_{\mathbf{k}}) \tag{2.22}$$

Here, $\mathbf{b}$ is the set of vectors that connect the point $\mathbf{k}$ in the Brillouin zone to all of its nearest neighbors, and w_b is a weighting constant for that set of nearest neighbors. To determine the weights and number of nearest-neighbor "shells" that must be used for the set of grid points, the following equation must be satisfied:

$$\sum_{a}^{N} w_a \sum_{i}^{M} b_{\alpha}^{i,a} b_{\beta}^{i,a} = \delta_{\alpha\beta} \tag{2.23}$$

where N is the number of shells required, M is the number of nearest neighbors in the ath shell, w_a is the weight associated with the ath shell, and α and β are Cartesian directions. For a body-centered cubic lattice (which all of the grids used in this work are), one shell is sufficient to satisfy Eq. (2.23), and w_b is equal to $3/8b^2$, where $b = |\mathbf{b}|$. We can write Eq. (2.22) in matrix form, including all prefactors, as

$$\frac{q\mathbf{E}}{\hbar} \cdot \nabla_{\mathbf{k}} \Delta f_{\mathbf{k}} = \sum_{\alpha} \sum_{\mathbf{b}} \frac{qE_\alpha}{\hbar} b_\alpha w_b (\Delta f_{\mathbf{k}+\mathbf{b}} - \Delta f_{\mathbf{k}}) = \sum_{\alpha} \sum_{\mathbf{k}'} \frac{qE_\alpha}{\hbar} D^{\alpha}_{\mathbf{k},\mathbf{k}'} \Delta f_{\mathbf{k}'} \tag{2.24}$$

Here, we define a finite-difference matrix D_α corresponding to the component of the electric field applied in the Cartesian direction α, where $D^{\alpha}_{\mathbf{k},\mathbf{k}'}$ is only nonzero when $\mathbf{k}' = \mathbf{k}$ or when $\mathbf{k}'$ is a nearest neighbor of $\mathbf{k}$, linked by some nearest neighbor vector $\mathbf{b}$ so that $\mathbf{k}' = \mathbf{k}+\mathbf{b}$. As the points in question represent electron states with an energy below some specified energy level, there will be boundary points without a full set of nearest neighbors. In order to account for this, we remove the contributions of these points in the finite difference matrix, while ensuring the column sum of the matrix remains zero (which ensures the sum of $\Delta f_{\mathbf{k}}$ over all $\mathbf{k}$ at any field remains zero). This is a valid assumption, if the population of the boundary points remains negligible.

A simple schematic of how this finite difference process works is shown below in Fig. 2.4, for a case of five points x_i each with a scalar function value $f(x_i)$, where $x_{i+1} - x_i = 1$. The finite difference matrix is pictured on the left, and on the right is the derivative vector. The contribution of the boundary points x_1 and x_5 in the finite difference matrix is nil, ensuring zero column sum of the finite difference matrix. This assumption is valid if $f(x_1), f(x_5) \sim 0$.

$$\begin{bmatrix} 0 & \frac{1}{2} & 0 & 0 & 0 \\ 0 & 0 & \frac{1}{2} & 0 & 0 \\ 0 & -\frac{1}{2} & 0 & \frac{1}{2} & 0 \\ 0 & 0 & -\frac{1}{2} & 0 & 0 \\ 0 & 0 & 0 & -\frac{1}{2} & 0 \end{bmatrix} \begin{bmatrix} f(x_1) \\ f(x_2) \\ f(x_3) \\ f(x_4) \\ f(x_5) \end{bmatrix} = \begin{bmatrix} \frac{f(x_2)}{2} \\ \frac{f(x_3)}{2} \\ \frac{f(x_4)-f(x_2)}{2} \\ -\frac{f(x_3)}{2} \\ -\frac{f(x_4)}{2} \end{bmatrix}$$

Figure 2.4: Schematic of how the finite-difference matrix acts on a 1D chain. Boundary points are not considered in the finite-difference matrix.

Combining Eq. (2.20), Eq. (2.21), and Eq. (2.24), we can rewrite Eq. (2.14) as:

$$-\frac{q\mathbf{E}}{k_B T}\mathbf{v}_{\mathbf{k}} f^0_{\mathbf{k}}(1 - f^0_{\mathbf{k}}) + \sum_{\alpha}\sum_{\mathbf{k}'} \frac{qE_\alpha}{\hbar} D^{\alpha}_{\mathbf{k},\mathbf{k}'} \Delta f_{\mathbf{k}'} = \sum_{\mathbf{k}'} \Theta_{\mathbf{k},\mathbf{k}'} \Delta f_{\mathbf{k}'} \tag{2.25}$$

Rearranging to put the analytic expression by itself on the right side, we obtain:

$$\sum_{\mathbf{k}'} \Big(\sum_{\alpha} \frac{qE_\alpha}{\hbar} D^{\alpha}_{\mathbf{k},\mathbf{k}'} - \Theta_{\mathbf{k},\mathbf{k}'} \Big) \Delta f_{\mathbf{k}'} = \sum_{\mathbf{k}'} \Lambda_{\mathbf{k},\mathbf{k}'} \Delta f_{\mathbf{k}'} = \frac{q\mathbf{E}}{k_B T} \mathbf{v}_{\mathbf{k}} f^0_{\mathbf{k}}(1 - f^0_{\mathbf{k}}) \tag{2.26}$$

Here, we have defined $\Lambda_{\mathbf{k},\mathbf{k}'}$ as a relaxation operator that combines the effects of the scattering and finite difference matrices. As this is now written as a linear system, we can solve for the deviational occupation $\Delta f_{\mathbf{k}}$ as:

$$\Delta f_{\mathbf{k}} = \sum_{\mathbf{k}'} \Lambda^{-1}_{\mathbf{k},\mathbf{k}'} \Big(\frac{q\mathbf{E}}{k_B T} \mathbf{v}_{\mathbf{k}} f^0_{\mathbf{k}}(1 - f^0_{\mathbf{k}}) \Big) \tag{2.27}$$

Once the deviational occupation is obtained, it is simple to calculate transport observables of interest using it (or the new occupation at the field $f_{\mathbf{k}} = f^0_{\mathbf{k}} + \Delta f_{\mathbf{k}}$). For instance, the drift velocity in the β direction can be written as:

$$V_\beta = \frac{1}{N} \sum_{\mathbf{k}} \mathbf{v}_{\mathbf{k},\beta} f_{\mathbf{k}} \tag{2.28}$$

where $N = \sum_{\mathbf{k}} f_{\mathbf{k}}$ is the number of electrons in the Brillouin zone. Similarly, the mobility can be written as:

$$\mu_{\alpha\beta}(\mathbf{E}) = \frac{2e^2}{k_B T \mathcal{V}_0} \sum_{\mathbf{k}} \mathbf{v}_{\mathbf{k},\alpha} \sum_{\mathbf{k}'} \Lambda^{-1}_{\mathbf{k},\mathbf{k}'} (\mathbf{v}_{\mathbf{k}',\beta} f^0_{\mathbf{k}'}) \tag{2.29}$$

where $\mathcal{V}_0$ is the supercell volume, α is the direction along which the current is measured, and β is the direction of the applied electric field [126].

2.4 Two-phonon scattering

As we will show in Section 2.6, including two-phonon scattering in n-Si has a large effect on both the low-field mobility and the warm electron tensor β. Here, we outline our implementation of two-phonon scattering.

First, we examine how the electron-phonon interaction is obtained, by expanding the (self-consistent) one-electron potential $V(\mathbf{r})$ in the phonon-induced displacements $\mathbf{u}_\alpha$ of the ions from their equilibrium position $\mathbf{R}_\alpha$ [110]. We can separate the perturbations that contribute to 2ph scattering into two types. The type that we include in our work is not the bilinear term $H^{(2)}$ (which represents an electron interacting simultaneously with two phonons, resulting from the second derivative of the perturbation potential), but instead the iterated 1ph-process of second order through an intermediate state, written here as $H^{(1,1)} = H^{(1)}(E - H)^{-1}H^{(1)}$. In the long-wavelength (small $\mathbf{q}$) limit for acoustic phonons, due to translational invariance, the contributions of the two types of 2ph scattering cancel out. It has been hypothesized that this cancellation extends to acoustic phonons beyond this limit, but has not been proven. Currently, the bilinear term cannot be computed ab-initio, and is left to future work.

The 2ph scattering rate that we consider is derived in [123] as:

$$\Gamma^{\text{2ph}}_{\mathbf{k}} = \frac{2\pi}{\hbar N^2_\Omega} \sum_{\mathbf{q}} \sum_{\mathbf{p}} \left[\Gamma^{\text{1e1a}} + \Gamma^{\text{2e}} + \Gamma^{\text{2a}} \right] \tag{2.30}$$

where $\mathbf{q}$ and $\mathbf{p}$ are phonons that scatter an electron in a state $\mathbf{k}$ to a new state $\mathbf{k}' = \mathbf{k} + \mathbf{q} + \mathbf{p}$, and for normalization we divide by N^2_Ω, corresponding to the number of $(\mathbf{q}, \mathbf{p})$ points sampled. As we consider only two-phonon scattering consisting of consecutive one-phonon scattering events, we can split the types of scattering into three types as seen in Fig. 2.5. There are scattering events where an electron first absorbs and then emits a phonon (or vice versa) that we define as 1e1a, consecutive

emission events (2e), and consecutive absorption events (2a). We note here that even though any specific 2ph scattering event here will consist of two consecutive 1ph events, the 2ph scattering will couple states that are not coupled with only 1ph scattering, and thus there is reason to believe that the transport properties from such a system will differ from the 1ph case. We can define the individual scattering rate for an electron to scatter from $\mathbf{k}$ to $\mathbf{k}'$ for each type in the following form:

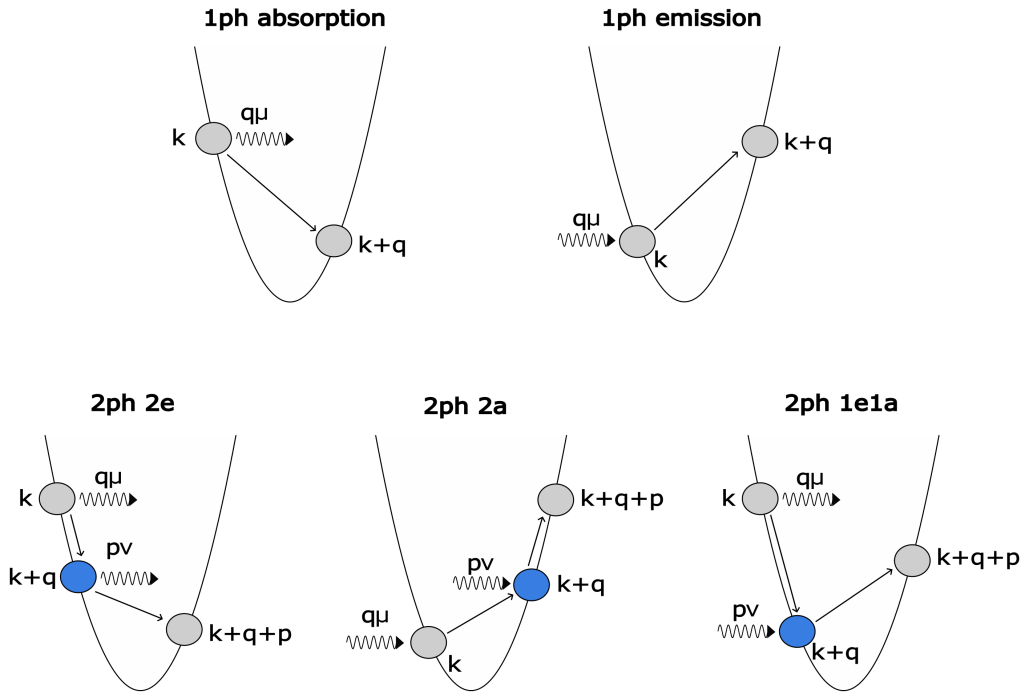

Figure 2.5: On the top row of the figure, schematics for one-phonon absorption and emission processes are shown. On the bottom row, the three types of two-phonon scattering included in this work are shown: two emission events (2e), two absorption events (2a), and one emission/one absorption (1e1a). All of the two-phonon processes are shown are on-shell, as the intermediate state's energy is identical to the band energy.

$$\Gamma^i_{\mathbf{k}} = A^i W^i \delta(\epsilon_{\mathbf{k}} - \epsilon_{\mathbf{k}'} - \alpha^i_{\mathbf{p}} \omega_{\mathbf{p}\mu} - \alpha^i_{\mathbf{q}} \omega_{\mathbf{q}\nu}) \tag{2.31}$$

Here, A^i is a prefactor dependent on the electron and phonon occupations, W^i is the sub-process amplitude, $\omega_{\mathbf{p}\mu}$ is the phonon energy of the phonon with wavevector $\mathbf{p}$ and phonon mode index μ, and α^i takes the values of either 1 or -1 depending on the scattering type:

$$\begin{aligned} \alpha_{\mathbf{p}}^{1e1a} = 1 \quad \alpha_{\mathbf{p}}^{2e} = 1 \quad \alpha_{\mathbf{p}}^{2a} = -1 \\ \alpha_{\mathbf{q}}^{1e1a} = -1 \quad \alpha_{\mathbf{q}}^{2e} = 1 \quad \alpha_{\mathbf{q}}^{2a} = -1 \end{aligned} \tag{2.32}$$

The prefactors A^i are defined in terms of the phonon occupation numbers N (here with mode index suppressed) and electron occupation numbers f as:

$$\begin{aligned} A^{1e1a} &= N_{\mathbf{q}} + N_{\mathbf{q}}N_{\mathbf{p}} + N_{\mathbf{p}}f_{\mathbf{k}'} - N_{\mathbf{q}}f_{\mathbf{k}'} \\ A^{2e} &= \frac{1}{2}\left[(1+N_{\mathbf{q}})(1+N_{\mathbf{p}}-f_{\mathbf{k}'}) - N_{\mathbf{p}}f_{\mathbf{k}'}\right] \\ A^{2a} &= \frac{1}{2}\left[N_{\mathbf{q}}(N_{\mathbf{p}}+f_{\mathbf{k}'}) + (1+N_{\mathbf{p}})f_{\mathbf{k}'}\right] \end{aligned} \tag{2.33}$$

Due to only non-degenerate electron concentrations being considered in this work, we make the assumption similar to Eq. (2.19) that $f_{\mathbf{k}'} \ll 1$ to obtain:

$$\begin{aligned} A^{1e1a} &= N_{\mathbf{q}} + N_{\mathbf{q}}N_{\mathbf{p}} \\ A^{2e} &= \frac{1}{2}\left[(1+N_{\mathbf{q}})(1+N_{\mathbf{p}})\right] \\ A^{2a} &= \frac{1}{2}\left[N_{\mathbf{q}}N_{\mathbf{p}}\right] \end{aligned} \tag{2.34}$$

The sub-process amplitude W^i is given by the following:

$$\left|\left(\frac{g_\nu(\mathbf{k},\mathbf{q})g_\mu(\mathbf{k}+\mathbf{q},\mathbf{p})}{\epsilon_{\mathbf{k}'} - \epsilon_{\mathbf{k}+\mathbf{q}} + \alpha_{\mathbf{p}}^i\omega_{\mathbf{p}\mu} + i\eta - \Sigma_{\mathbf{k}+\mathbf{q}}} + \frac{g_\mu(\mathbf{k},\mathbf{p})g_\nu(\mathbf{k}+\mathbf{p},\mathbf{q})}{\epsilon_{\mathbf{k}'} - \epsilon_{\mathbf{k}+\mathbf{p}} + \alpha_{\mathbf{q}}^i\omega_{\mathbf{q}\nu} + i\eta - \Sigma_{\mathbf{k}+\mathbf{p}}}\right)\right|^2 \tag{2.35}$$

Here, $g_\nu(\mathbf{k},\mathbf{q})$ is the one-phonon scattering matrix element that couples an electron in state $\mathbf{k}$ to another electron in state $\mathbf{k}+\mathbf{q}$ via scattering with a phonon of wavevector $\mathbf{q}$ and phonon index ν, ϵ represents the electron energies, η is an infinitesimal term preventing divergence when the rest of the denominator sums to zero, and $\Sigma_{\mathbf{k}+\mathbf{p}}$ is the self-energy of the intermediate electron state $\mathbf{k}+\mathbf{p}$. Here, the real part of Σ is neglected, as it acts to correct the band structure and does not significantly change the calculation results [123]. The self-energy can be used to obtain the intermediate state lifetime, or its inverse, the scattering rate of the intermediate state, through the relation:

$$\Gamma = \frac{2}{\hbar}\mathrm{Im}\Sigma \tag{2.36}$$

where Γ is the scattering rate of the intermediate state. Thus, we must solve for the self-energy iteratively, as the intermediate state lifetime contains contributions from both 1ph and 2ph scattering in the following manner:

$$|\mathrm{Im}\Sigma| = \frac{\hbar}{2}|\Gamma^{1\mathrm{ph}} + \Gamma^{2\mathrm{ph}}| \tag{2.37}$$

Thus, initially the two-phonon rates are set to zero in Eq. (2.37), and then we solve for Eq. (2.30). This process is repeated until the two-phonon rates do not differ significantly with an additional iteration. Further discussing the intermediate state, we note that the intermediate state does not have to correspond with a band energy. We note that we can categorize intermediate states by their off-shell extents, defined as $\Delta E = E - \epsilon_{\mathbf{k}+\mathbf{p}}$, where E is the energy of the intermediate state reached after an electron in a state $\mathbf{k}$ scatters with a phonon $\mathbf{p}$. We note that by examining Eq. (2.35), we see that the two-phonon scattering amplitude is inversely proportional to the off-shell extent; thus, we expect processes with a large off-shell extent to be negligible in terms of affecting the scattering rates. In this work, we consider two-phonon events with an off-shell extent less than 25 meV; increasing this number in past works did not see a significant change in transport observables [40].

Once the 2ph scattering matrix is computed, it is added to the 1ph scattering matrix, and the same process used in Section 2.3 is used to compute the transport observables of interest.

2.5 Computational details

The electronic structure and electron-phonon matrix elements are computed on a coarse $8 \times 8 \times 8$ grid using DFT and DFPT with Quantum Espresso [72]. We employ a plane wave cutoff of 40 Ryd and a relaxed lattice parameter of 5.431 Å. Once the electronic structure and electron-phonon matrix elements on a coarse grid were computed, they were interpolated on a finer grid of 100^3 using Perturbo. We set the Fermi level 203 meV below the conduction band minimum (CBM) corresponding to a non-degenerate electron gas of concentration of 10^{16} cm^{-3} at 300 K. The energy window of the Brillouin zone was set to 287 meV above the CBM. Increasing the energy window to 447 meV changed the mobility by 0.1% and β by 0.8%, while increasing the grid density to 140^3 resulted in mobility changes on the order of 1%. The final system of linear equations was solved by a Python implementation of the Generalized Minimal Residual (GMRES) method [63].

As in prior work, spin-orbit coupling is neglected as it has a weak effect on electron transport properties in Si [135, 163]. Quadrupole electron-phonon interactions were neglected as they provide only a small correction to the low-field mobility of silicon at room temperature [161].

2.6 Results

Mobility and warm electron tensor

Figure 2.6 shows the computed low-field mobility versus temperature for electrons in Si at the 1ph level of theory. The low-field value at 300 K is 1737 $cm^2V^{-1}s^{-1}$, approximately 20% higher than experimental drift mobility values, which range between 1300 and 1450 $cm^2V^{-1}s^{-1}$ [32, 134, 142, 171]. The calculated value at 300 K is generally consistent with prior ab-initio studies, which report values of 1915 $cm^2V^{-1}s^{-1}$ [135], 1860 $cm^2V^{-1}s^{-1}$ [126], and 1750 $cm^2V^{-1}s^{-1}$ [57]. The use of the experimental lattice constant and GW quasiparticle corrections leads to lower mobility values [163]. The general overestimate of low-field mobility in past ab-initio studies occurs across a wide range of temperatures, as Refs. [126] and [135] show an overestimated mobility from 100 to 300 K.

At higher fields, the mobility decreases below the low-field value owing to electron heating as described by β. Because β depends on the direction of the applied field, we denote β without subscripts to indicate the electric field is applied along the [100] crystallographic axis. In Figure 2.7a, we show the mobility versus electric field in the 1ph framework with the electric field applied in the [100] and [111] crystallographic axes along with the quadratic fit. The quadratic fit is observed to agree well with the calculated values. The coefficient of the quadratic fit yields β. The [100] mobility decreases more rapidly with field than the [111] case, thus yielding a larger value for β_{100} than β_{111}.

In Figure 2.7b we compare the computed β versus temperature with experimental data. The prediction from the 1ph level of theory is clearly larger than the experimental values by around 150% across all temperatures. This discrepancy is markedly larger than that of the low-field mobility. Figures 2.8a and 2.8b show β versus angle between current direction and electric field at 300 and 194 K, respectively. Here, the mobility is presented as the field is rotated from the [001] direction (corresponding to 0°) to the [110] direction (corresponding to 90°). While the qualitative trend in β with field orientation seen in experiment is captured by the 1ph theory, the computed values again are greater than the experimental data by over 100% at both temperatures.

Role of higher-order phonon scattering

Figures 2.7b and 2.8 indicate that β is markedly overestimated at the 1ph level of theory. The magnitude of discrepancy cannot be easily explained by inaccuracies in

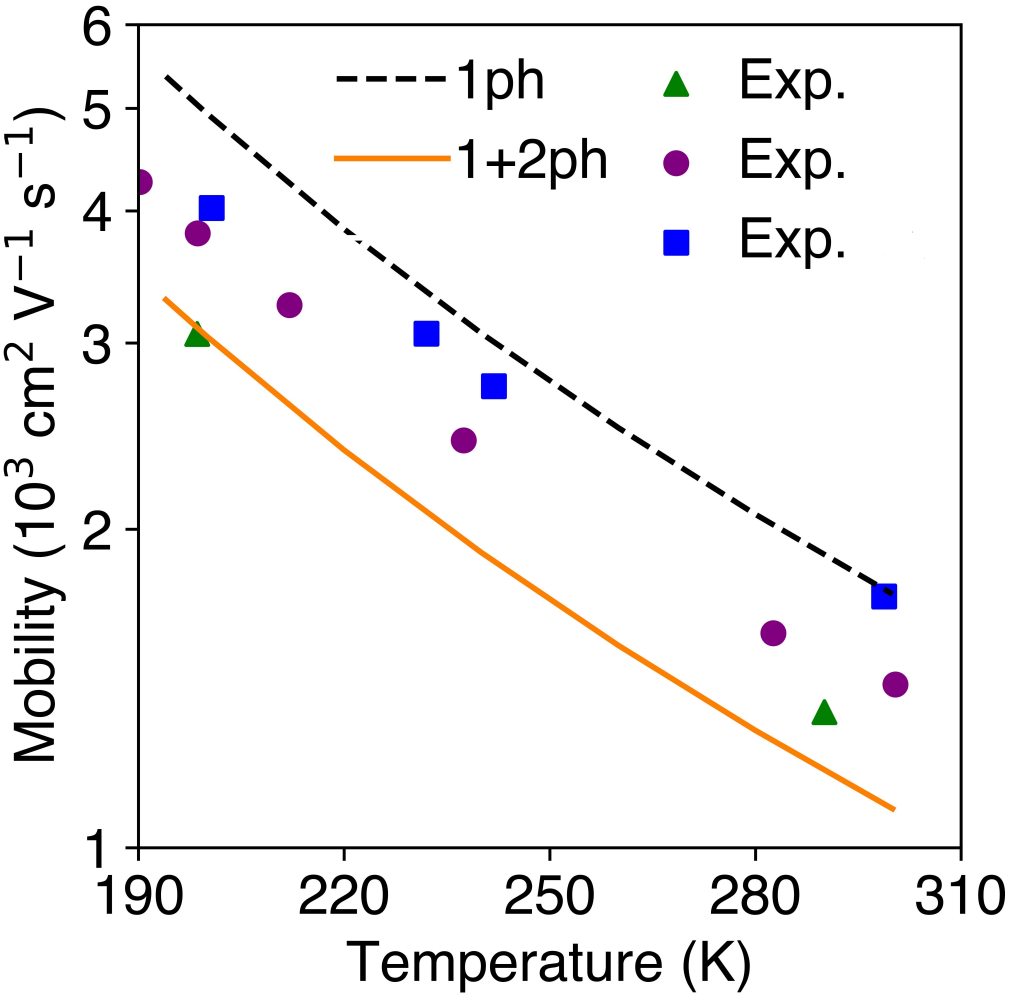

Figure 2.6: Low-field mobility versus temperature for the 1ph (dashed black line) and 1+2ph (solid orange line) frameworks. The mobility is overestimated with the 1ph level of theory, but underestimated when including on-shell 2ph scattering. Experimental data: Figure 11, Ref. [32] (green triangles), Figure 1, Ref. [157] (purple circles), Figure 2, Ref. [130] (blue squares).

band structure, as the discrepancies of the effective mass are $\sim 7\%$. Therefore, we considered whether higher-order phonon scattering processes could account for the poor agreement. The 1ph level of theory accounts for the leading-order electron-phonon scattering process for which electrons scatter with one phonon. We implemented a treatment of the next-to-leading order scattering processes where electrons scatter with two phonons using the ab-initio approach described in Ref. [123]. As in Ref. [40], beyond the low-field regime the full 2ph calculation is presently computationally intractable, and so we included only on-shell 2ph processes that are within 25 meV of a band energy. Despite the neglect of off-shell processes, Ref. [40]

indicates that most of the relevant processes are included with the approximation used here. The 2ph rates were iterated five times.

The computed one and two-phonon scattering rates are shown in Fig. 2.9a. Near the CBM, the 2ph rates are comparable to the 1ph rates. At 100 meV, the maximum energy relevant for transport properties at 300 K, the 2ph rate is approximately 50% of the 1ph rate owing to the weaker energy dependence of 2ph scattering. A disaggregation of the rates into specific emission and absorption processes is shown in Fig. 2.9b. For energies less than 100 meV, the 1e1a (one-phonon emission plus one-phonon absorption) rates are the largest and thus have the largest effect on transport properties, while the 2e (two-phonon emission) rates rise once electrons are able to emit two optical phonons. The 2a (two-phonon absorption) rates are relatively negligible at all energies and are only weakly dependent on energy. These characteristics are qualitatively similar to those reported for GaAs in Refs. [40, 123].

We now examine the impact of the on-shell 2ph rates on the low-field mobility and β. In Figure 2.6, the computed mobility versus temperature including on-shell 2ph scattering is shown. The computed 1+2ph curve underestimates experimental results by about 20%. At 300 K, the low-field mobility is 1089 $cm^2V^{-1}s^{-1}$. In Figure 2.7b, β including on-shell 2ph scattering versus temperature is shown. With the inclusion of on-shell 2ph scattering, good agreement is observed with two independent experimental reports [78, 104]. Similarly, in Figure 2.8a, the agreement with experiment [79] of the dependence of β on orientation angle at 300 K is greatly improved by including on-shell 2ph. The qualitative trend of a decrease in β from 0° until $\sim 55^\circ$ (corresponding to the electric field in the [111] direction), followed by an increase until 90° is unchanged, but it is uniformly decreased in magnitude. The computed β dependence on orientation angle at 194 K shown in Figure 2.8b lies between two data sets [108] of different resistivities.

We now consider the origin of the the improved agreement with β when including on-shell 2ph processes. The first mechanism is the increase in scattering rates, which have a relatively larger effect on β compared to mobility. Specifically, it can be shown that for a uniform scaling of the scattering rates by a factor ϵ, β is scaled by ϵ^{-2} rather than ϵ^{-1} as for the mobility. Therefore, the increased scattering rates contributed by on-shell 2ph processes can account for part of the relatively larger decrease in β. To examine how much of the decrease in β was due to the increased scattering rates, we scaled the 1ph scattering rates by a multiplicative factor so that the resulting low-field mobility was equal to the low-field mobility in the 1+2ph

case. The DC mobility versus electric field and β were then calculated. The scaled 1ph results can be seen in Figure 2.8. At both 300 and 194 K, the majority (94%) of the decrease in β occurs due to the higher scattering rates. However, the calculated values of β with the actual on-shell 2ph scattering rates are still lower than those predicted from the scaled 1ph rates. This further decrease is due to the larger sensitivity of β to the scattering rate at low energies near the CBM compared to that of the mobility (see Section 2.2). At these energies, 2ph processes make a relatively larger contribution to the scattering rates than at higher energies, leading to a larger reduction in β than expected based on a uniform increase in scattering rates.

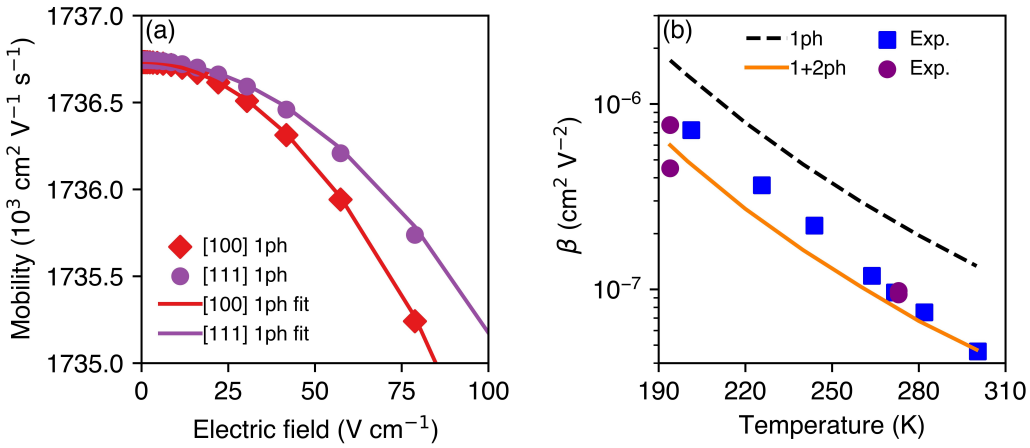

Figure 2.7: a) Mobility versus electric field applied along both the [100] (red diamonds) and [111] (purple circles) crystallographic axes at 300 K using 1ph scattering along with the quadratic fits (solid lines). (b) β versus temperature for the 1ph (dashed black line) and on-shell 2ph (solid orange line) frameworks. β is overestimated by $\gtrsim 100\%$ at the 1ph level of theory across all temperatures. When including on-shell 2ph, the discrepancy is eliminated. Experimental data from Figure 11, Ref. [78] (blue squares) and Figures 3 and 4, Ref. [108] (purple circles).

2.7 Discussion

We now discuss the finding that multi-phonon processes are relevant to transport in non-polar semiconductors. Previous experiment and modeling works have suggested that 2ph processes could account for deviations in the predicted temperature dependence of the mobility from the 1ph deformation potential theory. In particular, two-phonon deformation potentials were extracted from second-order Raman scattering measurements [177, 206], and using these values in transport calculations improved the agreement of both the variation of the low-field mobility and β with temperature [115]. However, these conclusions were subject to uncertainty owing

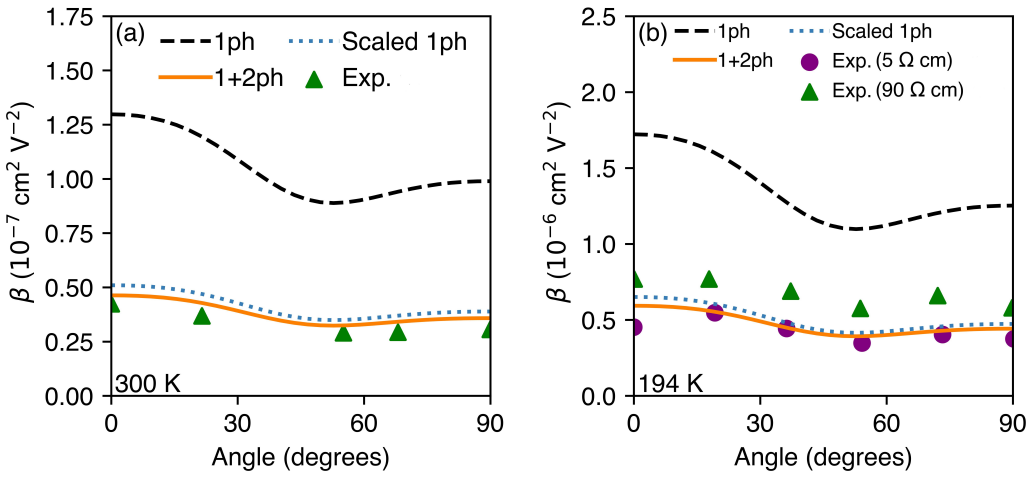

Figure 2.8: (a) β versus electric field orientation angle between the [001] and [110] crystallographic axes at 300 K for the 1ph (dashed black line), scaled 1ph (dotted blue line), and 1+2ph (solid orange line) frameworks. The 1ph theory captures the qualitative dependence of β on angle, but the value is overestimated by $\sim$ 200%. The discrepancy is reduced to $\sim$ 15% with inclusion of on-shell 2ph scattering. Experimental data from Figure 7, Ref. [79] (upward green triangles). (b) Same as (a) at 194 K. Data from Figures 3 and 4, Ref. [108] (purple circles and green triangles).

to the semi-empirical nature of the scattering rates employed in the modeling. The present work overcomes this limitation using the ab-initio scattering rates that are free of adjustable parameters, thereby providing firm evidence that multi-phonon scattering processes are of importance to low-field and warm electron transport in Si.

We additionally consider the role of other multi-phonon processes that have been neglected in the present study and their potential impact on the transport properties. First, the addition of the neglected off-shell 2ph processes will further increase the scattering rates and decrease both the mobility and β; however, Figure 2a of Ref. [40] indicates this difference is negligible in GaAs. A more involved complication is the role of the direct 2ph interaction arising from simultaneous interactions with two phonons, in contrast to that arising from two sequential 1ph scattering events considered here. Due to translational invariance, a cancellation occurs for interactions involving long-wavelength acoustic phonons [93], and it has been posited that this cancellation may extend to acoustic phonons beyond this limit [110]. To estimate the magnitude of this cancellation, we removed all two-

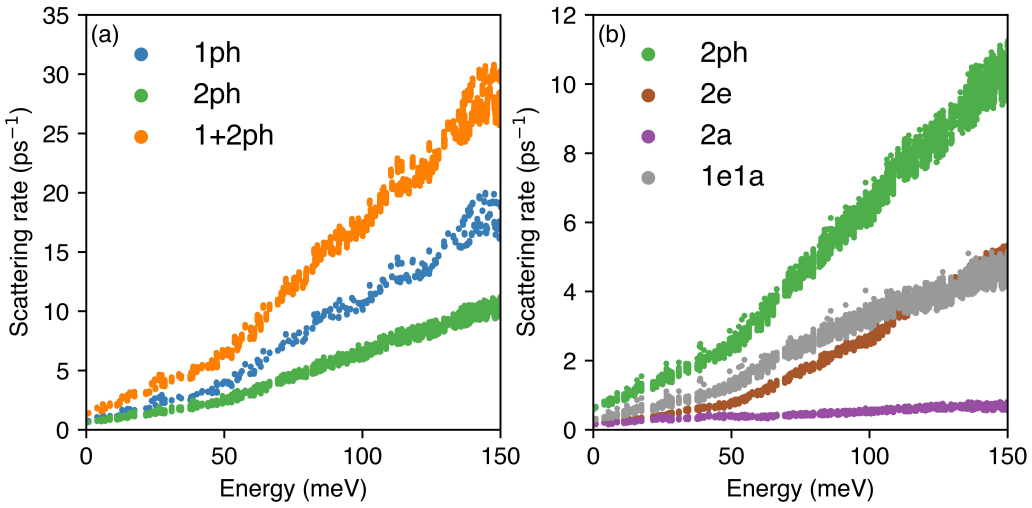

Figure 2.9: (a) Computed 1ph (blue), on-shell 2ph (green), and 1+2ph (orange) scattering rates versus energy at 300 K. The on-shell 2ph rates are approximately 50% of the 1ph rates, indicating a non-negligible contribution to transport properties. (b) Computed on-shell 2ph (green), 2e (brown), 2a (purple), and 1e1a (gray) scattering rates versus energy at 300 K. For energies less than 100 meV, the range relevant to transport properties at 300 K, the 1e1a rates are largest and have the dominant effect on transport properties.

phonon processes that involve acoustic phonons of energy less than 5 meV and recalculated the low-field mobility. The result is 1261 $\mathrm{cm^2V^{-1}s^{-1}}$, which is in near-quantitative agreement with experiment. This result indicates that taking into account the cancellation between the two 2ph vertices may be needed for predictive accuracy. Further tests of the role of multi-phonon processes may be obtained by calculating the free carrier absorption spectrum using the methods of Ref. [155] and the power spectral density of current fluctuations as in Refs. [40, 43].

2.8 Summary

We have presented a first-principles framework for calculating transport properties in semiconductors, starting from the electron-phonon matrix elements, and then using them in the Boltzmann transport equation to solve for the deviational occupation. Using this approach, we obtained the warm electron transport properties of Si. At the 1ph level of theory that is typically regarded as adequate for nonpolar semiconductors, the low-field mobility is overestimated by around 20% while β is overestimated by over 100% across a wide range of temperatures and crystallographic axes. The discrepancy in β is reconciled by inclusion of 2ph scattering, which is found to

exhibit a scattering rate that is comparable to that from 1ph processes. The underestimate of the mobility at this level of theory provides evidence for the occurrence of a non-trivial cancellation of second-order terms in the electron-phonon interaction.

While the importance of multi-phonon processes have been explored in nonpolar semiconductors for phenomena such as magnetophonon resonance [77], the second-order Raman spectrum [177, 206], and the infrared optical absorption [17, 116], very little information exists on their role in transport properties. Our work will stimulate future investigations into the role of multi-phonon processes in transport properties, even in materials in which these processes may have been overlooked in the past.

Chapter 3

HOT ELECTRON DIFFUSION, MICROWAVE NOISE, AND PIEZORESISTIVITY IN SI FROM FIRST PRINCIPLES

This chapter has been adapted, in part, from:

Alexander Y. Choi, Peishi S. Cheng, Benjamin Hatanpää, and Austin J. Minnich. Electronic noise of warm electrons in semiconductors from first principles. *Phys. Rev. Materials*, 5:044603, Apr 2021. https://link.aps.org/doi/10.1103/PhysRevMaterials.5.044603
B.H. co-wrote the code used in the manuscript.

Benjamin Hatanpää and Austin J. Minnich. Hot electron diffusion, microwave noise, and piezoresistivity in si from first principles. *Phys. Rev. B*, 109:235201, Jun 2024. https://link.aps.org/doi/10.1103/PhysRevB.109.235201
B.H. co-designed the research, conducted the calculations, analyzed the data, and wrote the manuscript.

In Chapter 2, we showed how the ab-initio methods that are used to routinely calculate linear transport coefficients such as the electrical mobility of materials [57, 126, 129, 163, 222] can be used to calculate the warm electron tensor, a quantity that characterizes the energy relaxation of the system. High-field transport properties are experimentally accessible as well, but have not been extensively explored with ab-initio methods. One example of such a property are noise properties away from equilibrium, such as the power spectral density (PSD) of current fluctuations [45, 84]. In order to decrease noise in modern electronic devices, a sophisticated understanding of the microscopic transport phenomena and the noise associated with them is required.

One example of a noise phenomena that is present in n-Si is intervalley noise. Intervalley noise, in which carrier number fluctuations between valleys are observable as current fluctuations, can only be observed in a multi-valley semiconductor such as n-Si [84, 167]. The PSD of hot electrons in Si has been experimentally investigated at a range of frequencies, temperature, and electric field strengths. Measurements of the electron diffusion coefficient (proportional to low-frequency PSD) at room

temperature along the [111] direction indicated a pronounced decrease with increasing electric field [33]. A subsequent study at lower temperatures showed an initial increase of the diffusion coefficient with increasing field, followed by the decrease seen at higher temperatures [29]. A clear anisotropy in the diffusion coefficient was observed between the [100] and [111] directions for high electric fields ($\gtrsim$ 2 kV cm^{-1}) across 77 – 300 K [29], despite the cubic symmetry of Si, and was attributed to intervalley noise. The frequency-dependence of the PSD at low temperatures $\sim$ 80 K was also examined, showing how thermal, convective, and intervalley noise contribute at different frequencies for these two directions [15].

Despite extensive experimental investigation, transport and noise properties beyond the low-field regime have historically been evaluated using semi-empirical Monte Carlo methods [29, 99, 101, 165]. These models utilized various approximations, such as dispersionless optical phonons, Debye acoustic phonons, and model band-structures. More recently, the Monte Carlo method in n-Si has been extended to device simulation [1] and full-band studies [58–60, 154]. Computations of high-field transport properties using ab-initio methods have only recently been reported [35, 40, 43, 137, 200]. In GaAs, the drift velocity characteristics up to several kV cm^{-1} have been computed and have provided evidence for the role of two-phonon scattering [40, 200]. The warm electron tensor of n-Si, including two-phonon scattering, has also been computed and directly compared to experiment [86]. An ab-initio formalism to calculate fluctuational properties like PSD has also been developed recently [43]. Previous studies have used the formalism to compute the electric field dependence of the PSD in p-Si [35] and n-GaAs, in the latter case including two-phonon scattering [40, 200]. However, whether ab-initio methods can accurately account for hot electron transport and noise properties in n-Si has not yet been determined.

In this chapter, we report first-principles calculations of the hot electron diffusion coefficient and frequency-dependent PSD in n-Si, including two-phonon scattering. We find that although some qualitative features of the diffusion coefficient are correctly predicted, such as an anisotropy at high electric fields, quantitative agreement is in general poor. To identify the origin of the discrepancies, we computed the microwave-frequency PSD and piezoresistivity. The computed properties are in reasonable qualitative agreement, constraining the magnitude of inaccuracy in the computed intervalley scattering rate. Together, these observations indicate that the diffusion coefficient discrepancies may be attributed to factors which are

not included in the ab-initio formulation of charge transport, for instance real-space gradients and space charge effects. This finding has relevance to the interpretation of diffusion coefficient measurements in terms of microscopic charge transport processes.

3.1 Intervalley noise

To start, we examine the typical anisotropy of the hot-electron diffusion coefficient in n-Si. In Fig. 3.1, experimental data from Ref. [29] for the diffusion coefficient and its dependence on electric field is shown at 200 K, with the electric field applied both in the [111] and [100] directions. We notice that the value of the diffusion coefficient is significantly higher away from equilibrium for the case where the field is applied in the [100] direction, than the [111] case. At a first glance, this might seem surprising — if we examine Eq. (1.11), the equilibrium diffusion coefficient is directly proportional to the mobility. At high fields, it is well-established that the mobility when the field is applied in the [100] is less than when it is in the [111] [31]. However, the diffusion coefficient in the [100] direction is higher than in the [111]. What is the cause of this extra contribution to the diffusion coefficient?

In a multi-valley semiconductor like n-Si, the differential mobility is not equal to the sum of the differential mobilities in each valley weighted by the relative population in each valley. An applied electric field changes the intervalley rates, and thus the relative number of carriers in each valley [84], as seen in Fig. 2.2. Similarly, in a many-valley semiconductor the noise is not equal to the sum of the noise from each individual valley. Due to intervalley transitions causing fluctuations of valley populations, this population fluctuation causes a current fluctuation in the case in which the drift velocities (in the direction of interest) differ. To understand this mechanism, consider the general expression for the intervalley diffusion coefficient D^{int}, given by [29, 167]

$$D^{\text{int}} = n_1 n_2 (v_1 - v_2)^2 \tau_{\text{int}} \tag{3.1}$$

Here, n_1 and n_2 are the fractions of electrons in valleys of type 1 and 2, v_1 and v_2 are the drift velocities in valleys of type 1 and 2, and τ_i is the characteristic intervalley relaxation time. In n-Si, when the field is applied along the high-symmetry [111] direction, all six valleys are oriented equivalently with respect to the electric field direction, and no intervalley diffusion will take place. However, when the field is oriented in the [100] direction, repopulation will occur as shown previously in

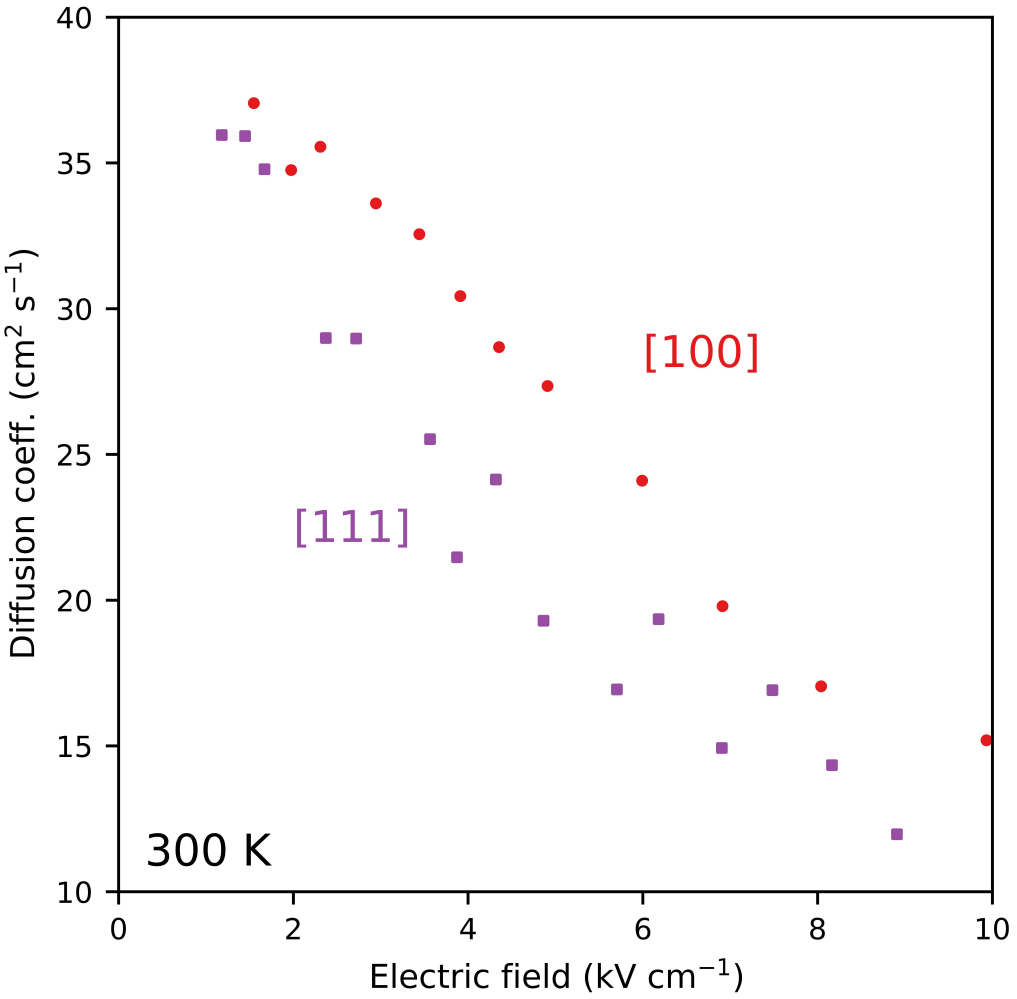

Figure 3.1: Experimental data from Ref. [29] showing the dependence of the diffusion coefficient on electric field in n-Si at 300 K. The electric field is applied in the [111] direction (purple squares) and the [100] direction (red circles).

Fig. 2.2, and the average drift velocities between hot and cold valleys will differ, leading to an additional source of noise. It can be shown that a rough estimate for the ratio of the intensity of intervalley noise to intravalley noise is on the order of

$$\Delta V^2 \tau^{\text{inter}} / \overline{v^2} \tau^{\text{intra}} \tag{3.2}$$

where τ^{inter} and τ^{intra} are the intervalley and intravalley relaxation times, respectively, ΔV is the difference between the drift velocity in a valley compared to the average drift velocity, and v the average drift velocity of the entire system [84]. Thus, if ΔV is large, intervalley noise can be comparable to the "thermal" noise, especially as the intervalley time is already greater than the intravalley time. One can intuit that this

is true if we assume that if an electron is in a state $\mathbf{k}_1$ in valley 1 and then is scattered to a state $\mathbf{k}_2$ into valley 2 via a phonon $\mathbf{q}$, the absolute value of the difference $|\mathbf{k_1} - \mathbf{k_2}|$ is on the order of a_0^{-1}, where a_0 is the lattice parameter of the crystal. The energy of the intervalley phonon $\hbar\omega_{\mathbf{q}}$ is thus on the order of $k_B\Theta_D$, where Θ_D is the Debye temperature. In general, and especially at temperatures less than Θ_D, the energies of phonons that are emitted or absorbed are on average much less $k_B\Theta_D$; that is to say, before an electron scatters to another valley, it changes its energy and momentum multiple times through intravalley scattering events [111]. Thus, $\tau^{\text{inter}} \gg \tau^{\text{intra}}$ holds. Intervalley noise has been observed not only experimentally in many different bulk semiconductors [29, 64], but it has been posited to be a contributor to the drain noise in GaAs FETs [10, 64] and Si MOSFETs [87]. Thus, gaining a quantitative understanding of intervalley noise and being able to predict it accurately in semiconductors is vital.

3.2 E- and ω-noise spectroscopy

Two of the most common experimental techniques to investigate hot-electron noise in semiconductors are $\mathbf{E}-$ and ω-spectroscopy (the electric field and frequency dependence of the noise). In this work, all data of the electric field versus the noise is taken at low frequencies. By measuring the electric field dependence of the noise, we can probe intervalley noise by measuring the noise in different directions, and investigate the balance between increasing scattering rates and increasing energy as the electric field is applied. To illustrate this, we can investigate a version of the Einstein relation in Eq. (1.11), modified for high fields:

$$D(E) = \frac{2}{3}\mu(E)\frac{\langle\epsilon\rangle}{e} \tag{3.3}$$

Here, $D(E)$ is the field-dependent diffusion coefficient, $\mu(E)$ is the electric field-dependent mobility and $\langle\epsilon\rangle$ the average electron energy [29, 100]. As an electric field is applied, this increases the average electron energy. High-energy states tend to contribute more to the diffusion coefficient, and thus raise its value. However, the effect of the electric field also tends to increase the average scattering rate, which damps out fluctuations (and lowers the mobility). Thus, the balance of these two behaviors will determine the energy dependence of the noise. This relation is not exact, but illustrative of the main mechanisms that cause changes in the noise.

A schematic is shown in Fig. 3.2 that illustrates the frequency dependence of the noise for a multi-valley semiconductor. We note that other noise sources such as

$1/f$ noise and generation-recombination noise are not considered in this work, and thus their effects are not pictured in Fig. 3.2. At equilibrium, it is expected that the noise follows the Nyquist-Johnson equation, and the frequency dependence is given by a Lorentzian characterized by the momentum relaxation time.

However, away from equilibrium in a current-carrying state, other types of fluctuations taking place in the system can reveal themselves. One example is the convective noise contribution, that is characterized by the exchange of energy between electrons and the lattice rather than momentum. When an electric field is applied, there is an energy gain from the field acting upon existing current fluctuations: $\delta\epsilon_{\mathbf{E}} \sim \delta\mathbf{j}\cdot\mathbf{E}$. In a semiconductor with a sublinear current-voltage characteristic, due to the decrease in mobility with increasing energy, the fluctuations will tend to reduce the intensity of current fluctuations. When the PSD approaches the inverse energy relaxation time, an increase in the noise will be seen as this contribution rolls off [84].

In addition, as shown in Eq. (3.1), when the electric field is oriented in a manner that creates valleys with inequivalent average drift velocities, an intervalley term is present. The intervalley relaxation time is generally assumed to be large compared to both the energy and momentum relaxation times, and thus the intervalley contribution rolls off at lower frequencies. This contribution is always positive. Thus, in Fig. 3.2, the blue curve is shifted up significantly at lower frequencies with respect to the red curve, and the intervalley contribution rolls off at the lowest frequencies. As the source of any particular noise contribution characterized by a relaxation process with time τ will be cut off at the frequency $\omega\tau \sim 1$, the relaxation times can be estimated from the frequency dependence.

3.3 F-type scattering, noise and piezoresistivity

We can separate intervalley scattering into two types: g-type (between valleys on the same Cartesian axis), and f-type (between valleys not on the same axis). The difference between the two types is visually depicted in Fig. 3.3. While most transport properties such as mobility are insensitive to the balance between f- and g-type scattering, τ_{int}, and thus D^{int}, is inversely proportional to the square of the f-type coupling constant [29].

This can be understood intuitively through the following argument. If we consider a group of electrons at $x, y, z = (0, 0, 0), t = 0$, as t increases due to intervalley scattering, electrons will scatter from one type of valley to the other, and thus at one time they will have drift velocity v_1 and then after scattering into another valley v_2.

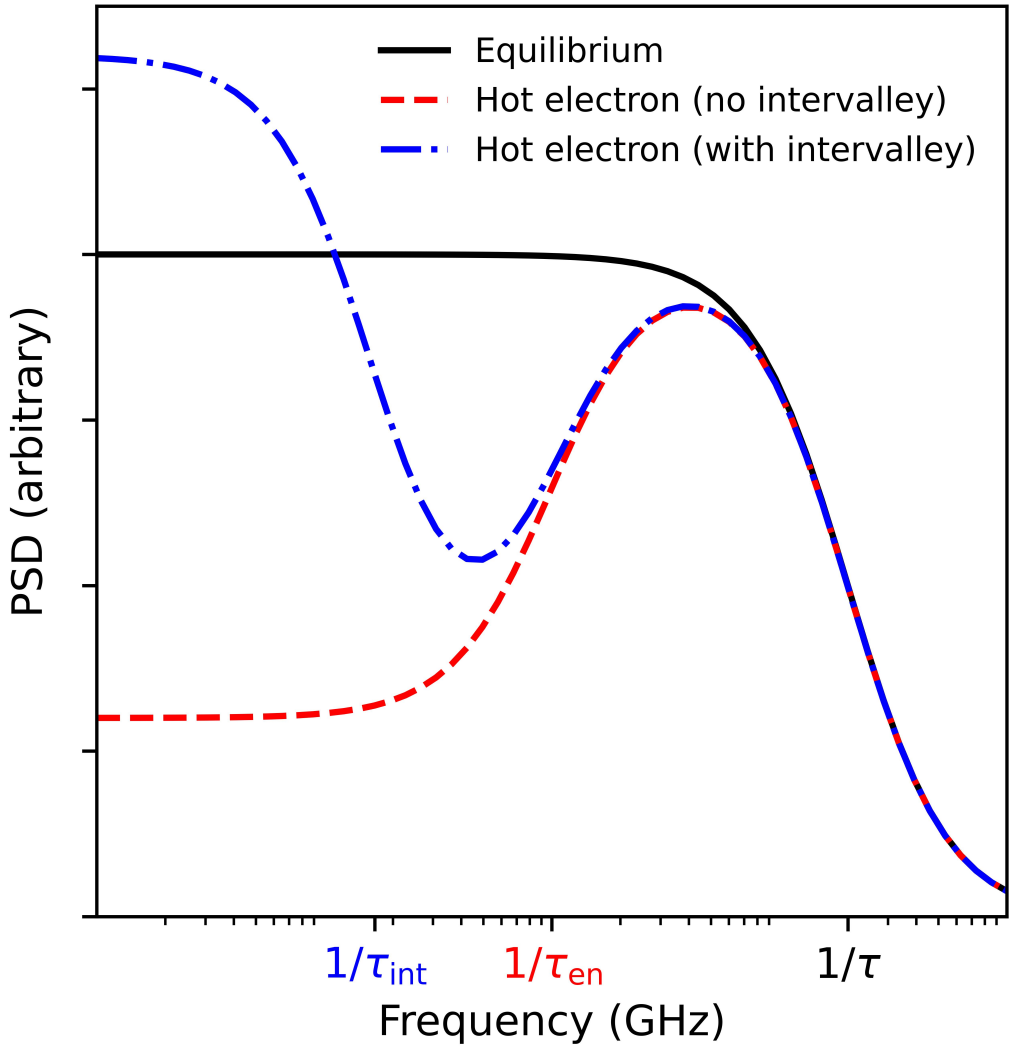

Figure 3.2: Schematic frequency dependence of the PSD in a typical semiconductor at (a) equilibrium, (b) away from equilibrium, where the electric field is oriented along a high-symmetry axis, and (c) away from equilibrium, where valleys are inequivalent.

The stronger f-type scattering is, the more electrons will scatter from one valley to another, so on the aggregate each electron will not differ greatly to others in terms of average drift velocity. Thus, the electron cloud will be less spread (smaller diffusion coefficient). However if f-type scattering is completely eliminated, electrons in two valleys will indefinitely separate from each other, with a mean-squared displacement proportional to t^2. If this is the case, we then lose the linear relation between M and t necessary for the definition of D in Eq. (1.12) [29].

Historically, electron transport in Si initially was evaluated with Monte Carlo models,

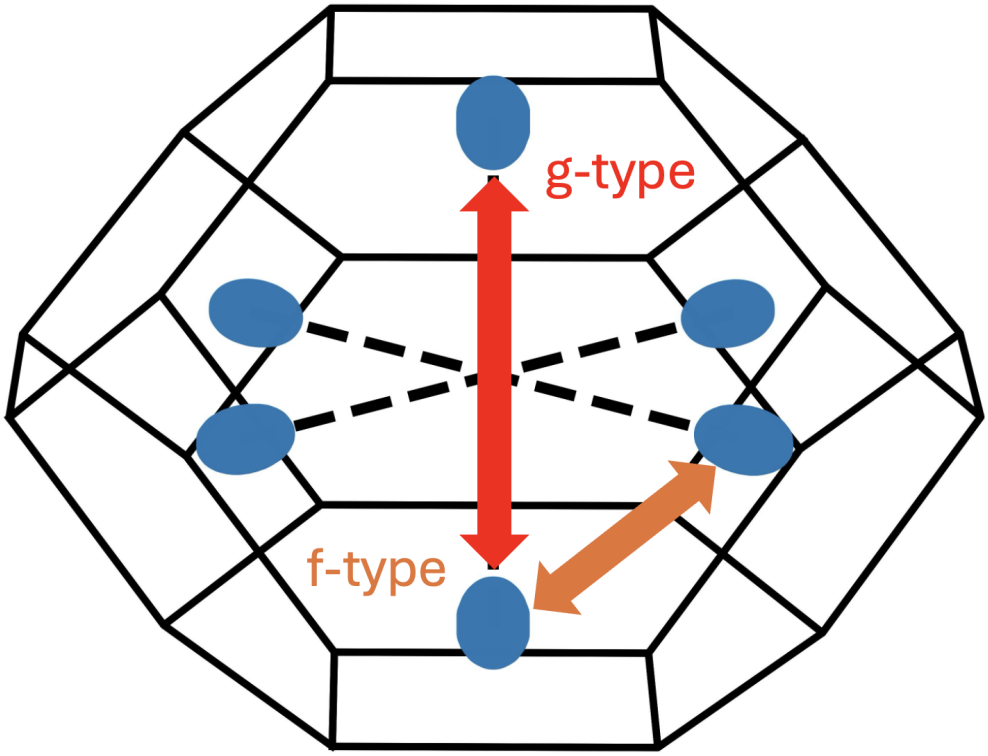

Figure 3.3: Schematic showing the difference between f- and g-type scattering in n-Si. g-type scattering is shown in red, between valleys oriented on the same axis. f-type is shown in orange, between valleys aligned along two different Cartesian axes.

where f- and g-type coupling constants were widely reported [7]. However, due to the fact that the experimentally available data (drift velocity) was insensitive to the exact balance of the two intervalley types, no definitive conclusions were reached and reported deformation potential values varied [8, 46, 107, 157]. In fact, Ref. [29] is a fitting example to show the disadvantage of using the Monte Carlo approach to interpret a quantity like the intervalley noise. When using the fitting parameters from previous results [99, 105], an underestimate of the anisotropy was shown. To fit the experimental data, the two f-type phonons of highest energy were reduced in coupling strength, while the highest-energy g-type phonon was increased in coupling strength. Once suitable agreement with experiment was reached, it was concluded that the coupling strengths must be correct. However, with our ab-initio approach, we are able to accurately probe the amount of f-type scattering, without worrying about adjustable parameters.

Another transport property that is sensitive specifically to the amount of f-type

scattering is the piezoresistivity. Piezoresistivity provides insight into the magnitude of f-type scattering in n-Si due to the following considerations. When a compressive stress is applied along a crystallographic direction, valleys parallel to the stress axis decrease in energy compared to the other valleys. The effect of applying compressive stress in the [100] and [111] directions compared to the unstrained case can be seen in Fig. 3.4.

If the stress is applied in the [001] direction, in the limit of high stress all electrons will be in the [001] valleys. Similarly, if stress is applied in the [011] direction, electrons will be in the [010] and [001] valleys. In the first case ([001] stress), all f-type scattering will be eliminated. However, in the second case ([011] stress), f-type intervalley scattering between [010] and [001] valleys remains. Therefore, if f-type scattering is negligible, the transverse resistivity (for instance resistivity measured along [100]) at high stress in both cases is expected to be identical [105]. If f-type scattering is present, the case with the stress oriented along the [001] will have a lower resistivity due to the lack of f-type scattering. Other observables that may yield insight into ratios of f- and g-type scattering include examining the galvanomagnetic properties of hot electrons [7].

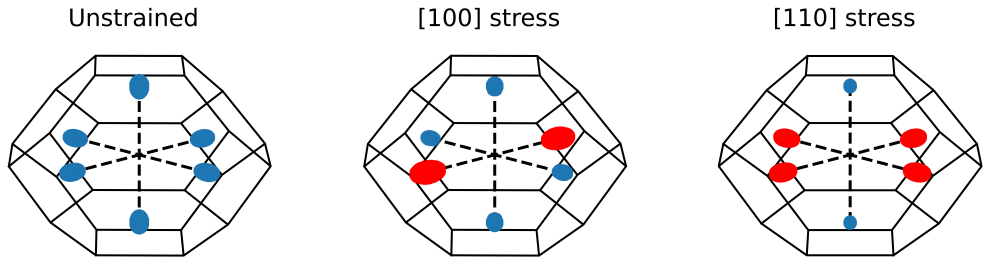

Figure 3.4: Schematic showing how applied compressive stress changes the valley structure in n-Si. On the left, the unstrained case is shown, where the six valleys are equivalent in energy and population. In the middle, the case where compressive stress is applied in the [100] direction is shown, where the valleys along the [100] are shifted lower in energy and have a greater population. On the right, the case where compressive stress is applied in the [110] direction is shown, where valleys along the [100] and [010] directions are shifted lower in energy and have a greater population. In all cases, the valleys shifted downwards in energy are shown in red.

3.4 Solving the BTE for noise

Section 2.3 showed how the BTE can be used to solve for the steady-state occupation function $f^s_{\mathbf{k}}$ of a semiconductor subjected to an electric field $\mathbf{E}$, and thus giving us transport quantities like the drift velocity, mobility, and β. Similarly, we can solve

a different BTE to investigate the fluctuations around this steady-state. Fluctuations still occur in steady-state, due to the Poissonian nature of every scattering event. Thus, we examine the fluctuations $\delta f_{\mathbf{k}}$ around $f^s_{\mathbf{k}}$, where $\delta f_{\mathbf{k}}(t) = f_{\mathbf{k}}(t) - f^s_{\mathbf{k}}$.

The spectral intensity (or density) $S_X(\omega)$ of a stationary random variable $X(t)$ is defined as the squared sum of the Fourier components of $X(t)$ lying in a frequency interval of infinitesimal length, averaged and then divided by the frequency interval. The Wiener-Khintchine Theorem relates $S_X(\omega)$ and the Fourier transform of the time-displaced correlation function of $X(t)$:

$$S_X(\omega) = 2\int_{-\infty}^{\infty} \overline{X(t)X} e^{-i\omega t} dt \tag{3.4}$$

We can use this to relate the power spectral density (PSD) of current fluctuations (the quantity of chief interest in this manuscript) $S_{j_\alpha j_\beta}$ to the Fourier transform of the autocorrelation of the current density fluctuations:

$$S_{j_\alpha j_\beta}(\omega) \equiv (\delta j_\alpha \delta j_\beta)_\omega = 2\int_{-\infty}^{\infty} \overline{\delta j_\alpha(t)\delta j_\beta} e^{-i\omega t} dt \tag{3.5}$$

Here, δj_α and δj_β are the current fluctuations along axes α and β. In order to put this in the form of occupancy fluctuations instead of current fluctuations, we first relate the two via the appropriate prefactors and the drift velocity to weight them:

$$\delta j_\alpha = \frac{2e}{V_0}\sum_{\mathbf{k}} v_{\mathbf{k},\alpha}\delta f_{\mathbf{k}} \tag{3.6}$$

Using this definition, we get

$$\overline{\delta j_\alpha(t)\delta j_\beta} = \left(\frac{2e}{V_0}\right)^2 \sum_{\mathbf{k}}\sum_{\mathbf{k}'} v_{\mathbf{k},\alpha} v_{\mathbf{k}',\beta} \overline{\delta f_{\mathbf{k}}(t)\delta f_{\mathbf{k}'}} \tag{3.7}$$

Eq. (3.7) shows that to compute the PSD of current fluctuations, we must compute the correlation of occupation fluctuations at $\mathbf{k}$ and $\mathbf{k}'$: $\overline{\delta f_{\mathbf{k}}(t)\delta f_{\mathbf{k}'}}$. This quantity is known as the time-displaced, two-particle correlation function [67]. It was shown by Gantsevich and coauthors that the time-displaced, two-particle correlation function obeys the same Boltzmann equation as the fluctuation itself:

$$\frac{\partial}{\partial t}\overline{\delta f_{\mathbf{k}}(t)\delta f_{\mathbf{k}'}} + \sum_{\mathbf{k}_1} \Lambda_{\mathbf{k},\mathbf{k}_1} \overline{\delta f_{\mathbf{k}_1}(t)\delta f_{\mathbf{k}'}} = 0 \tag{3.8}$$

Here, $\Lambda_{\mathbf{k},\mathbf{k}_1}$ is the same relaxation operator of Eq. (2.26), that now acts on the correlation function instead of the deviational occupations. The significance of

Eq. (3.8) is that with only the information needed to describe relaxation of the system to a steady state, we can solve for the fluctuation properties of the system [120]. To solve Eq. (3.8), an initial condition $\overline{\delta f_{\mathbf{k}}(t)\delta f_{\mathbf{k}'}}|_{t=0}$ must be specified, known as the one-time, two-particle correlation function. This condition was derived by Fowler [62] and Lax [120] (for a non-degenerate system of N particles) as:

$$\overline{\delta f_{\mathbf{k}}(t)\delta f_{\mathbf{k}'}}|_{t=0} = f^s_{\mathbf{k}}\delta_{\mathbf{k}\mathbf{k}'} - \frac{f^s_{\mathbf{k}} f^s_{\mathbf{k}_1}}{N} \tag{3.9}$$

We can combine Eq. (3.5) and Eq. (3.7) to get an expression for the PSD of current fluctuations in terms of the PSD of occupancy fluctuations:

$$(\delta j_\alpha \delta j_\beta)_\omega = \left(\frac{2e}{V_0}\right)^2 \sum_{\mathbf{k}} \sum_{\mathbf{k}'} v_{\mathbf{k},\alpha} v_{\mathbf{k}',\beta} (\delta f_{\mathbf{k}} \delta f_{\mathbf{k}'})_\omega \tag{3.10}$$

Here,

$$(\delta f_{\mathbf{k}} \delta f_{\mathbf{k}'})_\omega = \int_{-\infty}^{\infty} \overline{\delta f_{\mathbf{k}}(t)\delta f_{\mathbf{k}'}} e^{-i\omega t} dt \tag{3.11}$$

As we are interested in the PSD at a certain frequency, we can solve the Fourier-transformed version of Eq. (3.8). Utilizing the stationary properties of the auto-correlation function, we can write the Fourier-transformed correlation function as [67]:

$$(\delta f_{\mathbf{k}} \delta f_{\mathbf{k}'})_\omega = 2\Re\Big[\sum_{\mathbf{k}_1} (i\omega\mathbb{I} + \Lambda)^{-1}_{\mathbf{k}\mathbf{k}_1} \overline{\delta f_{\mathbf{k}_1}(t)\delta f_{\mathbf{k}'}}|_{t=0} \Big] \tag{3.12}$$

Combining Eq. (3.9), Eq. (3.10), and Eq. (3.12), we obtain:

$$S_{j_\alpha j_\beta}(\omega) = 2\left(\frac{2e}{V_0}\right)^2 \Re\Big[\sum_{\mathbf{k}} v_{\mathbf{k},\alpha} \sum_{\mathbf{k}_1} (i\omega\mathbb{I} + \Lambda)^{-1}_{\mathbf{k}\mathbf{k}_1} \sum_{\mathbf{k}'} v_{\mathbf{k}',\beta} \Big(f^s_{\mathbf{k}_1}\delta_{\mathbf{k}_1,\mathbf{k}'} - \frac{f^s_{\mathbf{k}_1} f^s_{\mathbf{k}'}}{N} \Big) \Big] \tag{3.13}$$

Explicitly evaluating the last sum over $\mathbf{k}'$ by using Eq. (2.28) for the definition of the drift velocity, we obtain:

$$S_{j_\alpha j_\beta}(\omega) = 2\left(\frac{2e}{V_0}\right)^2 \Re\Big[\sum_{\mathbf{k}} v_{\mathbf{k},\alpha} \sum_{\mathbf{k}_1} (i\omega\mathbb{I} + \Lambda)^{-1}_{\mathbf{k}\mathbf{k}_1} (f^s_{\mathbf{k}_1}(v_{\mathbf{k}_1,\beta} - V_\beta)) \Big] \tag{3.14}$$

Thus, we see from Eq. (3.14) that in order to obtain the spectral density of the current fluctuations, we must first solve for the steady occupation function in Eq. (2.27). Once this is solved, we solve another Boltzmann equation, with the different inhomogeneous term $(f^s_{\mathbf{k}}(v_{\mathbf{k},\beta} - V_\beta))$. Once the second Boltzmann equation is solved, we can obtain the spectral density of the current fluctuations by the Brillouin zone integration in Eq. (3.14).

3.5 Computational details

For all calculations, the electronic structure and electron-phonon matrix elements are computed on a coarse $14 \times 14 \times 14$ grid using DFT and DFPT with Quantum Espresso [72]. This finer coarse grid was used, in comparison to the 8×8×8 that was found to be sufficient to converge the unstressed mobility in Section 2.5. A wavefunction energy cutoff of 40 Ryd was used for all calculations, and a relaxed lattice parameter of 5.431 Å was used for the unstrained properties. The electronic structure and electron-phonon matrix elements were interpolated onto the fine grid using Perturbo [223]. For every combination of applied stress value and direction, the electronic structure and electron-phonon matrix elements were re-computed. The piezoresistivity was then computed by calculating the transverse mobility (mobility in the [001] direction) using Eq. (2.29) (from which the resistivity may be obtained by taking the inverse), and then normalizing by the calculated unstrained resistivity value. For the calculations with compressive stress in the [001] direction, a small uniaxial compressive strain was applied in the [001] direction by fixing one axis artificially in Quantum Espresso using the 'fixc' option, and the other two lattice vectors were then relaxed using the 'vc-relax' cell relaxation method. For the calculations with compressive stress in the [011] direction, the lattice vectors were changed manually until the desired stress state was reached.

For temperatures of 160 – 300 K, a grid density of $100 \times 100 \times 100$ for the electron states was used, while a grid density of $50 \times 50 \times 50$ was used for the phonons. We report convergence tests on the PSD values, as they are more sensitive to the details of the band structure and electron-phonon interaction than the mobility. Using a phonon grid with the same density as the electron grid resulted in a PSD change of 17% at 10 kV cm^{-1}, and using a grid density of $120 \times 120 \times 120$ for the electron states and $60 \times 60 \times 60$ for the phonon states resulted in a PSD change of 20% at 10 kV cm^{-1}. The quantity of relevance to our findings is the anisotropy between [111] and [100], defined as $(\mathrm{PSD}_{[111]} - \mathrm{PSD}_{[100]})/\mathrm{PSD}_{[111]}$. This quantity only changed by 0.5% when changing the grid density, indicating that the PSD anisotropy was well-converged. From 160-300 K we used an energy window of 284 meV above the conduction band minimum with a Gaussian smearing parameter of 5 meV, and increasing this energy window to 342 eV resulted in a PSD change at 10 kV cm^{-1} of 1%.

For the grid density at 77 K, a grid density of $140 \times 140 \times 140$ for the electron states and $70 \times 70 \times 70$ for the phonon states was used, with an energy window of 145 meV

and a Gaussian smearing parameter of 2.5 meV. For 77 K, increasing the energy window to 284 meV resulted in a PSD change of 7% at 1 kV cm^{-1}. Using a phonon grid with the same density as the electron grid resulted in a change of 12% in the PSD at 1 kV cm^{-1}, the largest field used. Using a grid density of $160 \times 160 \times 160$ for the electron states and $80 \times 80 \times 80$ for the phonon states resulted in a PSD change of 18% at 1 kV cm^{-1}. However, as before, our findings are not affected by these changes, as the qualitative trend of the PSD compared to experiment is unchanged, and the sign of the anisotropy is unchanged. Therefore, the calculations are converged adequately at 77 K for the PSD.

For the piezoresistivity calculations (all performed in the low-field limit), a grid density of $400 \times 400 \times 400$ ($200 \times 200 \times 200$) for electrons (phonons) was required. Increasing the electron grid density to $500 \times 500 \times 500$ and the phonon grid was $250 \times 250 \times 250$ resulted in mobility changes of 15%. As the relevant quantity for our conclusions is the piezoresistivity, which is normalized by the zero-stress resistivity value, the normalized trend changed only on the order of 5%. In this case, an energy window of 20 meV was employed for computational tractability. Increasing the energy window from 20 meV to 25 meV resulted in mobility changes of 4%. The final linear system of equations used to obtain the mobility and the PSD was then solved by a Python implementation of the GMRES method [63]. For all calculations and temperatures, the Fermi level was adjusted to yield a carrier density of 4×10^{13} cm^{-3}. Spin-orbit coupling was neglected, as it has a weak effect on electron transport properties in Si [135, 163]. Similarly, quadrupole electron-phonon interactions were neglected [161]. For all calculations of the diffusion coefficient, a frequency of 1 GHz was used, selected so to ensure that $\omega\tau^{-1} \ll 1$, where τ is a characteristic relaxation time, while avoiding too low frequencies which result in numerical instabilities.

In our past work [86], it has been shown that two-phonon scattering (2ph) is non-negligible in n-Si. Thus, for all PSD calculations, two-phonon scattering was included. For the piezoresistivity calculations, 2ph scattering could not be included due to the computational cost. However, we do not expect the absence of 2ph scattering for piezoresistivity to affect our conclusions, as it was shown in Ref. [86] that the energy dependence of 2ph scattering rates exhibited the same qualitative trends as those of one-phonon rates, and further that most of the effect of 2ph scattering can be accounted for by scaling the 1ph scattering rates. As this scaling would be present at all applied stresses, we therefore do not expect that neglecting

2ph would affect the piezoresistivity values and our conclusions.

3.6 Results

Electric-field dependence of hot electron diffusion coefficient

We begin by examining the dependence of the diffusion coefficient on electric field at various temperatures. We first compare the experimental low-field values of the diffusion coefficient to the computed ones. We considered four temperatures (300, 200, 160, and 77 K), corresponding to those for which experimental data is available. At these temperatures, the computed (experimental) diffusion coefficients were 29.7 (37) cm^2s^{-1}, 59.3 (62) cm^2s^{-1}, 58.8 (71) cm^2s^{-1}, and 1120 (141) cm^2s^{-1}. For all temperatures besides 77 K, the computation underestimates the experimental data. The magnitude of the underestimate for $T > 77$ K is consistent with a prior calculation of the electron mobility of Si when two-phonon scattering is included [86]. However, at 77 K, the computed value is $\sim 8\times$ larger than experiment. This overestimate is possibly attributable to ionized impurity scattering which is neglected in the present calculations.

To facilitate the comparison of trends with electric field in the subsequent plots, the computed data has been normalized to the calculated low-field diffusion coefficient, while the experimental data has been normalized to the value at the lowest electric field reported. We note that due to the requirement that the transit time in the time-of-flight experiment be less than the dielectric relaxation time, no data was reported below a minimum field at each temperature [29]. The electric field dependence of the diffusion coefficient at 300 K is shown in Fig. 3.5a. In experiment, it is observed that at low fields, the diffusion coefficient along the [100] and [111] directions are equal. Starting at less than 2 kV cm^{-1}, the diffusion coefficient along the [111] direction is less than in the [100], an anisotropy that has been attributed to intervalley diffusion [29]. The magnitude of this anisotropy continues to increase with field, reaches a maximum, and then decreases with field. The same qualitative trend with field is seen at 200 K in Fig. 3.5b, with the main difference being the anisotropy manifesting at lower fields than at higher temperatures. At 160 K, shown in Fig. 3.5c, there is a slight peak of the diffusion coefficient in the [100] direction at low fields and then a monotonic decrease for higher fields. At 77 K, shown in Fig. 3.5d, initial increases of the diffusion coefficient with field are seen for both directions.

The calculated results generally predict these trends qualitatively. At 300 K and 200 K, the correct trend of the anisotropy is reproduced, as the [111] diffusion coefficient

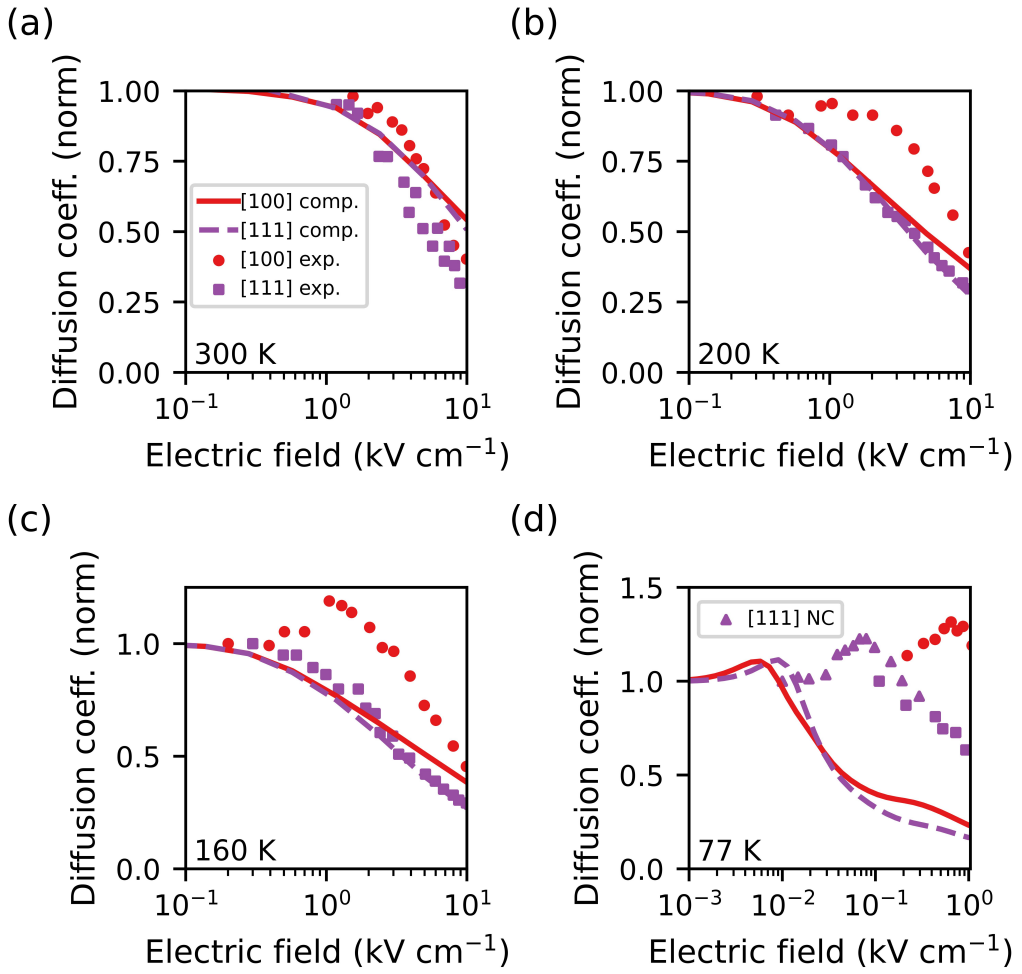

Figure 3.5: Diffusion coefficient (normalized by the zero-field value) versus electric field for n-Si at (a) 300 K, (b) 200 K, (c) 160 K, and (d) 77 K with field applied along the [100] direction (red solid line) and [111] direction (purple dotted line). Experimental data along the [100] direction (red circles) and [111] direction (purple squares) from Figures 3 and 4, Ref. [29]. In (d), noise conductivity (NC) measurements (purple triangles) included for comparison at low electric fields.

is less than the [100] value once field values exceed 5 kV cm^{-1} and 2 kV cm^{-1}, respectively. While the initial increase seen in experiment at 160 K with field applied in the [100] direction is not captured by computation, the qualitative anisotropy at high fields is reproduced. Similarly, at 77 K, the [111] diffusion coefficient is less than in the [100] once the electric field exceeds 0.2 kV cm^{-1}.

However, a number of quantitative discrepancies can be seen. At 160, 200, and 300 K, the computed anisotropy starts to manifest at higher fields than in experiment. In experiment, at 300 K the anisotropy is observed once the electric field exceeds 2 kV

cm^{-1}, while at 200 K and 160 K the anisotropy manifests even below 1 kV cm^{-1}. Similarly, the magnitude of the anisotropy is underestimated, particularly for 160 K and 200 K, where the agreement with the [111] data is excellent, but the [100] data lies much above the computed values.

At 77 K, the qualitative behavior of the diffusion coefficient with field changes greatly. We note that the electric field range used in this calculation is smaller than in the other cases due to lack of convergence at high fields. In Fig. 3.5d, for both directions measured an initial increase in the experimental PSD is seen. This increase is observed in computation, but at lower fields than in experiment. Given the relative importance of ionized impurity scattering at 77 K compared to higher temperatures, we examined whether the omission of this scattering mechanism in the calculation could play a role in the discrepancy. We implemented a simple model of ionized impurity scattering [131] with a density of 10^{14} cm^{-3}. The non-monotonic features were observed to shift to higher electric fields, suggesting that ionized impurity scattering could be partly responsible for this discrepancy.

The anisotropy in the diffusion coefficient seen in experiment has been attributed to a mechanism known as intervalley diffusion. [29]. As τ_{int} is inversely proportional to the square of the f-type coupling constant [29], a possible origin of the underpredicted anisotropy in the diffusion coefficient is computed f-type scattering rates which are too large compared to experiment. To test this hypothesis, we compute other transport and noise properties which are sensitive to the distinct types of intervalley scattering.

Microwave-frequency PSD

We first compute the microwave-frequency (~0.1-100 GHz) PSD at 77 K and 200 V cm^{-1}, for which experimental data is available for comparison [15]. Here, the frequency ranges computed are much higher than those in which sources of noise such as $1/f$ noise or generation-recombination noise would be relevant.

Figure 3.6 shows the calculated spectral density of current fluctuations versus frequency, at 77 K and 200 V cm^{-1} and with electric fields applied along the [111] and [100] directions, along with experimental data. At frequencies below 3 GHz, the [100] PSD is greater than the [111], due to the presence of intervalley diffusion. As intervalley scattering is characterized by a significantly smaller relaxation rate than either the energy or momentum relaxation rates, a rolloff in the [100] direction is observed around the relatively low frequency of 1 GHz. The presence of the "con-

vective" mechanism away from equilibrium rolls off at a frequency corresponding to the energy relaxation rate. Here, the convective peak occurs around 25 GHz. For semiconductors with a sublinear current-voltage characteristic, this convective contribution is negative [84]. This mechanism is present in both the [100] and [111] cases, but is more obviously present in the [111] due to the lack of intervalley noise. Finally, as the frequency exceeds the momentum relaxation rate, the PSD rolls off to zero as the electronic system is not able to redistribute in response to the oscillating external field.

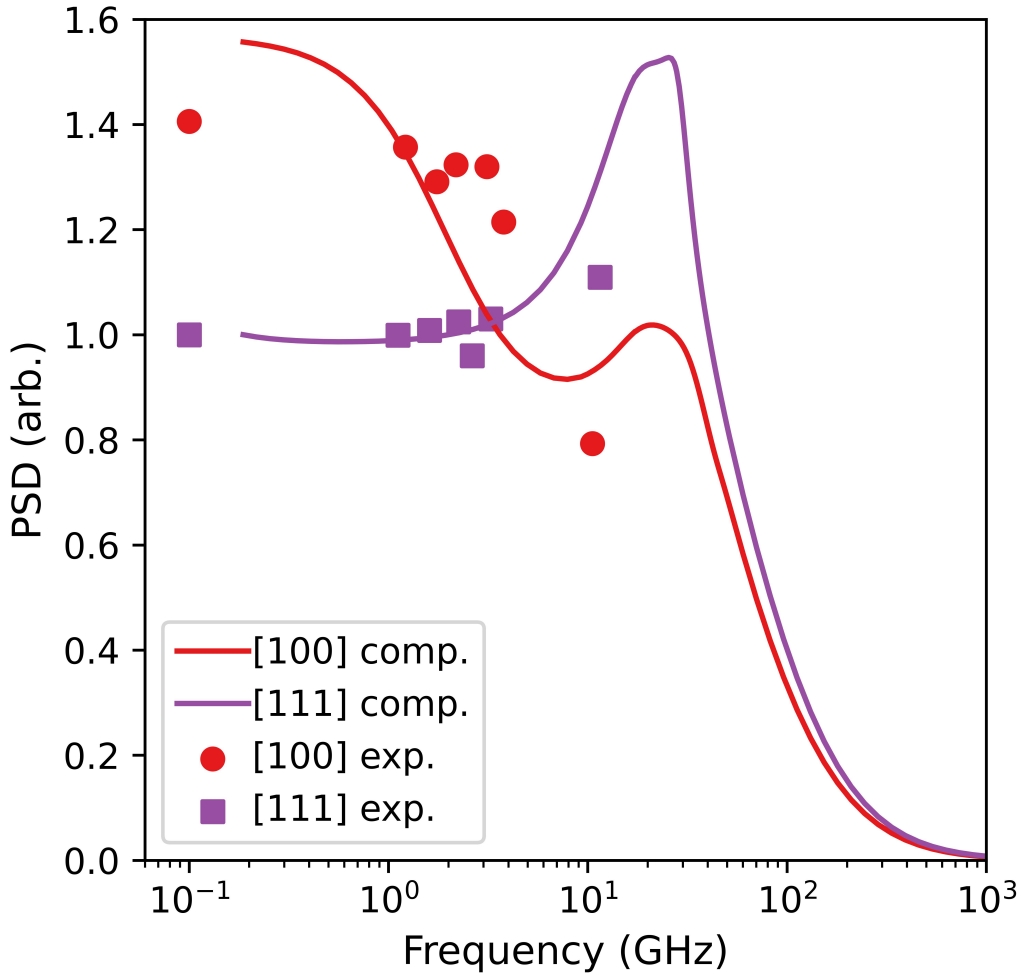

Figure 3.6: Microwave PSD versus frequency for n-Si at 77 K and 200 V cm^{-1} applied electric field, with field applied along the [100] direction (red solid line) and [111] direction (purple solid line). Experimental data along the [100] direction (red circles) and [111] direction (purple squares) from Figure 1, Ref. [15]. In both cases, the data is normalized to the value of the PSD at the lowest frequency data point (computation, 0.19 GHz; experiment, 0.1 GHz) in the [111] direction.

Over the entire calculated frequency range, the computed results qualitatively capture the trends seen in experiment. The anisotropy seen at low frequencies due to intervalley noise, the rolloff in the [100] direction starting around 1 GHz due to frequency exceeding the characteristic intervalley scattering rate, and the convective noise peaks are all reproduced. At frequencies above 100 GHz, the PSD is higher in the [111] direction, simply due to the greater mobility in this direction at 200 V cm^{-1}. Relaxation times for the various noise sources (thermal, convective, and intervalley) can be obtained by fitting the computed curves to Lorentzians parameterized by the various relaxation times, as given in Eq. 9.5 in Ref. [84]. For the [111] direction, an energy relaxation time of 15 ps was calculated using Monte Carlo simulation, as well as a momentum relaxation time of 2 ps, while our computation yields an energy relaxation time of 9 ps, and a momentum relaxation time of 4 ps [84]. For the [100] direction, Monte Carlo simulation reported an energy relaxation time of 5 ps [84], and an intervalley relaxation time of 50 ps [15], while our computation yields an energy relaxation time of 10 ps, and an intervalley relaxation time of 79 ps. The magnitudes of the relaxation times and relative difference between the momentum and energy relaxation times are thus in qualitative agreement with prior works. However, data only exists up to intermediate frequencies (around 10 GHz), so it is difficult to draw quantitative conclusions, especially for the momentum relaxation time.

As the difference in the PSD at low frequency is due to intervalley noise, and the magnitude of this difference is captured accurately by our computation, the results of Fig. 3.6 suggest that the f-type scattering rates in computation are compatible with their actual values. In addition, the frequency of the intervalley roll-off and convective mechanism being well-captured imply that both the intervalley and energy relaxation rates are qualitatively consistent with experimental values.

Piezoresistivity

We next compute the piezoresistivity at 300 K and 77 K, for which experimental data is available [80]. In Fig. 3.7a, the computed transverse resistivity versus stress in the [001] and [011] directions at 300 K is presented. The computed anisotropy exhibits qualitative agreement with experiment, as in both cases the resistivity is less when the stress is applied along the [001] compared to the [011] case. Due to the non-negligible contribution of f-type scattering at 300 K, applying pressure along the [001] eliminates f-type scattering in the high-stress limit and thereby decreases the resistivity by a greater amount than in the [011] case. However, the

computation underpredicts the transverse resistivity at all pressures for both applied stress directions.

In Fig. 3.7b, the computed transverse resistivity versus stress at 77 K is shown along with experimental data. Here, it is observed in experiment that at high stresses, the resistivity along both directions saturates to closer to the same value than at 300 K. The computed resistivity saturates with pressure to a slightly lower value than in experiment, but the difference between the two directions is considerably smaller than at 300 K (69% at 300 K versus 8% at 77 K). The relatively small difference in the high-pressure 77 K resistivity between the two directions indicates that f-type scattering is negligible at this temperature, while at 300 K the computed difference between the two directions is comparable with experimental results. The agreement at both temperatures indicates that the magnitude of f-type scattering at these temperatures is being qualitatively captured.

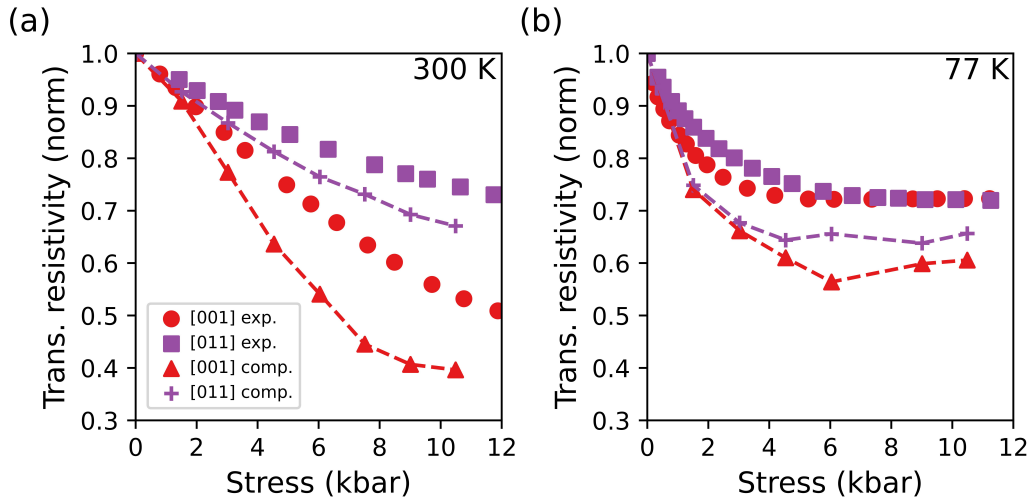

Figure 3.7: Computed normalized transverse resistivity versus stress in n-Si at (a) 300 K and (b) 77 K, with stress applied along the [001] direction (red triangles) and [011] direction (purple crosses). Experimental data along the [001] direction (red circles) and [011] direction (purple squares) from Figures 3 and 4, Ref. [80].

3.7 Discussion

Figure 3.5 indicates that the anisotropy of the diffusion coefficient in n-Si is qualitatively captured in the calculation, with the diffusion coefficient in the [111] direction being less than in the [100] in the high-field limit for all temperatures measured. The primary discrepancies between experiment and computation between 160 and 300 K are the anisotropy in the computed results being smaller and not manifesting

until higher fields compared to experiment. The smaller anisotropy in the computed results suggests that the computation underestimates the amount of intervalley noise, and thus overestimates the amount of f-type scattering. However, Fig. 3.6 indicates that the computed intervalley scattering rates and intervalley noise magnitude are qualitatively compatible with experiment, and Fig. 3.7 shows that the variation of f-type scattering with temperature is qualitatively captured as well. The amount of error in the computed f-type scattering rate is therefore constrained to values that are insufficient to explain the discrepancies in the diffusion coefficient.

One additional way to confirm this assertion is to examine the diffusion coefficient in n-Si with a modified version of the scattering matrix. If indeed the f-type scattering is described incorrectly, we may approximate the effects of having lower f-type scattering by manually changing the electron-phonon scattering rates (only for those corresponding to an f-type scattering process). For illustration, in Fig. 3.8, the diffusion coefficient results for a case in which the f-type scattering rates have been halved is shown, along with the original results and experimental data. While halving the f-type scattering rates does cause a larger anisotropy in the diffusion coefficient, as well as causing this anisotropy to start significantly manifesting at lower electric field values (the [100] diffusion coefficient is clearly higher in the scaled f-type case at an electric field value of 3.1 kV cm^{-1}, as opposed to 4.1 kV cm^{-1} in the original computation), this effect is not nearly enough to resemble the large anisotropy shown in experiment. Thus, this indicates that if this discrepancy is caused by an incorrect description of f-type scattering, the f-type rates must be several times smaller than what is computed.

Given these observations, and that we have used the highest level of ab-initio theory presently available which include two-phonon scattering, our findings suggest an external mechanism not contained in the computation is responsible for the discrepancy. We suggest that this mechanism could be the neglect of spatial inhomogeneities present in experiment. The ab-initio method used here does not include real-space effects such as concentration gradients or space charge effects. Although the time-of-flight experiment was carefully implemented to avoid dielectric relaxation in the sample, it is conceivable that fluctuations in drift velocity associated with intervalley scattering within the generated electron pulse could lead to space charge effects which would spatially broaden the pulse and hence increase the measured diffusion coefficient. This effect would be present only in the [100] direction due to the absence of intervalley scattering in the [111] direction. Further, these effects

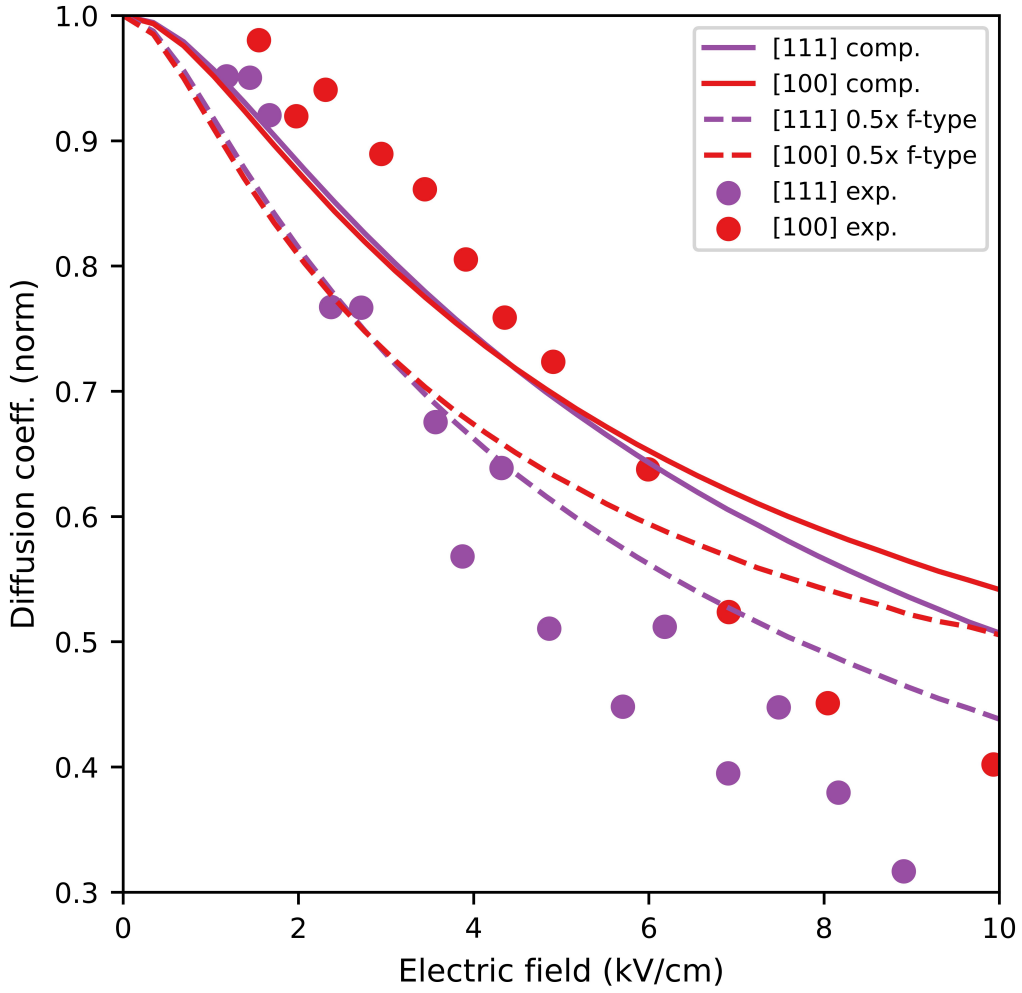

Figure 3.8: Diffusion coefficient versus electric field at 300 K in n-Si. The circles represent experimental data taken from Ref. [29], the solid lines represent the results of our original computation (also contained in Fig. 3.5a, and the dotted lines represent a computation in which the f-type scattering rates have been artificially halved. Data in red represents the electric field applied in the [100] direction, while data in purple represents the electric field applied in the [111] direction. This shows that even an overestimate of $\sim$ 2x would not be nearly enough to make up the experimental discrepancy.

would not appear in the microwave PSD as these frequencies are much higher than those associated with any dielectric relaxation phenomena. Additional study will be required to determine the origin of the diffusion coefficient discrepancies.

3.8 Summary

In this chapter, we introduced how our first-principles approach could be applied to fluctuational variables. With this approach, we focused on intervalley noise in n-Si,

and computed the hot-electron diffusion coefficient, microwave PSD, and piezoresistivity from 77 – 300 K. We find that while qualitative features of the diffusion coefficient such as the anisotropy at high electric fields are generally predicted, several trends of the calculated values differ from experiment. We computed the piezoresistivity and microwave PSD to investigate whether an inaccurate description of f-type intervalley scattering could explain the discrepancies (as these variables are sensitive to the precise amount of f-type scattering, unlike most observables).

However, the good qualitative agreement of these properties with experiment excluded this possibility, leading to the hypothesis that the measured diffusion coefficient is influenced by factors not included in ab-initio calculations such as real-space gradients and space charge effects. This finding indicates that care must be taken when interpreting diffusion coefficient measurements in terms of microscopic charge transport processes.

Chapter 4

VALLEYTRONICS AND NEGATIVE DIFFERENTIAL RESISTANCE IN CUBIC BORON NITRIDE: A FIRST-PRINCIPLES STUDY

This chapter has been adapted, in part, from:

> Benjamin Hatanpää and Austin J. Minnich. Valleytronics and negative differential resistance in cubic boron nitride: a first-principles study, 2024. https://arxiv.org/abs/2408.08458
> B.H. co-designed the research, conducted the calculations, analyzed the data, and wrote the manuscript.

Si, Ge, and "conventional" III-V materials were dominant in semiconductor technology for the first 40 years of the field's development. Wide-bandgap materials were not widely used until the early 1990s [4, 149, 151, 152], after breakthroughs were made that made InGaN widely used due to its optoelectronic properties. Other wide-bandgap technologies based off of materials such as SiC [160] and GaN [182, 219] are maturing rapidly, mostly due to their electronic properties. In electronic applications, as opposed to optoelectronics, indirect bandgap materials can be used and light emission efficiency is unimportant, relaxing the constraints on material selection [210]. However, there are another class of materials that have not been extensively explored for device applications, which have bandgaps much larger than the 3.4 eV of GaN.

Ultrawide-bandgap (UWBG) semiconductors are the subject of intense recent study owing to their utility in power electronics and related device applications [210, 217]. Cubic boron nitride (c-BN), with a wide bandgap of 6.4 eV [44], has long been of interest for electron devices and other applications owing to its competitive mechanical, thermal, and electrical properties. c-BN has a high hardness of 30-43 GPa [83], thermal conductivity which is second only to diamond [39], excellent oxidation resistance, and high chemical and thermal stability. In addition, c-BN also has a high electric breakdown field of 4 MV cm^{-1}, comparable to those of diamond and GaN; [41] and a high predicted saturation drift velocity of 4.3×10^7 cm s^{-1}, which is the highest of any semiconductor. These properties lead to the

prediction of among the highest figure-of-merits (such as Johnson, Baliga, and Keyes figures-of-merit) for high-frequency and high-power applications [41, 82, 210].

In addition to transistor-based devices using UWBGs, other device types such as transferred-electron and valleytronic devices are of interest. For instance, diamond exhibits a region of negative differential resistance (NDR) below room temperature [96], enabling the realization of Gunn oscillators. [202] Further, the large intervalley time of 300 ns [97] allows for manipulation of electrons by their valley degree of freedom, for instance in a valleytronic transistor [203]. However, diamond has long-standing challenges, including the difficulty to realize n-type doping [26, 71, 190] and synthesis of high-quality thin films.

c-BN has potential to overcome some of these difficulties. c-BN can be doped both n- and p-type [128, 204, 205, 212], has a higher oxidation temperature than diamond, and is more thermally and chemically stable [98]. c-BN also may be useful in conjunction with diamond in devices, as due to the small degree of lattice mismatch between c-BN and diamond of 1.4%, heteroepitaxy can be attained between the two [27, 113, 212, 220]. In addition, several theoretical studies have been done that point to the possibility of creating a two-dimensional hole gas (2DHG) [148, 215], and NV-based quantum sensors using diamond and c-BN [191] . However, c-BN films face various challenges in synthesis, including formation of nanocrystalline films, growth of the hexagonal crystal structure rather than the desired cubic structure [185], and high compressive stresses. [218] As a result, devices based on c-BN are still rare. Most devices are limited to $p-n$ junctions [158] fabricated from doped or intrinsic c-BN thin films [221]. Diodes [143] and ultraviolet emitters [144] have been realized in c-BN. In addition, deep-ultraviolet photodetectors based on c-BN have been fabricated [18, 127, 196], which are of interest for extreme-environment applications.

Considering that diamond thin films have been found to be promising for Gunn oscillators and valleytronic transistors [202, 203], it is natural to consider c-BN as well given the similarities in electronic band structure. However, experimental data regarding the transport properties of c-BN, especially at high electric fields, are scarce. The low-field mobility has been reported experimentally [81, 90, 156, 212], with values varying by several orders of magnitude. The low-field mobility of c-BN has been computed with ab-initio methods [95, 164, 186], but investigations at higher fields are limited to Monte Carlo methods with semi-empirical inputs [42, 195, 224]. The properties relevant for transferred-electron and valleytronic

devices, namely the occurrence of negative differential resistance and a sufficiently long intervalley scattering time, have not yet been assessed in c-BN.

In this chapter, we report first-principles calculations of the high-field electron transport properties and noise characteristics of c-BN. We find a pronounced region of negative differential resistance below 140 K. This feature occurs due to the strong dependence of the electron scattering rates associated with optical phonon emission. The high optical phonon energy in c-BN also leads to intervalley scattering times rivaling those of diamond. We identify how these predictions could be experimentally tested via a non-monotonic trend in the spectral noise current density versus electric field. These properties suggest that c-BN is a promising contender in novel electronics applications such as valleytronics or Gunn oscillators.

4.1 Band structure and phonon dispersion of c-BN

Cubic boron nitride (c-BN) is a ultra-wide-bandgap semiconductor (UWBG), of recent scientific interest. The cubic form of BN has been known of since 1957 [214], and is used most commonly as an industrial abrasive due to its mechanical properties [156]. However, as mentioned previously, the electronic properties of c-BN are also of scientific interest, but have not been extensively probed. To start, we investigate the band structure and phonon dispersion.

The calculated bandstructure of c-BN is shown in Fig. 4.1. The conduction band minima are at the X points, giving three equivalent valleys in reciprocal space, while the valence band minima is at Γ. We note here that the next-lowest conduction band minimum is calculated to be 4.32 eV higher in energy than the conduction band minimum, far higher than the electronic states occupied at the highest fields used in this work. Thus, the assumption of only using one band is valid. In addition, we note that the next-lowest-energy satellite valley at K is 2.44 eV higher than the conduction band minimum as well.

We next discuss the calculated phonon dispersion of c-BN, shown in Fig. 4.2. We first note that the longitudinal optical phonon energy at the Γ point is 157 meV and the transverse optical phonon energy is 128 meV, which are 1822 K and 1485 K in temperature units, respectively. The calculated LO-TO split is similar to other computed values [147, 186]. The high Debye temperature here limits scattering events between electrons and emission of optical phonons, as the average electron at 300 K or below does not have enough energy to emit an optical phonon.

As the masses of boron and nitrogen are not very dissimilar, the phonon bandgap

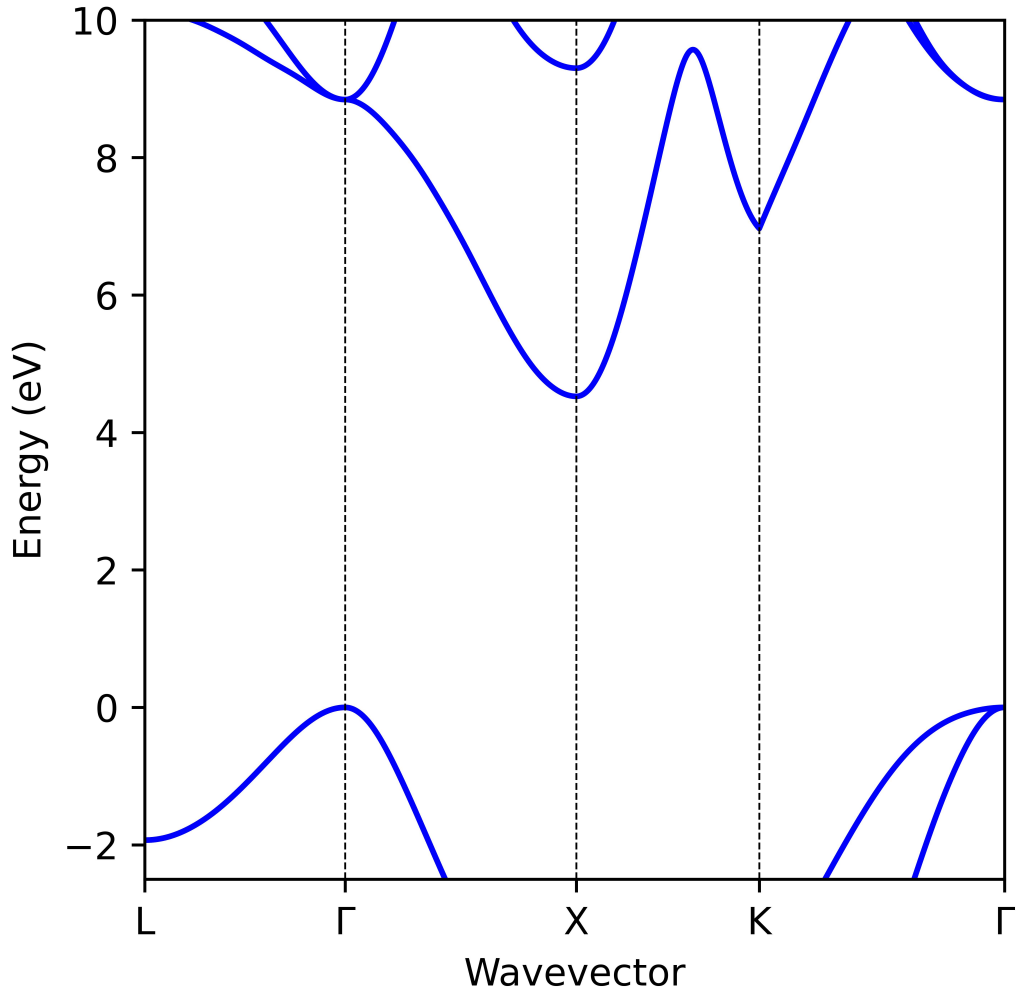

Figure 4.1: Computed electronic band structure of c-BN, showing the two highest lying valence bands, and two lowest lying conduction bands. The valence band minimum is at Γ, while the conduction band minimum is at X, making c-BN an indirect gap semiconductor.

is minimal. Acoustic phonons also are high energy (> 50 meV), except for small wavevector acoustic phonons. Thus, low energy scattering is almost all intravalley, due to the small wavevector.

4.2 Negative differential resistance

Negative differential resistance (NDR), or a decreasing drift velocity with an increase in electric field, in semiconductors was first theoretically predicted in 1961, where Hilsum predicted that such behavior could be observed in GaSb and GaAs [89], and Riley and Watkins posited that Ge/Si alloys and III-V semiconductors would be promising candidates for NDR materials [180]. When Gunn oscillations were first

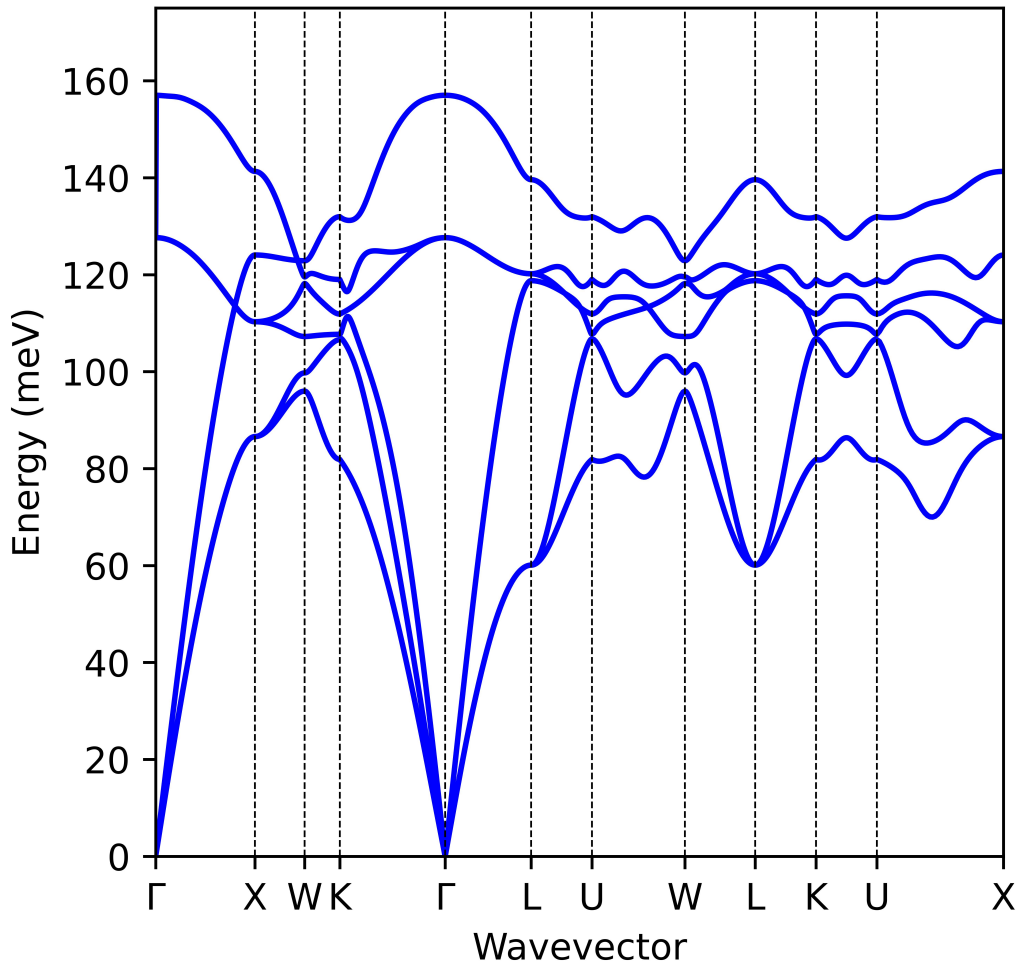

Figure 4.2: Computed phonon dispersion of c-BN. The large optical phonon energy that limits optical phonon emission can be observed, as well as the small phonon bandgap.

observed in GaAs and InP [76], it was then shown that NDR was the cause [114].

The most common types of materials that exhibit NDR are semiconductors with a direct bandgap, and non-equivalent local minima with an energy separation. When an electric field is applied, more population is scattered into higher energy satellite valleys that have a negligible population at low fields. If these satellite valleys have a higher effective mass (and thus lower mobility), NDR can be seen. A good example of this phenomenon is shown in n-GaAs. At low fields, the vast majority of electrons are in the lowest-energy Γ valley. However, there are eight satellite L valleys, approximately 0.3 eV higher in energy than the CBM. These valleys have a significantly larger effective mass than the Γ valley, and thus a lower mobility. Thus, when the field is significant enough, the electrons have a high enough energy to be

transferred from the Γ valley to the L valleys, resulting in a decrease of the total drift velocity in the material.

However, it is possible for a material to exhibit NDR even without non-equivalent local minima. For instance, it was posited that NDR would be seen in n-Si (which has six equivalent valleys) below 50 K, and it was later confirmed experimentally [9, 30, 107]. Later, NDR was observed in diamond below 140 K when the electric field was oriented along the [100]. This was shown to be due to the strong repopulation effect caused by hot electrons reaching the energy threshold for LA phonon emission [96].

It can be shown via thermodynamic arguments ([178, 179]), that if a material is biased in a NDR region, the system becomes unstable and a high-field region forms at the cathode, necessitating a decrease in field elsewhere along the sample. Once the high-field region reaches the anode, it disappears but the instability of the system causes it to appear again at the cathode [172]. These oscillations in current are known as Gunn oscillations, and Gunn diodes are mainly used to provide microwave power in the GHz to THz range from a DC bias [76, 180], used in radio astronomy receivers [20], and sensors and measuring instruments such as radar detectors [139]. Thus, identifying materials with a pronounced NDR region may lead to new Gunn diode devices.

4.3 Valleytronics

In the 1980s, it was observed that certain transport phenomena in solid-state devices were spin-dependent [11, 103]. This observation led to the idea of spintronics: using the intrinsic spin degree of freedom of the electron in devices [48]. Spintronic devices have been used for applications such as information storage and processing [21]. However, the electron spin is not the only degree of freedom that can possibly be exploited in devices. Any local minima in the conduction band is referred to as a valley [188]. Valleytronics is the idea of manipulating the valley degree of freedom in a material, in order to perform operations. An ideal valleytronic material is one with several energy-degenerate valleys [188]. In a sense, manipulating the valley degree of freedom in order to change a material's properties is not a new idea. For instance, as seen in Section 3.3, applying stress to a multi-valley semiconductor will shift the valley energies, leading to increased (or decreased) mobility along certain directions. This phenomena has been used to increase mobility in devices [124, 208]. However, the ability to use this degree of freedom has not been exploited

nearly to the extent as it is in spintronic devices.

Most valleytronic devices fabricated have been two-dimensional, using materials such as graphene or group VI transition metal dichalcogenides monolayers [188]. Frequently, these devices exploit the +K and -K points in the Brillouin zone to store binary information. Some three-dimensional materials exhibit significant valley polarization under an applied field (usually at cryogenic temperatures), such as diamond [97] and silicon [32]. However, three-dimensional valleytronic devices have not been studied in much depth, due to the lack of strong coupling between the valley index and the external field (making initialization, readout, and information manipulation more difficult) [211]. However, a three-dimensional valleytronic transistor has recently been created using diamond [203], and even a room-temperature valleytronic transistor has been created using the Weyl semiconductor tellurium, due to its band topology [38]. Thus, the area of three-dimensional valleytronics is emerging, and finding materials suited for these applications is key. The most important quantity to examine when searching for these materials is the intervalley time, as in order for a valleytronic application to be useful, the carriers must stay in the valley they are in for enough time for manipulation and readout to occur [211]. Computing the intervalley time and its variation with quantities such as electric field, magnetic field, and strain enables intelligent material and application selection.

4.4 Computational details

The numerical details are as follows. A similar approach is used as in Chapter 2 and Chapter 3, but new quantities are computed and we outline how they are computed here. The total intervalley scattering rate $\Xi_{\mathbf{k}}$ of a state $\mathbf{k}$ can be expressed as:

$$\Xi_{\mathbf{k}} = \sum_{\mathbf{k}'} \Theta_{\mathbf{k}'\mathbf{k}}(1 - \delta_{\mathbf{k}'\mathbf{k}}) \tag{4.1}$$

Here, $\delta_{\mathbf{k}'\mathbf{k}} = 1$ if $\mathbf{k}'$ and $\mathbf{k}$ are in the same valley, and $\delta_{\mathbf{k}'\mathbf{k}} = 0$ if they are in different valleys. We do not make any distinction between valleys on the same axis as the minima in c-BN are at X, meaning such valleys are connected across the Brillouin zone edges. There thus exist three distinct valley types: (100), (010), and (001). We then define the average intervalley scattering time τ_{int} as

$$\tau_{\text{int}} = \frac{1}{N} \sum_{\mathbf{k}} \Xi_{\mathbf{k}} f_{\mathbf{k}} \tag{4.2}$$

As in Chapter 3, we can compute the diffusion coefficient from Eq. (3.14), and for simplicity here we refer to the quantity defined in Eq. (3.14) as the diffusion coefficient.

For all calculations, the electron-phonon matrix elements and electronic structure are computed on a coarse $12 \times 12 \times 12$ grid using DFPT and DFT in Quantum Espresso [72]. The PBE functional was used for the DFT calculations. A wavefunction energy cutoff of 80 Ryd was used for all calculations. A relaxed lattice parameter of 3.623 Å was used, which overestimates the experimental value by only 0.22% [109]. The electronic structure and electron-phonon matrix elements were then interpolated to a fine grid using Perturbo [223]. For all temperatures, a fine grid of $160 \times 160 \times 160$ was used, with a 5 meV Gaussian smearing parameter. Increasing the grid size to $180 \times 180 \times 180$ led to a maximum change of 3.3% in the mobility and maximum change of 8.0% in the diffusion coefficient. An energy window of 383 meV was used. Increasing this energy window to 437 meV led to a maximum change of 0.16% in the mobility and maximum change of 4.0% in the diffusion coefficient. The linear system of equations used to compute the high-field transport properties was then solved by a Python implementation of the GMRES method [63]. For all calculations and temperatures, the Fermi level was adjusted to yield a carrier density of 4×10^{13} cm^{-3}. For all calculations of the diffusion coefficient, a frequency of 1 GHz was used, selected so to ensure that $\omega\tau^{-1} \ll 1$ (where τ is a characteristic relaxation time), while avoiding too low frequencies which result in numerical instabilities.

4.5 Results

Low-field mobility and electric-field dependence of drift velocity

We begin by examining the dependence of the electron drift velocity and mobility on electric field at various temperatures. We first compare our computed low-field mobility with other reported values. At 300 K, we compute a low-field mobility of 1860 cm^{2}V^{-1}s^{-1}. When including two-phonon scattering in the framework described in Refs. [40, 86], the value decreases to 1136 cm^{2}V^{-1}s^{-1}. c-BN has an experimentally reported Hall mobility value of 825 cm^{2}V^{-1}s^{-1} [212] (although much lower values have been reported [81, 90, 156]), and previously computed ab-initio values range from 1230 cm^{2}V^{-1}s^{-1} (Ref. [95]) to 1610 cm^{2}V^{-1}s^{-1} (Ref. [186]). Our mobility values are thus in reasonable agreement with prior computed and experimental values.

We note that for the rest of this work, only one-phonon scattering is considered. We find that adding two-phonon scattering decreases the mobility at all temperatures by roughly 40%, and the qualitative features of the mobility and diffusion coefficient versus electric field are generally retained. These findings are similar to those in Refs. [40, 86]. Therefore, to reduce computational cost, we consider only one-phonon scattering as is typically assumed.

Next, we examine the drift velocity versus electric field at 300 K in Fig. 4.3a. At sufficiently high electric fields, we observe an anisotropy in the drift velocity despite the cubic symmetry of the crystal, with the drift velocity in the [100] direction being less than that in the [111] by around 4% at 3 kV cm^{-1}. This anisotropy is present with greater magnitude at 200 K, as seen in Fig. 4.3b. We also note that as the temperature decreases, the onset of a discernible difference in drift velocity between the two directions occurs at a lower field. The anisotropy arises due to differences in the average energy of the electron distribution function between the longitudinal and transverse valleys [32, 45], as discussed in more detail below.

At 130 K, a qualitative change in the [100] drift velocity characteristics is seen in Fig. 4.3c as an abrupt decrease in drift velocity above $\approx$ 500 V cm^{-1}. The effect is even more pronounced at 77 K, with the drift velocity dropping 25% within only 20 V cm^{-1}. This NDR effect is well-known in semiconductors such as GaAs, forming the basis for Gunn diodes, as outlined in Section 4.2. For these materials, NDR is caused by intervalley scattering of electrons from the primary, high-mobility valley at Γ to a satellite valley with higher effective mass such as the L valley in GaAs. However, this explanation is not applicable in c-BN as we calculate that the next-lowest-energy satellite valley is 2.44 eV higher than the conduction band minimum, as seen in Fig. 4.1. This energy is sufficiently large that it plays a negligible role in the transport in the electric field range used in this work.

Valley repopulation and intervalley time

In diamond, NDR has been experimentally observed when the electric field is oriented along the [100] direction, despite lacking the two-valley band structure required for the conventional NDR mechanism [96]. In this case, NDR was attributed to the sudden onset of intervalley scattering associated with zone-edge longitudinal acoustic phonon emission, which causes an abrupt repopulation from valleys transverse to the electric field to those parallel to it [96]. This repopulation occurs only at a high enough electric field value where the threshold for longitudinal acous-

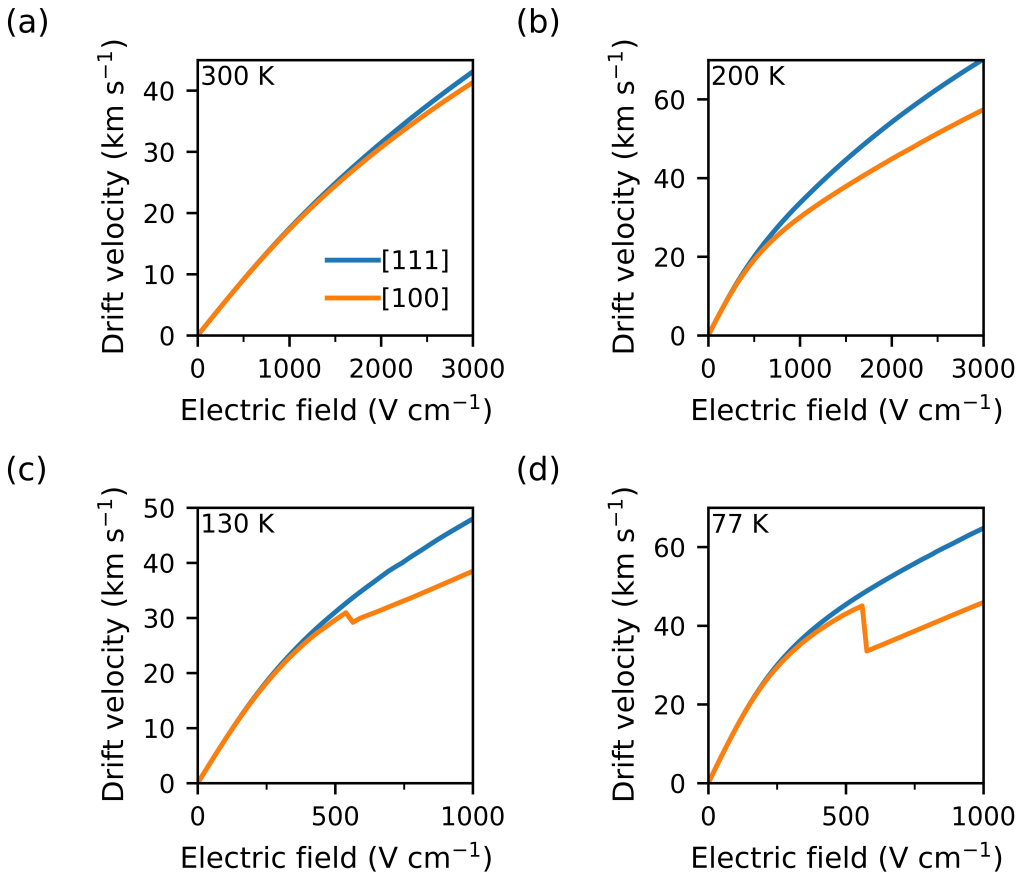

Figure 4.3: Computed drift velocity versus electric field at (a) 300 K, (b) 200 K, (c) 130 K, and (d) 77 K, with field applied along the [100] direction (orange line) and [111] direction (blue line).

tic intervalley phonon emission is reached. As c-BN has a similar band structure to diamond with six equivalent conduction band minima, we hypothesize that a similar explanation is applicable. To test the hypothesis, we computed the energy dependence of the electron-phonon scattering rates. The result at 77 K is shown in Fig. 4.4. Indeed, we observe that below the optical phonon energy of ~150 meV, the scattering rates have a relatively weak dependence on energy, while the scattering rates abruptly increase above the optical phonon energy.

The strong energy-dependence of the scattering rates has consequences for the relative occupation in the various valleys and ultimately the transport properties. Below the threshold field, few electrons have sufficient energy to scatter to an inequivalent valley, and the [100], [010], and [001] valleys react to the electric field largely independently. In addition, owing to the lower effective mass of the

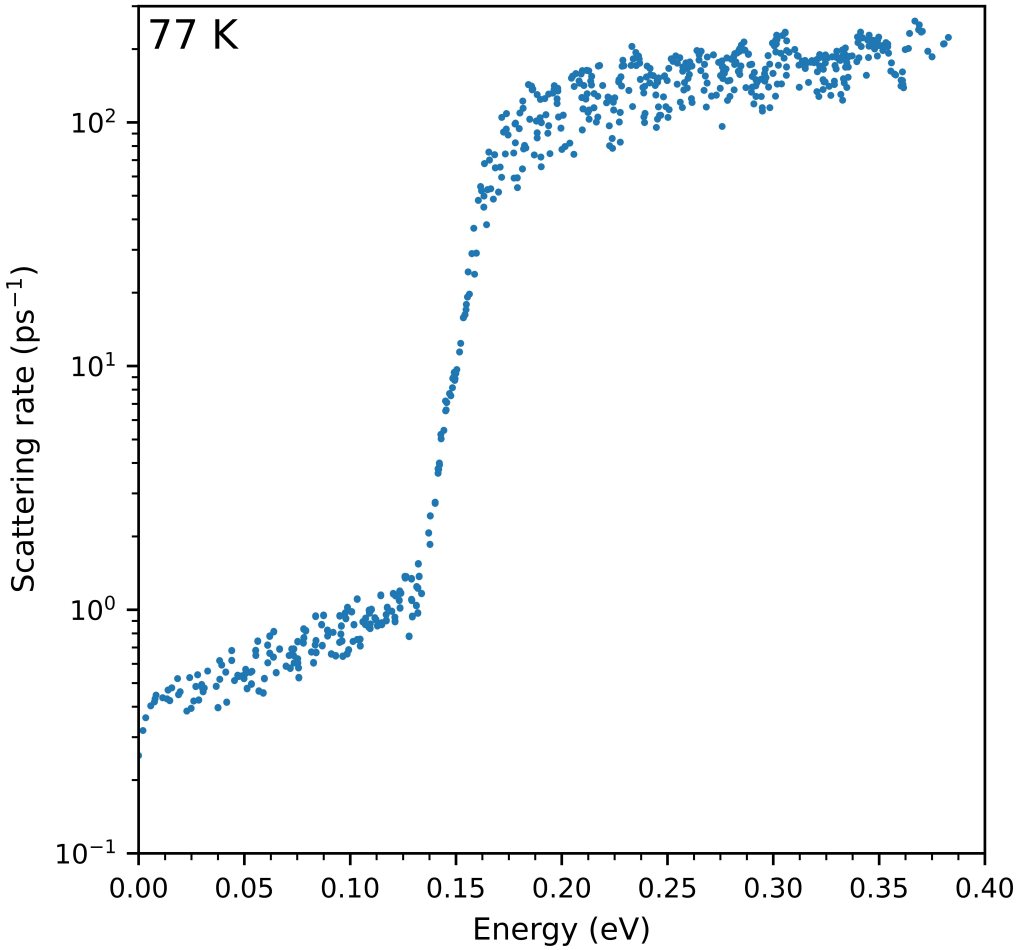

Figure 4.4: Electron scattering rate versus energy for c-BN at 77 K. The large optical phonon threshold can be seen at ~150 meV.

transverse valleys relative to longitudinal ones ($0.36m_0$ versus $0.95m_0$ for transverse and longitudinal, respectively), transverse valleys have a higher effective carrier temperature than the longitudinal valleys at a given field, as shown in Fig. 4.5. The effective valley temperatures are defined by computing the average energies of the steady distributions at the given field and identifying the temperature of a Boltzmann distribution with the same average energy. The valley temperature is a measure of the average energy of the distribution rather than a thermodynamic temperature. As the field increases, the transverse valleys achieve a higher steady-state temperature owing to their lower effective mass. The higher electron temperature of the transverse valleys also leads to the drift velocity anisotropy between [100] and [111] directions shown in Fig. 4.3. This phenomenon is similar to what is shown schematically in Fig. 2.2 in n-Si, but exaggerated as the mechanisms to equilibrate the valley

populations do not exist at low electric field values.

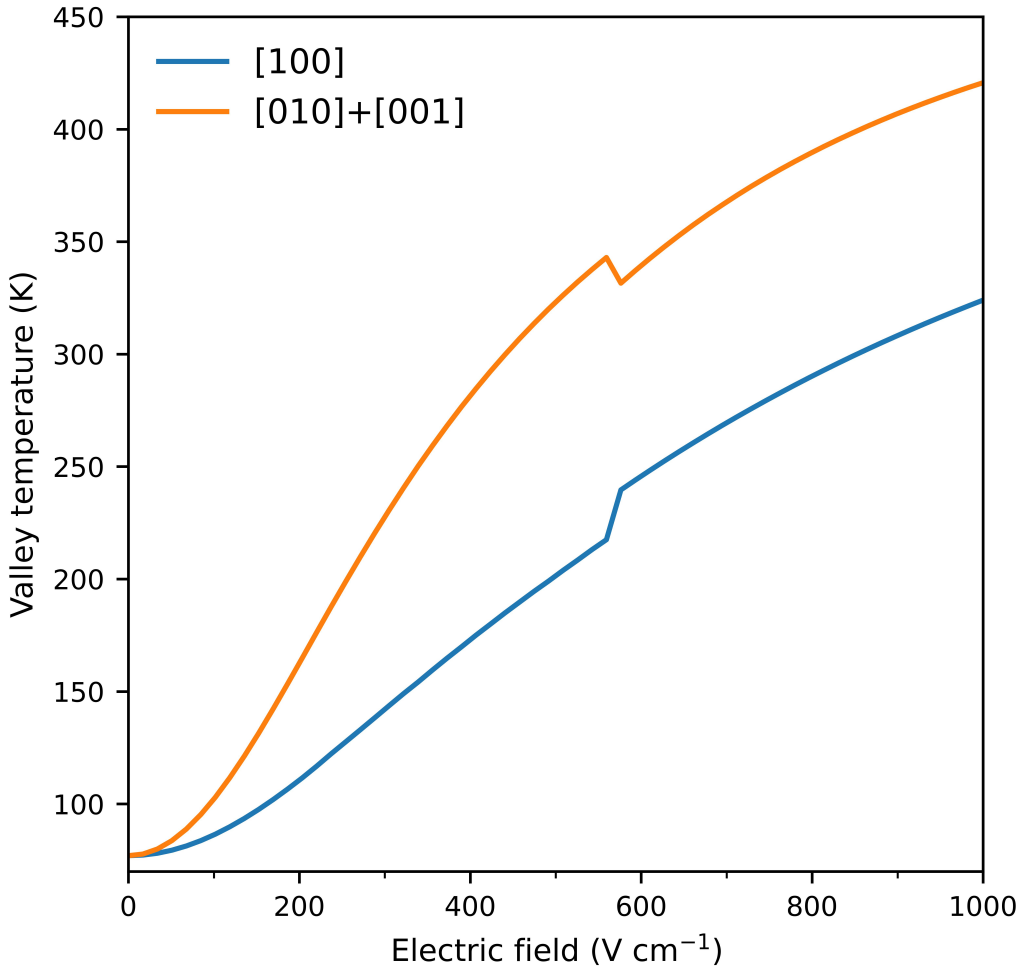

Figure 4.5: Valley temperature versus electric field for c-BN at 77 K with the electric field applied in the [100] direction. The [100] type valleys are shown in blue, and [010]+[001] type valleys are shown in orange.

At the threshold field, electrons in the transverse valleys gain enough energy to emit optical phonons and undergo an intervalley transition to the longitudinal valleys. This repopulation effect is shown in Fig. 4.6 at 77 K, which plots the population of the [100] type valleys in comparison to the sum of the [010] and [001] type valleys versus electric field, with the field applied in the [100] direction. At zero field, all valleys have the same population. As the field increases from zero, there is little population redistribution due to the absence of a significant intervalley scattering by phonon emission and the weak absorption-mediated scattering at 77 K. Even at 500 V cm^{-1}, the [100] type valleys have less than 40% of the population. However, once the threshold field is reached ($\approx$ 560 V cm^{-1}), a redistribution to

the [100] longitudinal valleys occurs. Because the longitudinal mass is higher than the transverse mass, the drift velocity abruptly decreases. This repopulation effect occurs at all temperatures when the field is applied in any cubic axis, but NDR only manifests in the transport properties when phonon-absorption intervalley scattering is negligible compared to emission-mediated scattering, in this case at temperatures below around 140 K.

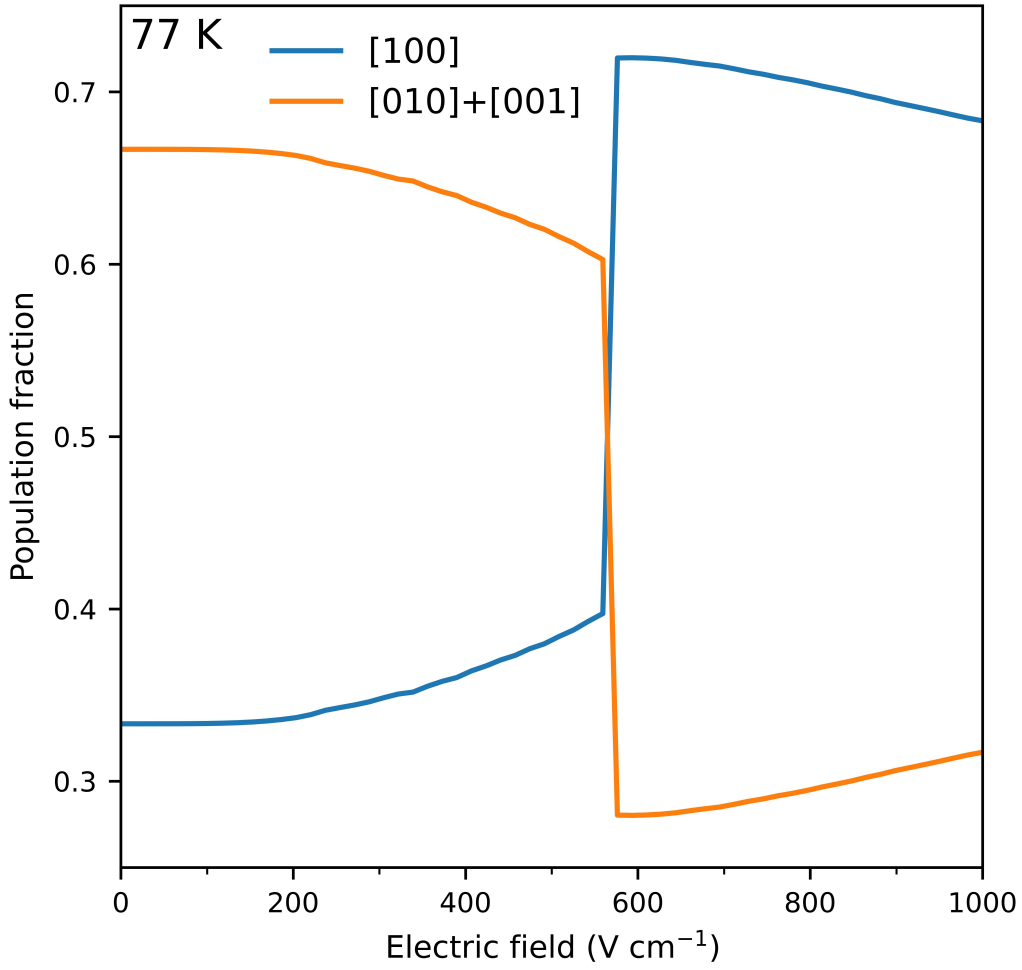

Figure 4.6: Population fraction versus electric field for c-BN at 77 K with the electric field applied in the [100] direction, for [100] type valleys (blue) and the sum of the [010] and [001] type valleys (orange).

The high optical phonon energy in c-BN has consequences for intervalley scattering, which must be mediated by zone-edge modes due to momentum conservation. For sufficiently low fields, most electrons do not have sufficient energy to scatter via an intervalley phonon emission process. Further, the high optical phonon energy of c-BN leads to low thermal occupation even at 300 K, relative to conventional

semiconductors like GaAs. As a result, both absorption and emission-mediated intervalley scattering are weak in c-BN, and so the corresponding average intervalley relaxation time is expected to be long in comparison to other semiconductors with lower phonon energies.

In Fig. 4.7, we show the intervalley time versus electric field along the [100] direction at 77 K. At low field ($\approx$1 V cm^{-1}), the intervalley relaxation time is calculated to be 5.3 μs. For comparison, we also computed the intervalley relaxation time in diamond, obtaining a value of 2.4 μs. c-BN thus has an intervalley relaxation time at low fields nearly 100% larger than that of diamond. We note that the value decreases with increasing electric field as electrons are able to emit zone-edge phonons and scatter to other valleys. However, the relatively long intervalley time suggests that c-BN may be promising in valleytronic applications.

Electric-field dependence of hot-electron diffusion coefficient

Experimental tests of these predictions are challenging owing to the difficulties in preparing high-quality thin films of c-BN. We suggest an approach to mitigate this challenge based on measurement of the current noise power spectral density (PSD), or equivalently in the low-frequency limit, the diffusion coefficient. Due to the long intervalley scattering time in c-BN, we expect a clear intervalley noise contribution arising from electrons scattering between valleys with distinct effective masses when the electric field is applied in the [100] direction. Intervalley noise manifests in experiment as an anisotropy in the diffusion coefficient, with the value being larger along the direction with inequivalent valleys relative to the case in which all valleys are equivalent [84, 167]([100] valleys versus [111] valleys, respectively, for c-BN).

More precisely, the general expression for the intervalley diffusion coefficient is given by Eq. (3.1), and in the present case, the valley types 1 and 2 refer to longitudinal and transverse valleys defined by the field direction. Thus, intervalley noise will manifest as an increase in the [100] diffusion coefficient over the [111] diffusion coefficient, with the precise amount depending on the quantities in Eq. (3.1) at each field.

In Fig. 4.8, we show the electric field dependence of the diffusion coefficient for 300 K and 77 K. At 300 K in Fig. 4.8a, we observe that the diffusion coefficient monotonically decreases with increasing field along the [111]. This behavior is similar to what is seen in n-Si [85], and it occurs when the scattering rates increase

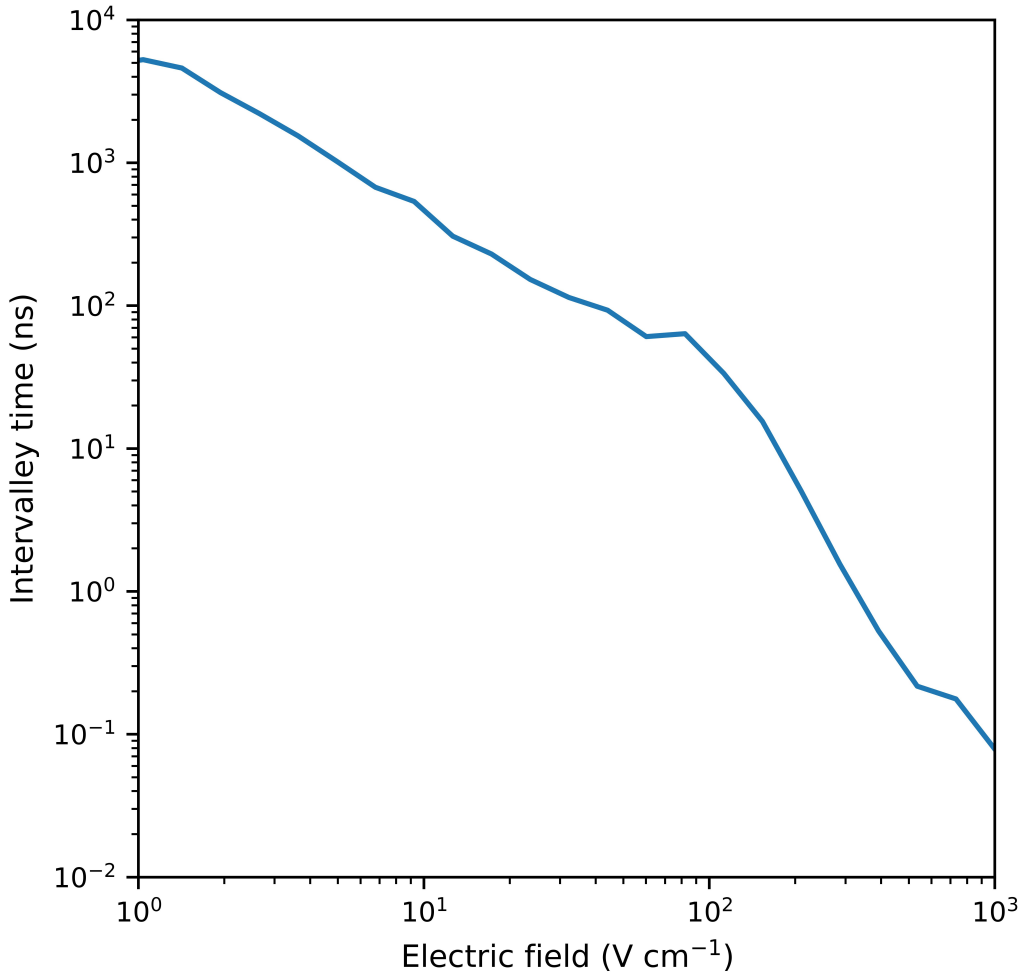

Figure 4.7: Average intervalley relaxation time versus electric field for c-BN at 77 K, with the electric field applied in the [100] direction. The intervalley time is on the order of microseconds at low fields, rivaling that of diamond.

sufficiently strongly with increasing energy [5, 29, 43]. For the [100] direction, however, a higher diffusion coefficient value and a non-monotonic trend with electric field are seen. At 300 K in Fig. 4.8a, we observe that the diffusion coefficient peak when the electric field is applied in the [100] direction leads to a non-monotonic trend, with a peak around 2% higher than the equilibrium value. We attribute this peak to the contribution of intervalley noise, although the magnitude of the peak may be difficult to detect experimentally.

Figure 4.8b shows the corresponding results at 77 K. Along the [111], a non-monotonic trend is observed despite the expected absence of intervalley noise. This feature can be partially explained using the generalization of the Einstein relation applied to high fields in Eq. (3.3). Figure 4.9a shows the average energy versus

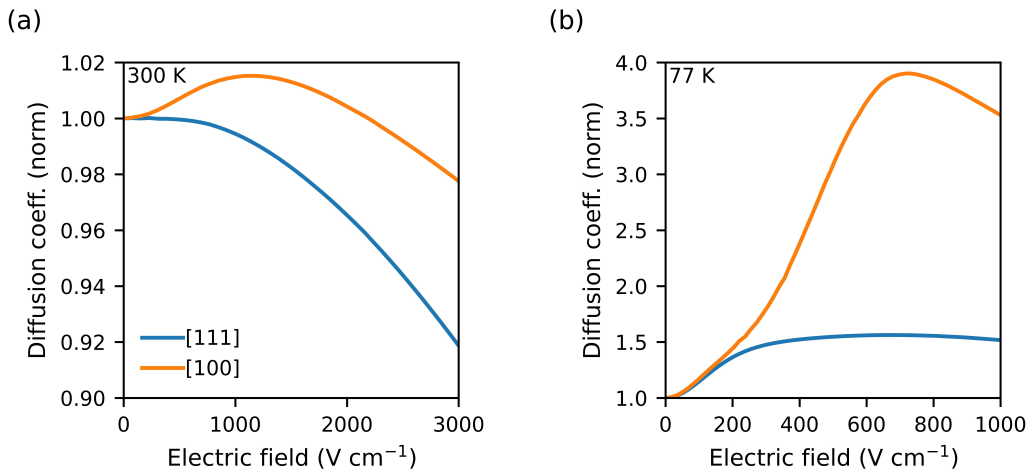

Figure 4.8: Computed electron diffusion coefficient versus electric field at (a) 300 K and (b) 77 K, with field applied along the [100] direction (orange line) and [111] direction (blue line). A pronounced peak in the [100] diffusion coefficient is observed at 77 K, which is attributed to intervalley diffusion.

electric field when the field is oriented in the [111], and Fig. 4.9b shows the mobility versus electric field. With these two quantities, we can calculate an approximation for the high-field diffusion coefficient. This approximation versus the original computed result is shown in Fig. 4.10. While the magnitude of the increase is greater in the modified Einstein approximation result, and a decrease in the diffusion coefficient is observed at $\sim$ 700 V cm^{-1} in the approximation, the approximation confirms an initial increase in the diffusion coefficient. Due to a weak dependence of scattering rates on energy below the optical phonon energy as seen in Fig. 4.4, the average electron energy exhibits a stronger dependence on electric field than the mobility. As a result, the diffusion coefficient initially increases with increasing field.

In the [100] direction, the peak is markedly larger compared to the [111] case, with the peak value of the [100] diffusion coefficient at $\approx$700 V cm^{-1} being nearly 300% larger than the equilibrium value. The effect is much larger at 77 K compared to at 300 K. Such large peaks in the diffusion coefficient have been observed experimentally for other materials such as GaAs [14, 70, 181] but have not been seen in first-principles calculations [40] until now. Monte Carlo calculations of the diffusion coefficient in diamond at 300 K have found a slight increase of the diffusion coefficient with electric field [159], similar to what is observed here in c-BN at 300 K. The magnitude of the peak at low temperatures is sufficiently large that it could easily be discerned in experiment, and its detection would support the

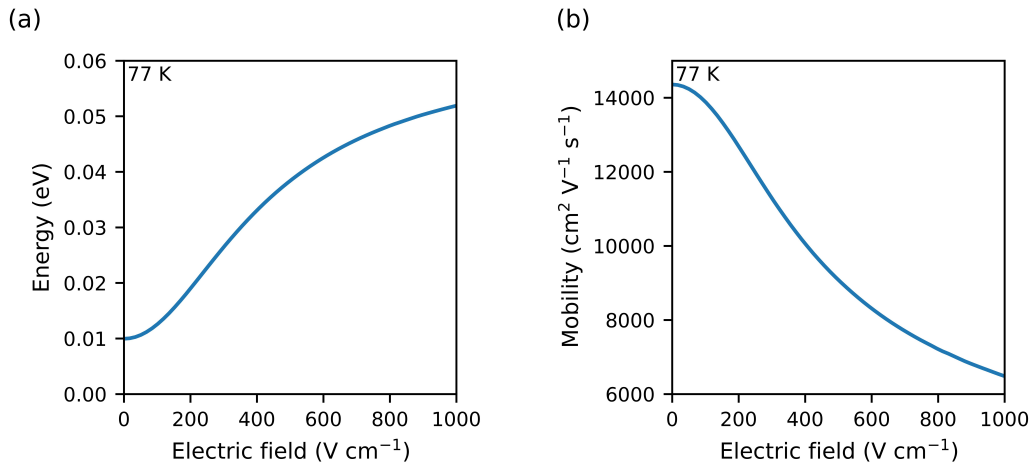

Figure 4.9: (a) Average electron energy versus electric field and (b) mobility versus field for c-BN at 77 K. For both cases, the electric field is applied in the [111].

prediction of the long intervalley time in c-BN.

4.6 Discussion

Our first-principles calculations have predicted that c-BN exhibits a region of NDR and a long intervalley lifetime rivaling that of diamond. These properties may find useful device applications. In materials with a pronounced NDR region, instabilities in electric current will lead to the formation of charged domains [76], which can be utilized in Gunn oscillators for various microwave applications. As a Gunn oscillator has been constructed with diamond thin films [202] it is possible that such devices could be realized in c-BN. We note that in both cases, the devices would need to operate below room temperature.

Experimental characterization of the NDR region can also provide insight into the role of 2ph scattering in c-BN. While in this work we have employed the 1ph level of theory, 2ph scattering was found to reduce the predicted mobility by $\approx 40\%$, in line with the reduction reported for other semiconductors [52, 86, 123]. 2ph scattering also shifts the electron distribution to lower energies at a given field, which in turn would cause the threshold field for NDR to occur at ≈ 1120 V cm^{-1} than the 560 V cm^{-1} at the 1ph level of theory. If sufficiently pure samples were available, the difference in threshold field should be discernible.

For valleytronics, it is essential that electrons within a valley remain there long enough to perform the desired function [211]. For c-BN, at equilibrium, our calcu-

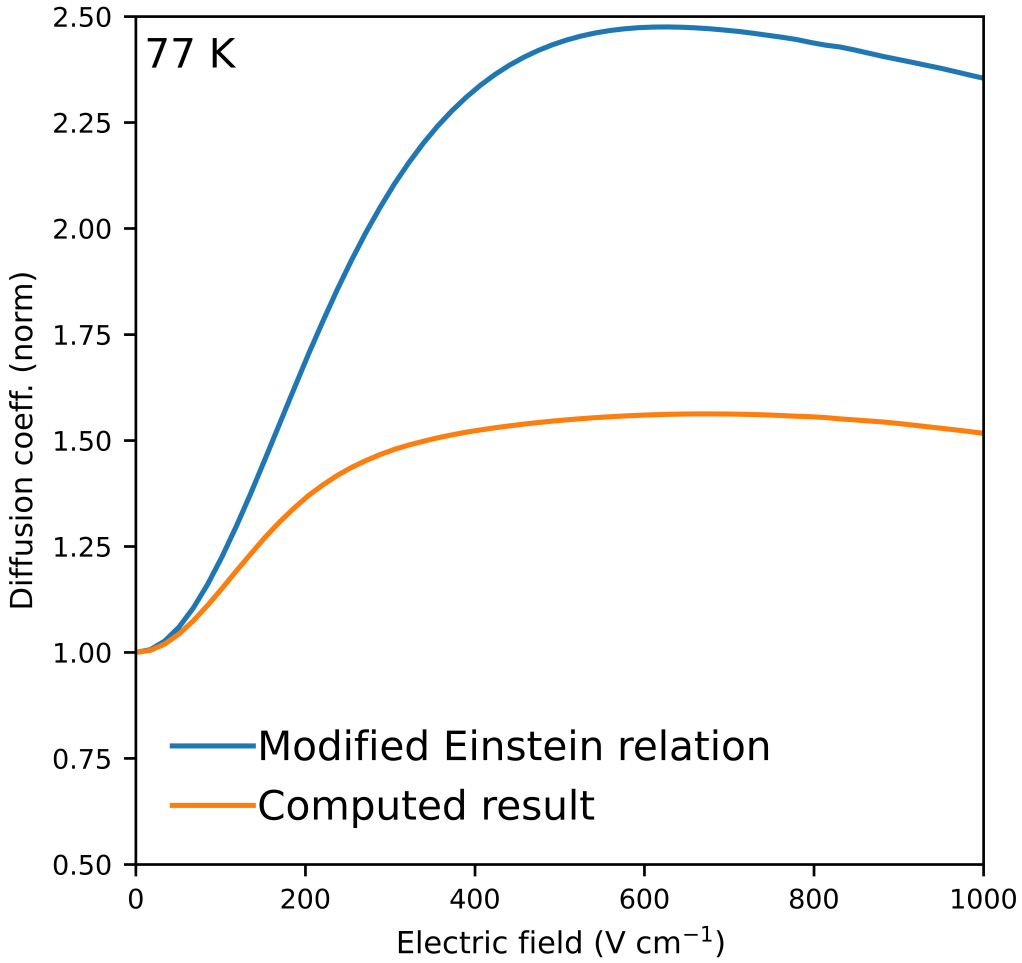

Figure 4.10: (a) Average electron energy versus electric field and (b) mobility versus field for c-BN at 77 K. For both cases, the electric field is applied in the [111].

lated intervalley time of 5.3 μs at 77 K is significantly greater than the 300 ns value for diamond, calculated from Monte Carlo simulation [97] and the value of 2.4 μs we computed. It also greatly exceeds the intervalley time of typical semiconductors; for instance, we compute the intervalley time of n-Si to only be 149 ps at the same temperature. However, due to the strong decrease of the intervalley time with increasing field seen in Fig. 4.7, some optimization may be required to use c-BN in valleytronic applications. A potential route to increase the intervalley relaxation time further is by leveraging the compressive strain present in most c-BN thin films. Strain would break the degeneracy of the six equivalent valleys, further inhibiting intervalley scattering and leading to an increase in intervalley relaxation time.

4.7 Summary

Cubic boron nitride (c-BN) is a novel ultra-wide-bandgap semiconductor with technological promise due to its predicted high breakdown field and saturation drift velocity, but has not been investigated in depth away from equilibrium with ab-initio methods or in experiments. We have computed the high-field transport properties and diffusion coefficient of c-BN from first-principles from 77 – 300 K. We find that below 140 K, c-BN exhibits a region of negative differential resistance arising from the strong energy dependence of the scattering rates around the optical phonon energy, indicating the potential of c-BN in transferred-electron devices. The high optical phonon energy in conjunction with c-BN's anisotropic band structure also leads to a calculated intervalley time comparable to that of diamond, suggesting that c-BN could be a promising material for valleytronic applications.

We also show that our predictions can be tested by identifying a non-monotonic trend of the diffusion coefficient versus electric field. Our work highlights the potential electron device applications of c-BN beyond conventional power electronics, and stimulates further experimental investigation into the synthesis and electrical transport properties of c-BN thin films by suggesting techniques to confirm our computations and to ameliorate the potential obstacles in using c-BN in devices.

Chapter 5

CONCLUSION AND OUTLOOK

This thesis has focused on using first-principles methods to investigate high-field transport and noise properties in semiconductors. In Chapter 1, we introduced the theoretical background of the problem of the electron-phonon interaction, and outlined the computational approach we use to obtain the electron-phonon matrix elements utilized in our BTE solver. In addition, we gave a short summary of hot-electron noise, and the advantages of an ab-initio approach to solve for both transport and fluctuational observables.

In Chapter 2, we introduced the widely utilized semiconductor n-Si, and its band structure and phonon dispersion. We then went in depth of how, starting with the Boltzmann transport equation for a spatially homogeneous and nondegenerate electron gas, we can solve a linear system in order to obtain high-field transport properties like the drift velocity. In order to provide an intermediate observable to characterize the heating of the electron gas, between the linear response of the low-field mobility and the high-field drift velocity, we introduce the warm electron tensor or β. We found that the qualitative features of the dependence of β on electric field orientation are described correctly at the normal one-phonon level of theory, but that the magnitude of β is overestimated by over 100% over a wide range of temperatures. To address this, we investigated the effect of including the next-to-leading order term in the electron-phonon perturbative expansion, by including one-electron-two-phonon (2ph) scattering. We find that including 2ph scattering causes near-quantitative agreement with experimental values of β, showing that 2ph is important even in nonpolar semiconductors.

In Chapter 3, we continued our study of n-Si, by investigating the hot-electron diffusion coefficient. To do this, we showed how we are able to solve for fluctuational observables using the BTE, in a similar manner to how we solved for transport properties. We found that while we correctly predicted the qualitative features of the diffusion coefficient anisotropy, such as the sign of the anisotropy at high fields, we predicted a much smaller intervalley noise contribution than in experiments, and this contribution also manifested at much larger fields than in experiments. The most obvious explanation for this discrepancy between computation and experiment is an

incorrect description of f-type scattering. However, by investigating the frequency dependence of the diffusion coefficient and the piezoresistivity, we showed that the good qualitative agreement of these quantities with experiment excluded the idea of f-type scattering being overestimated in our computation. Instead, we suggested that the measured diffusion coefficient may be influenced by real-space gradients and space charge effects, not included in our electron-phonon scattering description. Our work shows the care that must be taken when attempting to explain experimental diffusion measurements with microscopic charge transport processes.

In Chapter 4, we applied the approach to solve for high-field transport properties outlined in Chapter 2 and the approach to calculate high-field diffusion coefficients outlined in Chapter 3 to the novel ultra-wide bandgap semiconductor, cubic boron nitride (c-BN). While c-BN is known for its excellent mechanical and thermal properties, past studies have indicated it has excellent electronic properties such as an extremely high breakdown field and saturation drift velocity. While these properties in theory make c-BN an excellent candidate for usage in high-power and high-frequency devices, very few experimental or theoretical studies have been conducted on the electronic properties of c-BN away from low field. We found that c-BN exhibits a distinct NDR region below 140 K, through an unusual mechanism where when electrons reach the high optical phonon energy threshold, they repopulate from high- to low-energy valleys. A second consequence of this high optical phonon energy is the extremely high intervalley time at low electric fields, comparable to diamond. The NDR region and large intervalley time indicate that c-BN is a promising candidate for transferred-electron and valleytronic devices, respectively. Our work shows the potential of c-BN beyond the usually suggested high-power and high-frequency applications, stimulating further theoretical and experimental investigation into this novel semiconductor.

Future Work

Here, we discuss some possible new avenues of investigation that are motivated by our findings.

Inclusion of full electron-two-phonon interaction

We noted in Section 2.4 that we only included two-phonon events consisting of consecutive one-phonon events, mediated by an intermediate state, and not the two-phonon scattering corresponding to an electron simultaneously interacting with two

phonons. The first type of two-phonon scattering corresponds to the first derivative with respect to the interatomic potential, taken to second order in perturbation theory, while the second corresponds to the second-order derivative of the interatomic potential. While these two types of 2ph scattering have been shown to cancel in the limit of long-wavelength acoustic phonons, it is unclear about the full extent of this cancellation and the effect of it on transport properties. A further investigation of the full electron-two-phonon interaction would aid understanding of this.

Investigating transport properties and noise in 2D materials

A similar approach to what is outlined in Section 2.3 has been used to calculate the transport properties away from equilibrium [137] and the ultrafast dynamics [209] of graphene, as well as the low-field transport properties of large-angle twisted bilayer graphene [68]. However, the electronic properties of very few two-dimensional materials have been investigated using first-principles, and the noise properties have not been reported for any material using a fully ab-initio method. However, in principle there are very few impediments to using the approach outlined in Section 2.3 and Section 3.4 for two-dimensional materials, and our group has begun to compute high-field noise properties in MoS_2. As most valleytronic materials are two-dimensional [188], using this computational approach would help identify promising materials for this type of application, as the intervalley time can be directly predicted. In addition, more understanding of the noise properties for two-dimensional materials could be gained by computing fluctuational observables from first-principles.

Inclusion of length-dependence in the BTE framework

In this work, length-dependence was neglected, and the BTE was solved solely in momentum space — in principle, for an infinite sample bar. However, in order to work towards using computational tools to be predictive of phenomena in devices, it is imperative to take into account length-dependence, as we expect important length-dependent changes in the noise at frequencies $\omega\tau_m < 1$, where τ_m is the relaxation time corresponding to the process responsible for the noise source [84]. For instance, it has been found that intervalley noise can be suppressed by changing the length of the sample [14]. Incorporating some degree of length dependence from first-principles (for instance, confinement in one dimension) would give a more mechanistic understanding of noise processes in devices.

Incorporating ab-initio ionized-impurity scattering

In this work, only scattering between electrons and phonons were considered, and when ionized-impurity scattering was briefly introduced in Section 3.6, it was only the simple Brooks-Herring formula due to ease of implementation [131]. It has been shown that in multivalley semiconductors with anisotropic bands, the Brooks-Herring treatment of impurity scattering is insufficient and leads to an order-of-magnitude discrepancy in ionized-impurity-limited mobility values [65]. However, approaches to include ionized-impurity scattering [125] and electron-defect scattering [133] first-principles have been reported recently, and the low-field mobility for basic semiconductors have been computed. A significant amount of ionized-impurity scattering would cause valley depolarization in valleytronic materials [96], and an accurate description of ionized-impurity scatering is crucial at low temperatures to compute high-field transport properties. An improvement on our work would be to be the first to include both electron-phonon and ionized-impurity scattering away from low fields, and to accurately predict the effect of impurity concentration on quantities such as the intervalley time.

Investigating transferred-electron devices and intervalley time using c-BN

In Chapter 4, we showed how our computations predicted a NDR region and large intervalley time in c-BN, which are indicators of good suitability in transferred-electron devices and valleytronic applications, respectively. However, very few experimental measurements have been made of the electronic properties of c-BN away from equilibrium, limited to voltage versus current at small voltage values [12]. With recent improvements in synthesis of thin films of c-BN, more measurements at different temperatures can be recorded. Importantly, it should be straightforward to test the hypothesis in Chapter 4 of the NDR region below 140 degrees. While directly observing the intervalley time is more complicated, using the noise characteristics at low temperature as a proxy for this as suggested in Section 4.5 should be attainable, using (for instance) the time-of-flight method. In order to progress to novel devices using c-BN, these properties must be confirmed first.

Bibliography

[1] Zlatan Aksamija and Umberto Ravaioli. Joule heating and phonon transport in silicon mosfets. *Journal of Computational Electronics*, 5(4):431–434, 2006. doi: 10.1007/s10825-006-0045-2. URL https://doi.org/10.1007/s10825-006-0045-2.

[2] Ya.I. Al'ber, A.A. Andronov, V.A. Valov, V.A. Kozlov, and I.R. Ryazantseva. Hot electron population inversion and cyclotron resonance negative differential conductivity in semiconductors. *Solid State Communications*, 19 (10):955–959, 1976. ISSN 0038-1098. doi: https://doi.org/10.1016/0038-1098(76)90629-3. URL https://www.sciencedirect.com/science/article/pii/0038109876906293.

[3] Gerald P. Alldredge and F. J. Blatt. On the role of two-phonon processes in the energy relaxation of a heated-electron distribution. *Annals of Physics*, 45 (2):191–231, November 1967. doi: 10.1016/0003-4916(67)90123-6.

[4] Hiroshi Amano, Masahiro Kito, Kazumasa Hiramatsu, and Isamu Akasaki. P-type conduction in mg-doped gan treated with low-energy electron beam irradiation (leebi). *Japanese journal of applied physics*, 28(12A):L2112, 1989.

[5] V. Aninkevičius, V. Bareikis, J. Liberis, A. Matulionis, and P. Sakalas. Comparative analysis of microwave noise in gaas and algaas/gaas channels. *Solid-State Electronics*, 36(9):1339 – 1343, 1993. ISSN 0038-1101. doi: https://doi.org/10.1016/0038-1101(93)90174-O. URL http://www.sciencedirect.com/science/article/pii/003811019390174. "http://www.sciencedirect.com/science/article/pii/0038110193901740".

[6] M. Asche and O. G. Sarbei. Electric conductivity of hot carriers in si and ge. *physica status solidi (b)*, 33(1):9–57, 1969. doi: https://doi.org/10.1002/pssb.19690330102. URL https://onlinelibrary.wiley.com/doi/abs/10.1002/pssb.19690330102.

[7] M. Asche and O. G. Sarbei. Electron–phonon interaction in n-si. *physica status solidi (b)*, 103(1):11–50, 1981. doi: https://doi.org/10.1002/pssb.2221030102. URL https://onlinelibrary.wiley.com/doi/abs/10.1002/pssb.2221030102.

[8] M. Asche, V.M. Vasetskii, A.G Maksimchuk, and O.G. Sarbei. Electron scattering in n-silicon. *Ukrainskii fizicheskii zhurnal / Akademiia nauk Ukrainskoi SSR, Otdelenie fiziki*, 15:1692–1700, 1970.

[9] M. Asche, B. L. Boichenko, V. M. Bondar, and O. G. Sarbei. Influence of electron-electron scattering on the anisotropic conductivity at high electric

fields in si. *physica status solidi (b)*, 44(1):173–182, 1971. doi: https://doi.org/10.1002/pssb.2220440117. URL https://onlinelibrary.wiley.com/doi/abs/10.1002/pssb.2220440117.

[10] W. Baechtold. Noise behavior of gaas field-effect transistors with short gate lengths. *IEEE Transactions on Electron Devices*, 19(5):674–680, 1972. doi: 10.1109/T-ED.1972.17473.

[11] M. N. Baibich, J. M. Broto, A. Fert, F. Nguyen Van Dau, F. Petroff, P. Etienne, G. Creuzet, A. Friederich, and J. Chazelas. Giant magnetoresistance of (001)fe/(001)cr magnetic superlattices. *Phys. Rev. Lett.*, 61:2472–2475, Nov 1988. doi: 10.1103/PhysRevLett.61.2472. URL https://link.aps.org/doi/10.1103/PhysRevLett.61.2472.

[12] I.S. Bam, V.M. Davidenko, V.G. Sidorov, L.I. Fel'dgun, M.D. Shagalov, and Yu.K. Shalabutov. Electrical properties of cubic boron nitride. *Fizika i Tekhnika Poluprovodnikov*, 10:554–556, 1976.

[13] J. Bardeen and W. Shockley. Deformation potentials and mobilities in non-polar crystals. *Phys. Rev.*, 80:72–80, Oct 1950. doi: 10.1103/PhysRev.80.72. URL https://link.aps.org/doi/10.1103/PhysRev.80.72.

[14] V. Bareikis, V. Viktoravicius, A. Galdikas, and R. Miliusyte. Microwave Noise and Constant of the Coupling Between the Valleys Gamma and l in a Three-Valley Model of GaAs. *Sov. Phys. Semicond.*, 14(7):847–849, 1980.

[15] V. Bareikis, V. Viktoravichyus, and A. Galdikas. Frequency dependence of noise in n-type si in high electric fields. *Soviet Physics Semiconductors*, 16: 1202–1203, 1982.

[16] Stefano Baroni, Stefano de Gironcoli, Andrea Dal Corso, and Paolo Giannozzi. Phonons and related crystal properties from density-functional perturbation theory. *Rev. Mod. Phys.*, 73:515–562, Jul 2001. doi: 10.1103/RevModPhys.73.515. URL https://link.aps.org/doi/10.1103/RevModPhys.73.515.

[17] P. K. Basu and B. R. Nag. Infrared free-carrier absorption in n-type silicon. *physica status solidi (b)*, 53(1):K61–K64, 1972. doi: https://doi.org/10.1002/pssb.2220530158. URL https://onlinelibrary.wiley.com/doi/abs/10.1002/pssb.2220530158.

[18] A. BenMoussa, A. Soltani, U. Schühle, K. Haenen, Y.M. Chong, W.J. Zhang, R. Dahal, J.Y. Lin, H.X. Jiang, H.A. Barkad, B. BenMoussa, D. Bolsee, C. Hermans, U. Kroth, C. Laubis, V. Mortet, J.C. De Jaeger, B. Giordanengo, M. Richter, F. Scholze, and J.F. Hochedez. Recent developments of wide-bandgap semiconductor based uv sensors. *Diamond and Related Materials*, 18(5):860–864, 2009. ISSN 0925-9635. doi: https://doi.org/10.1016/j.diamond.2008.11.013. URL https://www.sciencedirect.com/

science/article/pii/S0925963508005669. Proceedings of Diamond 2008, the 19th European Conference on Diamond, Diamond-Like Materials, Carbon Nanotubes, Nitrides and Silicon Carbide.

[19] Marco Bernardi. First-principles dynamics of electrons and phonons. *The European Physical Journal B*, 89(11):239, 2016. doi: 10.1140/epjb/e2016-70399-4. URL https://doi.org/10.1140/epjb/e2016-70399-4.

[20] M. Bester. Phaselock system for millimeter-wave Gunn oscillators used in radio astronomy and laboratory spectroscopy. *International Journal of Infrared and Millimeter Waves*, 7(1):43–63, January 1986. doi: 10.1007/BF01011061.

[21] Sabpreet Bhatti, Rachid Sbiaa, Atsufumi Hirohata, Hideo Ohno, Shunsuke Fukami, and S.N. Piramanayagam. Spintronics based random access memory: a review. *Materials Today*, 20(9):530–548, 2017. ISSN 1369-7021. doi: https://doi.org/10.1016/j.mattod.2017.07.007. URL https://www.sciencedirect.com/science/article/pii/S1369702117304285.

[22] Ya.M. Blanter and M. Büttiker. Shot noise in mesoscopic conductors. *Physics Reports*, 336(1–2):1–166, September 2000. ISSN 0370-1573. doi: 10.1016/s0370-1573(99)00123-4. URL http://dx.doi.org/10.1016/S0370-1573(99)00123-4.

[23] Felix Bloch. Über die quantenmechanik der elektronen in kristallgittern. *Zeitschrift für Physik*, 52(7):555–600, 1929. doi: 10.1007/BF01339455. URL https://doi.org/10.1007/BF01339455.

[24] A. D. Boardman, W. Fawcett, and H. D. Rees. Monte Carlo calculation of the velocity-field relationship for gallium arsenide. *Solid State Communications*, 6(5):305–307, May 1968. doi: 10.1016/0038-1098(68)90110-5.

[25] A. D. Boardman, W. Fawcett, and J. G. Ruch. Monte carlo determination of hot electron galvanomagnetic effects in gallium arsenide. *physica status solidi (a)*, 4(1):133–141, 1971. doi: https://doi.org/10.1002/pssa.2210040114. URL https://onlinelibrary.wiley.com/doi/abs/10.1002/pssa.2210040114.

[26] T.H. Borst and O. Weis. Electrical characterization of homoepitaxial diamond films doped with b, p, li and na during crystal growth. *Diamond and Related Materials*, 4(7):948–953, 1995. ISSN 0925-9635. doi: https://doi.org/10.1016/0925-9635(94)00263-0. URL https://www.sciencedirect.com/science/article/pii/0925963594002630.

[27] Jesse M. Brown, Saurabh Vishwakarma, David J. Smith, and Robert J. Nemanich. Nucleation of cubic boron nitride on boron-doped diamond via plasma enhanced chemical vapor deposition. *Journal of Applied Physics*, 133(21):215303, 06 2023. ISSN 0021-8979. doi: 10.1063/5.0145771. URL https://doi.org/10.1063/5.0145771.

[28] M.A.C.S. Brown. Deviations from ohm's law in germanium and silicon. *Journal of Physics and Chemistry of Solids*, 19(3):218–227, 1961. ISSN 0022-3697. doi: https://doi.org/10.1016/0022-3697(61)90030-0. URL https://www.sciencedirect.com/science/article/pii/0022369761900300.

[29] R. Brunetti, C. Jacoboni, F. Nava, L. Reggiani, G. Bosman, and R. J. J. Zijlstra. Diffusion coefficient of electrons in silicon. *Journal of Applied Physics*, 52(11):6713–6722, 1981. doi: 10.1063/1.328622. URL https://doi.org/10.1063/1.328622.

[30] C. Canali, A. Loria, F. Nava, and G. Ottaviani. Negative differential mobility for electrons in silicon at temperatures below 77°k. *Solid State Communications*, 12(10):1017–1021, 1973. ISSN 0038-1098. doi: https://doi.org/10.1016/0038-1098(73)90027-6. URL https://www.sciencedirect.com/science/article/pii/0038109873900276.

[31] C. Canali, C. Jacoboni, F. Nava, G. Ottaviani, and A. Alberigi-Quaranta. Electron drift velocity in silicon. *Phys. Rev. B*, 12:2265–2284, Sep 1975. doi: 10.1103/PhysRevB.12.2265. URL https://link.aps.org/doi/10.1103/PhysRevB.12.2265.

[32] C. Canali, C. Jacoboni, G. Ottaviani, and A. Alberigi-Quaranta. High-field diffusion of electrons in silicon. *Applied Physics Letters*, 27(5):278–280, 1975. doi: 10.1063/1.88465. URL https://doi.org/10.1063/1.88465.

[33] C. Canali, C. Jacoboni, G. Ottaviani, and A. Alberigi-Quaranta. High-field diffusion of electrons in silicon. *Applied Physics Letters*, 27(5):278–280, 1975. doi: 10.1063/1.88465. URL https://doi.org/10.1063/1.88465.

[34] C. Canali, G. Gavioli, A. Losi, and G. Ottaviani. Hot-hole diffusivity in ge at 77 k. *Solid State Communications*, 20(1):57–60, 1976. ISSN 0038-1098. doi: https://doi.org/10.1016/0038-1098(76)91698-7. URL https://www.sciencedirect.com/science/article/pii/0038109876916987.

[35] David S. Catherall and Austin J. Minnich. High-field charge transport and noise in *p*-si from first principles. *Phys. Rev. B*, 107:035201, Jan 2023. doi: 10.1103/PhysRevB.107.035201. URL https://link.aps.org/doi/10.1103/PhysRevB.107.035201.

[36] Carlton M. Caves. Quantum limits on noise in linear amplifiers. *Phys. Rev. D*, 26:1817–1839, Oct 1982. doi: 10.1103/PhysRevD.26.1817. URL https://link.aps.org/doi/10.1103/PhysRevD.26.1817.

[37] Gang Chen. *Nanoscale energy transport and conversion: a parallel treatment of electrons, molecules, phonons, and photons*. Oxford, New York: Oxford University Press, 2005., 2005.

[38] Jiewei Chen, Yue Zhou, Jianmin Yan, Jidong Liu, Lin Xu, Jingli Wang, Tianqing Wan, Yuhui He, Wenjing Zhang, and Yang Chai. Room-temperature valley transistors for low-power neuromorphic computing. *Nature Communications*, 13(1):7758, 2022. doi: 10.1038/s41467-022-35396-x. URL https://doi.org/10.1038/s41467-022-35396-x.

[39] Ke Chen, Bai Song, Navaneetha K. Ravichandran, Qiye Zheng, Xi Chen, Hwijong Lee, Haoran Sun, Sheng Li, Geethal Amila Gamage Udalamatta Gamage, Fei Tian, Zhiwei Ding, Qichen Song, Akash Rai, Hanlin Wu, Pawan Koirala, Aaron J. Schmidt, Kenji Watanabe, Bing Lv, Zhifeng Ren, Li Shi, David G. Cahill, Takashi Taniguchi, David Broido, and Gang Chen. Ultrahigh thermal conductivity in isotope-enriched cubic boron nitride. *Science*, 367 (6477):555–559, 2020. doi: 10.1126/science.aaz6149. URL https://www.science.org/doi/abs/10.1126/science.aaz6149.

[40] Peishi S. Cheng, Jiace Sun, Shi-Ning Sun, Alexander Y. Choi, and Austin J. Minnich. High-field transport and hot-electron noise in gaas from first-principles calculations: Role of two-phonon scattering. *Phys. Rev. B*, 106: 245201, Dec 2022. doi: 10.1103/PhysRevB.106.245201. URL https://link.aps.org/doi/10.1103/PhysRevB.106.245201.

[41] John Chilleri, Poppy Siddiqua, Michael S. Shur, and Stephen K. O'Leary. Cubic boron nitride as a material for future electron device applications: A comparative analysis. *Applied Physics Letters*, 120(12):122105, 03 2022. ISSN 0003-6951. doi: 10.1063/5.0084360. URL https://doi.org/10.1063/5.0084360.

[42] John Chilleri, Yana Wang, Michael S. Shur, and Stephen K. O'Leary. A low-field electron mobility analysis of cubic boron nitride. *Solid State Communications*, 352:114776, 2022. ISSN 0038-1098. doi: https://doi.org/10.1016/j.ssc.2022.114776. URL https://www.sciencedirect.com/science/article/pii/S0038109822001156.

[43] Alexander Y. Choi, Peishi S. Cheng, Benjamin Hatanpää, and Austin J. Minnich. Electronic noise of warm electrons in semiconductors from first principles. *Phys. Rev. Materials*, 5:044603, Apr 2021. doi: 10.1103/PhysRevMaterials.5.044603. URL https://link.aps.org/doi/10.1103/PhysRevMaterials.5.044603.

[44] R.M. Chrenko. Ultraviolet and infrared spectra of cubic boron nitride. *Solid State Communications*, 14(6):511–515, 1974. ISSN 0038-1098. doi: https://doi.org/10.1016/0038-1098(74)90978-8. URL https://www.sciencedirect.com/science/article/pii/0038109874909788.

[45] Esther Conwell. *High Field Transport in Semiconductors*. Academic Press, 1967. https://www.google.com/books/edition/{High_Field_Transport_in_Semiconductors}/{9teaxQEACAAJ}?hl=en.

[46] M Costato and Lino Reggiani. Electron drift velocity and related phenomena in si. *physica status solidi (b)*, 42(2):591–602, 1970.

[47] M. Costato, S. Fontanesi, and L. Reggiani. Electron energy relaxation time in si and ge. *Journal of Physics and Chemistry of Solids*, 34(3):547–564, 1973. ISSN 0022-3697. doi: https://doi.org/10.1016/0022-3697(73)90050-4. URL https://www.sciencedirect.com/science/article/pii/0022369773900504.

[48] Supriyo Datta and Biswajit Das. Electronic analog of the electro-optic modulator. *Applied Physics Letters*, 56(7):665–667, 02 1990. ISSN 0003-6951. doi: 10.1063/1.102730. URL https://doi.org/10.1063/1.102730.

[49] Dhruv C. Desai, Bahdan Zviazhynski, Jin-Jian Zhou, and Marco Bernardi. Magnetotransport in semiconductors and two-dimensional materials from first principles. *Phys. Rev. B*, 103:L161103, Apr 2021. doi: 10.1103/PhysRevB.103.L161103. URL https://link.aps.org/doi/10.1103/PhysRevB.103.L161103.

[50] W. P. Dumke. Two-phonon indirect transitions and lattice scattering in si. *Phys. Rev.*, 118:938–939, May 1960. doi: 10.1103/PhysRev.118.938. URL https://link.aps.org/doi/10.1103/PhysRev.118.938.

[51] William P. Dumke. Deformation potential theory for *n*-type ge. *Phys. Rev.*, 101:531–536, Jan 1956. doi: 10.1103/PhysRev.101.531. URL https://link.aps.org/doi/10.1103/PhysRev.101.531.

[52] Iretomiwa Esho and Austin J. Minnich. Charge transport in bas and the role of two-phonon scattering. *Phys. Rev. B*, 108:165202, Oct 2023. doi: 10.1103/PhysRevB.108.165202. URL https://link.aps.org/doi/10.1103/PhysRevB.108.165202.

[53] R. Fauquembergue, J. Zimmermann, A. Kaszynski, E. Constant, and Greco Microondes. Diffusion and the power spectral density and correlation function of velocity fluctuation for electrons in Si and GaAs by Monte Carlo methods. *Journal of Applied Physics*, 51(2):1065–1071, 02 1980. ISSN 0021-8979. doi: 10.1063/1.327713. URL https://doi.org/10.1063/1.327713.

[54] W. Fawcett and H.D. Rees. Calculation of the hot electron diffusion rate for gaas. *Physics Letters A*, 29(10):578–579, 1969. ISSN 0375-9601. doi: https://doi.org/10.1016/0375-9601(69)91103-7. URL https://www.sciencedirect.com/science/article/pii/0375960169911037.

[55] W. Fawcett, C. Hilsum, and H.D. Rees. Effects of non-parabolicity on non-ohmic transport in inas. *Solid State Communications*, 7(17):1257–1259, 1969. ISSN 0038-1098. doi: https://doi.org/10.1016/0038-1098(69)90189-6. URL https://www.sciencedirect.com/science/article/pii/0038109869901896.

[56] W. Fawcett, A.D. Boardman, and S. Swain. Monte carlo determination of electron transport properties in gallium arsenide. *Journal of Physics and Chemistry of Solids*, 31(9):1963–1990, 1970. ISSN 0022-3697. doi: https://doi.org/10.1016/0022-3697(70)90001-6. URL https://www.sciencedirect.com/science/article/pii/0022369770900016.

[57] Mattia Fiorentini and Nicola Bonini. Thermoelectric coefficients of *n*-doped silicon from first principles via the solution of the boltzmann transport equation. *Phys. Rev. B*, 94:085204, Aug 2016. doi: 10.1103/PhysRevB.94.085204. URL https://link.aps.org/doi/10.1103/PhysRevB.94.085204.

[58] Björn Fischer and Karl R. Hofmann. A full-band Monte Carlo model for the temperature dependence of electron and hole transport in silicon. *Applied Physics Letters*, 76(5):583–585, 01 2000. ISSN 0003-6951. doi: 10.1063/1.125824. URL https://doi.org/10.1063/1.125824.

[59] M. V. Fischetti, P. D. Yoder, M. M. Khatami, G. Gaddemane, and M. L. Van de Put. "Hot electrons in Si lose energy mostly to optical phonons": Truth or myth? *Applied Physics Letters*, 114(22), 06 2019. ISSN 0003-6951. doi: 10.1063/1.5099914. URL https://doi.org/10.1063/1.5099914. 222104.

[60] M.V. Fischetti. Monte carlo simulation of transport in technologically significant semiconductors of the diamond and zinc-blende structures. i. homogeneous transport. *IEEE Transactions on Electron Devices*, 38(3):634–649, 1991. doi: 10.1109/16.75176.

[61] N. O. Folland. Shapes of two-phonon recombination peaks in silicon. *Phys. Rev. B*, 1:1648–1654, Feb 1970. doi: 10.1103/PhysRevB.1.1648. URL https://link.aps.org/doi/10.1103/PhysRevB.1.1648.

[62] R.H. Fowler. *Statistical Mechanics*. Cambridge University Press, London, 1936.

[63] Valérie Frayssé, Luc Giraud, Serge Gratton, and Julien Langou. Algorithm 842: A set of gmres routines for real and complex arithmetics on high performance computers. *ACM Trans. Math. Softw.*, 31(2):228–238, jun 2005. ISSN 0098-3500. doi: 10.1145/1067967.1067970. URL https://doi.org/10.1145/1067967.1067970.

[64] J. Frey. Effects of intervalley scattering on noise in gaas and inp field-effect transistors. *IEEE Transactions on Electron Devices*, 23(12):1298–1303, 1976. doi: 10.1109/T-ED.1976.18653.

[65] Alex M. Ganose, Junsoo Park, Alireza Faghaninia, Rachel Woods-Robinson, Kristin A. Persson, and Anubhav Jain. Efficient calculation of carrier scattering rates from first principles. *Nature Communications*, 12(1):2222, 2021. doi: 10.1038/s41467-021-22440-5. URL https://doi.org/10.1038/s41467-021-22440-5.

[66] SV Gantsevich, VL Gurevich, and R Katilius. Fluctuations in semiconductors in a strong electric field and the scattering of light by" hot" electrons. *Soviet Physics JETP*, 22(4), 1970.

[67] S.V. Gantsevich, V.L. Gurevich, and R. Katilius. Theory of fluctuations in nonequilibrium electron gas. *Rivista Del Nuovo Cimento*, 2(5), 1979.

[68] Shiyuan Gao, Jin-Jian Zhou, Yao Luo, and Marco Bernardi. First-principles electron-phonon interactions and electronic transport in large-angle twisted bilayer graphene. *Phys. Rev. Mater.*, 8:L051001, May 2024. doi: 10.1103/PhysRevMaterials.8.L051001. URL https://link.aps.org/doi/10.1103/PhysRevMaterials.8.L051001.

[69] F Pelayo García de Arquer, Ardalan Armin, Paul Meredith, and Edward H Sargent. Solution-processed semiconductors for next-generation photodetectors. *Nature Reviews Materials*, 2(3):1–17, 2017.

[70] D. Gasquet, M. de Murcia, J.P. Nougier, and C. Gontrand. Transport parameters of hot electrons in gaas at 300 k. *Physica B+C*, 134(1):264–268, 1985. ISSN 0378-4363. doi: https://doi.org/10.1016/0378-4363(85)90353-5. URL https://www.sciencedirect.com/science/article/pii/0378436385903535.

[71] E. Gheeraert, N. Casanova, A. Tajani, A. Deneuville, E. Bustarret, J.A. Garrido, C.E. Nebel, and M. Stutzmann. n-type doping of diamond by sulfur and phosphorus. *Diamond and Related Materials*, 11(3):289–295, 2002. ISSN 0925-9635. doi: https://doi.org/10.1016/S0925-9635(01)00683-5. URL https://www.sciencedirect.com/science/article/pii/S0925963501006835. 12th European Conference on Diamond, Diamond-Like Materials, Carbon Nanotubes, Nitrides & Silicon Carbide.

[72] Paolo Giannozzi, Stefano Baroni, Nicola Bonini, Matteo Calandra, Roberto Car, Carlo Cavazzoni, Davide Ceresoli, Guido L. Chiarotti, Matteo Cococcioni, Ismaila Dabo, Andrea Dal Corso, Stefano De Gironcoli, Stefano Fabris, Guido Fratesi, Ralph Gebauer, Uwe Gerstmann, Christos Gougoussis, Anton Kokalj, Michele Lazzeri, Layla Martin-Samos, Nicola Marzari, Francesco Mauri, Riccardo Mazzarello, Stefano Paolini, Alfredo Pasquarello, Lorenzo Paulatto, Carlo Sbraccia, Sandro Scandolo, Gabriele Sclauzero, Ari P. Seitsonen, Alexander Smogunov, Paolo Umari, and Renata M. Wentzcovitch. Quantum espresso: A modular and open-source software project for quantum simulations of materials. *Journal of physics. Condensed matter : an Institute of Physics journal*, 21(39), 2009. ISSN 0953-8984. doi: 10.1088/0953-8984/21/39/395502.

[73] W.E.K. Gibbs. Conductivity anisotropy and hot electron temperature in silicon. *Journal of Physics and Chemistry of Solids*, 25(2):247–251, 1964. ISSN 0022-3697. doi: https://doi.org/10.1016/0022-3697(64)90085-

X. URL https://www.sciencedirect.com/science/article/pii/002236976490085X.

[74] Feliciano Giustino. Electron-phonon interactions from first principles. *Rev. Mod. Phys.*, 89:015003, Feb 2017. doi: 10.1103/RevModPhys.89.015003. URL https://link.aps.org/doi/10.1103/RevModPhys.89.015003.

[75] Martin A. Green, Anita Ho-Baillie, and Henry J. Snaith. The emergence of perovskite solar cells. *Nature Photonics*, 8(7):506–514, 2014. doi: 10.1038/nphoton.2014.134. URL https://doi.org/10.1038/nphoton.2014.134.

[76] J.B. Gunn. Microwave oscillations of current in iii–v semiconductors. *Solid State Communications*, 1(4):88–91, 1963. ISSN 0038-1098. doi: https://doi.org/10.1016/0038-1098(63)90041-3. URL https://www.sciencedirect.com/science/article/pii/0038109863900413.

[77] C. Hamaguchi and N. Mori. Magnetophonon resonance in semiconductors. *Physica B: Condensed Matter*, 164(1):85–96, 1990. ISSN 0921-4526. doi: https://doi.org/10.1016/0921-4526(90)90065-3. URL https://www.sciencedirect.com/science/article/pii/0921452690900653.

[78] Chihiro Hamaguchi and Yoshio Inuishi. Temperature dependence of mobility of warm carriers in germanium and silicon. *Journal of the Physical Society of Japan*, 18(12):1755–1762, 1963. doi: 10.1143/JPSJ.18.1755. URL https://doi.org/10.1143/JPSJ.18.1755.

[79] Chihiro Hamaguchi and Yoshio Inuishi. Conductivity anisotropy of hot electrons in n-type silicon heated by microwave fields. *Journal of Physics and Chemistry of Solids*, 27:1511–1518, 1966.

[80] K.V. Hansen. *Some investigations of the intervalley scattering in N-type silicon*. Phd thesis, Technical University of Denmark, 1974.

[81] Ariful Haque and Jagdish Narayan. Tunable n-type conductivity and transport properties of cubic boron nitride via carbon doping. *ACS Applied Electronic Materials*, 3(3):1359–1367, 03 2021. doi: 10.1021/acsaelm.0c01130. URL https://doi.org/10.1021/acsaelm.0c01130.

[82] Ariful Haque, Saif Taqy, and Jagdish Narayan. Recent progress in cubic boron nitride (c-bn) fabrication by pulsed laser annealing for optoelectronic applications. *Journal of Electronic Materials*, 53(8):4308–4340, 2024. doi: 10.1007/s11664-024-11171-0. URL https://doi.org/10.1007/s11664-024-11171-0.

[83] T.K. Harris, E.J. Brookes, and C.J. Taylor. The effect of temperature on the hardness of polycrystalline cubic boron nitride cutting tool materials.

International Journal of Refractory Metals and Hard Materials, 22(2):105–110, 2004. ISSN 0263-4368. doi: https://doi.org/10.1016/j.ijrmhm.2004.01.004. URL https://www.sciencedirect.com/science/article/pii/S0263436804000058.

[84] H.L. Hartnagel, R. Katilius, and A. Matulionis. *Microwave Noise in Semiconductor Devices*. John Wiley & Sons, New York, 2001.

[85] Benjamin Hatanpää and Austin J. Minnich. Hot electron diffusion, microwave noise, and piezoresistivity in si from first principles. *Phys. Rev. B*, 109: 235201, Jun 2024. doi: 10.1103/PhysRevB.109.235201. URL https://link.aps.org/doi/10.1103/PhysRevB.109.235201.

[86] Benjamin Hatanpää, Alexander Y. Choi, Peishi S. Cheng, and Austin J. Minnich. Two-phonon scattering in nonpolar semiconductors: A first-principles study of warm electron transport in si. *Phys. Rev. B*, 107: L041110, Jan 2023. doi: 10.1103/PhysRevB.107.L041110. URL https://link.aps.org/doi/10.1103/PhysRevB.107.L041110.

[87] E.A. Hendriks and R.J.J. Zijlstra. Diffusion and inter-valley noise in (100) n-channel si-mosfets from t = 4.2 to 295 k. *Solid-State Electronics*, 31 (2):171–180, 1988. ISSN 0038-1101. doi: https://doi.org/10.1016/0038-1101(88)90126-8. URL https://www.sciencedirect.com/science/article/pii/0038110188901268.

[88] G. Hill, P. N. Robson, and W. Fawcett. Diffusion and the power spectral density of velocity fluctuations for electrons in InP by Monte Carlo methods. *Journal of Applied Physics*, 50(1):356–360, 01 1979. ISSN 0021-8979. doi: 10.1063/1.325670. URL https://doi.org/10.1063/1.325670.

[89] C. Hilsum. Transferred electron amplifiers and oscillators. *Proceedings of the IRE*, 50(2):185–189, 1962. doi: 10.1109/JRPROC.1962.288025.

[90] Kazuyuki Hirama, Yoshitaka Taniyasu, Hideki Yamamoto, and Kazuhide Kumakura. Control of n-type electrical conductivity for cubic boron nitride (c-BN) epitaxial layers by Si doping. *Applied Physics Letters*, 116(16): 162104, 04 2020. ISSN 0003-6951. doi: 10.1063/1.5143791. URL https://doi.org/10.1063/1.5143791.

[91] Lillian H. Hoddeson, G. Baym, and Nevill Francis Mott. The development of the quantum mechanical electron theory of metals: 1900-28. *Proceedings of the Royal Society of London. A. Mathematical and Physical Sciences*, 371(1744):8–23, 1980. doi: 10.1098/rspa.1980.0051. URL https://royalsocietypublishing.org/doi/abs/10.1098/rspa.1980.0051.

[92] P. Hohenberg and W. Kohn. Inhomogeneous electron gas. *Phys. Rev.*, 136: B864–B871, Nov 1964. doi: 10.1103/PhysRev.136.B864. URL https://link.aps.org/doi/10.1103/PhysRev.136.B864.

[93] T. Holstein. Theory of ultrasonic absorption in metals: the collision-drag effect. *Phys. Rev.*, 113:479–496, Jan 1959. doi: 10.1103/PhysRev.113.479. URL https://link.aps.org/doi/10.1103/PhysRev.113.479.

[94] F.N. Hooge. 1/f noise sources. *IEEE Transactions on Electron Devices*, 41 (11):1926–1935, 1994. doi: 10.1109/16.333808.

[95] Safdar Iqbal, Tao Cheng, Xinlei Duan, Linhua Liu, and Jia-Yue Yang. Phonon-assisted carrier transport and indirect optical absorption of cubic boron nitride from first-principles. *Journal of Applied Physics*, 135 (5):055102, 02 2024. ISSN 0021-8979. doi: 10.1063/5.0180628. URL https://doi.org/10.1063/5.0180628.

[96] J. Isberg, M. Gabrysch, S. Majdi, and D. J. Twitchen. Negative electron mobility in diamond. *Applied Physics Letters*, 100(17):172103, 04 2012. ISSN 0003-6951. doi: 10.1063/1.4705434. URL https://doi.org/10.1063/1.4705434.

[97] Jan Isberg, Markus Gabrysch, Johan Hammersberg, Saman Majdi, Kiran Kumar Kovi, and Daniel J. Twitchen. Generation, transport and detection of valley-polarized electrons in diamond. *Nature Materials*, 12(8):760–764, 2013. doi: 10.1038/nmat3694. URL https://doi.org/10.1038/nmat3694.

[98] Natalia Izyumskaya, Denis O. Demchenko, Saikat Das, Ümit Özgür, Vitaliy Avrutin, and Hadis Morkoç. Recent development of boron nitride towards electronic applications. *Advanced Electronic Materials*, 3(5): 1600485, 2017. doi: https://doi.org/10.1002/aelm.201600485. URL https://onlinelibrary.wiley.com/doi/abs/10.1002/aelm.201600485.

[99] C. Jacoboni, R. Minder, and G. Majni. Effects of band non-parabolicity on electron drift velocity in silicon above room temperature. *Journal of Physics and Chemistry of Solids*, 36(10):1129–1133, 1975. ISSN 0022-3697. doi: https://doi.org/10.1016/0022-3697(75)90055-4. URL https://www.sciencedirect.com/science/article/pii/0022369775900554.

[100] Carlo Jacoboni. *Theory of electron transport in semiconductors. A pathway from elementary physics to nonequilibrium Green functions*. Springer Berlin, Heidelberg, Jul 2010. doi: 10.1007/978-3-642-10586-9.

[101] Carlo Jacoboni and Lino Reggiani. The monte carlo method for the solution of charge transport in semiconductors with applications to covalent materials. *Rev. Mod. Phys.*, 55:645–705, Jul 1983. doi: 10.1103/RevModPhys.55.645. URL https://link.aps.org/doi/10.1103/RevModPhys.55.645.

[102] J. F. Janak, V. L. Moruzzi, and A. R. Williams. Ground-state thermomechanical properties of some cubic elements in the local-density formalism. *Phys. Rev. B*, 12:1257–1261, Aug 1975. doi: 10.1103/PhysRevB.12.1257. URL https://link.aps.org/doi/10.1103/PhysRevB.12.1257.

[103] Mark Johnson and R. H. Silsbee. Interfacial charge-spin coupling: Injection and detection of spin magnetization in metals. *Phys. Rev. Lett.*, 55:1790–1793, Oct 1985. doi: 10.1103/PhysRevLett.55.1790. URL https://link.aps.org/doi/10.1103/PhysRevLett.55.1790.

[104] M. H. Jørgensen. Warm-electron effects in *n*-type silicon and germanium. *Phys. Rev.*, 156:834–843, Apr 1967. doi: 10.1103/PhysRev.156.834. URL https://link.aps.org/doi/10.1103/PhysRev.156.834.

[105] M. H. Jørgensen. Electron-phonon scattering and high-field transport in *n*-type si. *Phys. Rev. B*, 18:5657–5666, Nov 1978. doi: 10.1103/PhysRevB.18.5657. URL https://link.aps.org/doi/10.1103/PhysRevB.18.5657.

[106] M.H. Jørgensen, N.I. Meyer, and K.J. Schmidt-Tiedemann. Conductivity anisotropy of warm and hot electrons in silicon and germanium. *Solid State Communications*, 1(7):226–233, 1963. ISSN 0038-1098. doi: https://doi.org/10.1016/0038-1098(63)90014-0. URL https://www.sciencedirect.com/science/article/pii/0038109863900140.

[107] M.H. Jørgensen, N.O. Gram, and N.I. Meyer. Negative differential conductivity and current oscillations in lightly doped n-type silicon. *Solid State Communications*, 10(4):337–340, 1972. ISSN 0038-1098. doi: https://doi.org/10.1016/0038-1098(72)90437-1. URL https://www.sciencedirect.com/science/article/pii/0038109872904371.

[108] Peter Kästner, Ernst-Peter Röth, and Karlheinz Seeger. Conductivity anisotropy of n-type silicon in the range of warm and hot carriers. *Zeitschrift für Physik*, 187(4):359–368, 1965. doi: 10.1007/BF01328720. URL https://doi.org/10.1007/BF01328720.

[109] Elise Knittle, Renata M. Wentzcovitch, Raymond Jeanloz, and Marvin L. Cohen. Experimental and theoretical equation of state of cubic boron nitride. *Nature*, 337(6205):349–352, 1989. doi: 10.1038/337349a0. URL https://doi.org/10.1038/337349a0.

[110] P. Kocevar. *Multiphonon Scattering*, pages 167–174. Springer, Boston, MA, 01 1980. ISBN 978-1-4684-3640-2. doi: 10.1007/978-1-4684-3638-9_7.

[111] Sh. Kogan. *Electronic Noise and Fluctuations in Solids*. Cambridge University Press, 1996.

[112] W. Kohn and L. J. Sham. Self-consistent equations including exchange and correlation effects. *Phys. Rev.*, 140:A1133–A1138, Nov 1965. doi: 10.1103/PhysRev.140.A1133. URL https://link.aps.org/doi/10.1103/PhysRev.140.A1133.

[113] Satoshi Koizumi. Heteroepitaxy of diamond on cubic boron nitride. *Israel Journal of Chemistry*, 38(1-2):33–40, 1998. doi: https://doi.org/10.1002/ijch.199800004. URL https://onlinelibrary.wiley.com/doi/abs/10.1002/ijch.199800004.

[114] H. Kroemer. Theory of the gunn effect. *Proceedings of the IEEE*, 52(12): 1736–1736, 1964. doi: 10.1109/PROC.1964.3476.

[115] Shrishail S Kubakaddi and B. S. Krishnamurthy. The electron-two short-wavelength phonon scattering in non-polar semiconductors. *Physica Status Solidi B-basic Solid State Physics*, 80:603–609, 1977.

[116] SS Kubakaddi and BS Krishnamurthy. Infrared free-carrier absorption in non-polar semiconductors; scattering by two short wavelength phonons. *Indian Journal of Physics A*, 53(1):127–135, 1979.

[117] Tilmann Kuhn, Lino Reggiani, Luca Varani, and Vladimir Mitin. Monte carlo method for the simulation of electronic noise in semiconductors. *Phys. Rev. B*, 42:5702–5713, Sep 1990. doi: 10.1103/PhysRevB.42.5702. URL https://link.aps.org/doi/10.1103/PhysRevB.42.5702.

[118] Tatsumi Kurosawa. Monte carlo calculation of hot electron problems. In *Proc. Intl. Conf. on Physics of Semiconductors*, pages 424–426, 1966.

[119] Tatsumi Kurosawa and Hajime Maeda. Monte carlo calculation of hot electron phenomena. i. streaming in the absence of a magnetic field. *Journal of the Physical Society of Japan*, 31(3):668–678, 1971. doi: 10.1143/JPSJ.31.668. URL https://doi.org/10.1143/JPSJ.31.668.

[120] Melvin Lax. Fluctuations from the nonequilibrium steady state. *Rev. Mod. Phys.*, 32:25–64, Jan 1960. doi: 10.1103/RevModPhys.32.25. URL https://link.aps.org/doi/10.1103/RevModPhys.32.25.

[121] Paul A. Lebwohl. Monte Carlo simulation of response of a semiconductor to periodic perturbations. *Journal of Applied Physics*, 44(4):1744–1752, 04 1973. ISSN 0021-8979. doi: 10.1063/1.1662441. URL https://doi.org/10.1063/1.1662441.

[122] Nien-En Lee, Jin-Jian Zhou, Luis A. Agapito, and Marco Bernardi. Charge transport in organic molecular semiconductors from first principles: The bandlike hole mobility in a naphthalene crystal. *Phys. Rev. B*, 97:115203, Mar 2018. doi: 10.1103/PhysRevB.97.115203. URL https://link.aps.org/doi/10.1103/PhysRevB.97.115203.

[123] Nien-En Lee, Jin-Jian Zhou, Hsiao-Yi Chen, and Marco Bernardi. Ab initio electron-two-phonon scattering in gaas from next-to-leading order perturbation theory. *Nature Communications*, 11(1):1607, 2020. doi: 10.1038/s41467-020-15339-0. URL https://doi.org/10.1038/s41467-020-15339-0.

[124] Wonho Lee, Yun Hwangbo, Jae-Hyun Kim, and Jong-Hyun Ahn. Mobility enhancement of strained si transistors by transfer printing on plastic substrates. *NPG Asia Materials*, 8(3):e256–e256, 2016. doi: 10.1038/am.2016.31. URL https://doi.org/10.1038/am.2016.31.

[125] Joshua Leveillee, Xiao Zhang, Emmanouil Kioupakis, and Feliciano Giustino. Ab initio calculation of carrier mobility in semiconductors including ionized-impurity scattering. *Phys. Rev. B*, 107:125207, Mar 2023. doi: 10.1103/PhysRevB.107.125207. URL https://link.aps.org/doi/10.1103/PhysRevB.107.125207.

[126] Wu Li. Electrical transport limited by electron-phonon coupling from boltzmann transport equation: An ab initio study of si, al, and mos_2. *Phys. Rev. B*, 92:075405, Aug 2015. doi: 10.1103/PhysRevB.92.075405. URL https://link.aps.org/doi/10.1103/PhysRevB.92.075405.

[127] K. J. LIAO, W. L. WANG, C. Z. CAI, X. S. WANG, and C. Y. KONG. Uv photodetectors of c-bn films. *International Journal of Modern Physics B*, 16(06n07):1115–1119, 2002. doi: 10.1142/S0217979202010968. URL https://doi.org/10.1142/S0217979202010968.

[128] Dmitri Litvinov, Charles A. Taylor, and Roy Clarke. Semiconducting cubic boron nitride. *Diamond and Related Materials*, 7(2):360–364, 1998. ISSN 0925-9635. doi: https://doi.org/10.1016/S0925-9635(97)00216-1. URL https://www.sciencedirect.com/science/article/pii/S0925963597002161.

[129] Te-Huan Liu, Jiawei Zhou, Bolin Liao, David J. Singh, and Gang Chen. First-principles mode-by-mode analysis for electron-phonon scattering channels and mean free path spectra in gaas. *Phys. Rev. B*, 95:075206, Feb 2017. doi: 10.1103/PhysRevB.95.075206. URL https://link.aps.org/doi/10.1103/PhysRevB.95.075206.

[130] R. A. Logan and A. J. Peters. Impurity effects upon mobility in silicon. *Journal of Applied Physics*, 31(1):122–124, 1960. doi: 10.1063/1.1735385. URL https://doi.org/10.1063/1.1735385.

[131] Donald Long and John Myers. Ionized-impurity scattering mobility of electrons in silicon. *Phys. Rev.*, 115:1107–1118, Sep 1959. doi: 10.1103/PhysRev.115.1107. URL https://link.aps.org/doi/10.1103/PhysRev.115.1107.

[132] I-Te Lu, Jin-Jian Zhou, and Marco Bernardi. Efficient ab initio calculations of electron-defect scattering and defect-limited carrier mobility. *Phys. Rev. Mater.*, 3:033804, Mar 2019. doi: 10.1103/PhysRevMaterials.3.033804. URL https://link.aps.org/doi/10.1103/PhysRevMaterials.3.033804.

[133] I-Te Lu, Jin-Jian Zhou, Jinsoo Park, and Marco Bernardi. First-principles ionized-impurity scattering and charge transport in doped materials. *Phys. Rev. Mater.*, 6:L010801, Jan 2022. doi: 10.1103/PhysRevMaterials.6.L010801. URL https://link.aps.org/doi/10.1103/PhysRevMaterials.6.L010801.

[134] G. W. Ludwig and R. L. Watters. Drift and conductivity mobility in silicon. *Phys. Rev.*, 101:1699–1701, Mar 1956. doi: 10.1103/PhysRev.101.1699. URL https://link.aps.org/doi/10.1103/PhysRev.101.1699.

[135] Jinlong Ma, Arun S. Nissimagoudar, and Wu Li. First-principles study of electron and hole mobilities of si and gaas. *Phys. Rev. B*, 97:045201, Jan 2018. doi: 10.1103/PhysRevB.97.045201. URL https://link.aps.org/doi/10.1103/PhysRevB.97.045201.

[136] Gerald D Mahan. *Many-particle physics*. Springer Science & Business Media, 2013.

[137] Ivan Maliyov, Jinsoo Park, and Marco Bernardi. Ab initio electron dynamics in high electric fields: Accurate prediction of velocity-field curves. *Phys. Rev. B*, 104:L100303, Sep 2021. doi: 10.1103/PhysRevB.104.L100303. URL https://link.aps.org/doi/10.1103/PhysRevB.104.L100303.

[138] Richard M Martin. *Electronic structure: basic theory and practical methods*. Cambridge university press, 2020.

[139] Glen D Martinson and Mark M Burin. Radar detector technology. *Applied Microwave*, 2:68–85, 1990.

[140] Nicola Marzari, Arash A. Mostofi, Jonathan R. Yates, Ivo Souza, and David Vanderbilt. Maximally localized wannier functions: Theory and applications. *Rev. Mod. Phys.*, 84:1419–1475, Oct 2012. doi: 10.1103/RevModPhys.84.1419. URL https://link.aps.org/doi/10.1103/RevModPhys.84.1419.

[141] E. Massa, G. Mana, U. Kuetgens, and L. Ferroglio. Measurement of the lattice parameter of a silicon crystal. *New Journal of Physics*, 11, 2009. doi: 10.1088/1367-2630/11/5/053013. URL https://doi.org/10.1088/1367-2630/11/5/053013.

[142] Jean Messier and Jorge Merlo Flores. Temperature dependence of hall mobility and μh/μd for si. *Journal of Physics and Chemistry of Solids*, 24(12): 1539–1542, 1963.

[143] Osamu Mishima, Junzo Tanaka, Shinobu Yamaoka, and Osamu Fukunaga. High-temperature cubic boron nitride p-n junction diode made at high pressure. *Science*, 238(4824):181–183, 1987. doi: 10.1126/science.238.4824.181. URL https://www.science.org/doi/abs/10.1126/science.238.4824.181.

[144] Osamu Mishima, Koh Era, Junzo Tanaka, and Shinobu Yamaoka. Ultraviolet light-emitting diode of a cubic boron nitride pn junction made at high pressure. *Applied Physics Letters*, 53(11):962–964, 09 1988. ISSN 0003-6951. doi: 10.1063/1.100082. URL https://doi.org/10.1063/1.100082.

[145] V. L. Moruzzi, A. R. Williams, and J. F. Janak. Local density theory of metallic cohesion. *Phys. Rev. B*, 15:2854–2857, Mar 1977. doi: 10.1103/PhysRevB.15.2854. URL https://link.aps.org/doi/10.1103/PhysRevB.15.2854.

[146] Arash A. Mostofi, Jonathan R. Yates, Young-Su Lee, Ivo Souza, David Vanderbilt, and Nicola Marzari. wannier90: A tool for obtaining maximally-localised wannier functions. *Computer Physics Communications*, 178(9):685 – 699, 2008. ISSN 0010-4655. doi: https://doi.org/10.1016/j.cpc.2007.11.016. http://www.sciencedirect.com/science/article/pii/S0010465507004936.

[147] Saikat Mukhopadhyay and Derek Stewart. Polar effects on the thermal conductivity of cubic boron nitride under pressure. *Physical Review Letters*, 113:025901, 07 2014. doi: 10.1103/PhysRevLett.113.025901.

[148] Jeffrey T. Mullen, James A. Boulton, Minghao Pan, and Ki Wook Kim. Electronic properties of c-bn/diamond heterostructures for high-frequency high-power applications. *Diamond and Related Materials*, 143:110920, 2024. ISSN 0925-9635. doi: https://doi.org/10.1016/j.diamond.2024.110920. URL https://www.sciencedirect.com/science/article/pii/S092596352400133X.

[149] S Nakamura, T Mukai, and M Senoh. In situ monitoring and hall measurements of gan grown with gan buffer layers. *Journal of applied physics*, 71 (11):5543–5549, 1992.

[150] Shuji Nakamura and Gerhard Fasol. *The blue laser diode: GaN based light emitters and lasers*. Springer Science & Business Media, 2013.

[151] Shuji Nakamura, Takashi Mukai, Masayuki Senoh Masayuki Senoh, and Naruhito Iwasa Naruhito Iwasa. Thermal annealing effects on p-type mg-doped gan films. *Japanese Journal of Applied Physics*, 31(2B):L139, 1992.

[152] Shuji Nakamura Shuji Nakamura. Gan growth using gan buffer layer. *Japanese Journal of Applied Physics*, 30(10A):L1705, 1991.

[153] K. L. Ngai. Carrier-two phonon interaction in semiconductors. In Manfred H. Pilkuhn, editor, *Proceedings of the Twelfth International Conference on the Physics of Semiconductors*, pages 489–498, Wiesbaden, 1974. Vieweg+Teubner Verlag. ISBN 978-3-322-94774-1.

[154] Phuong Hoa Nguyen, Karl R. Hofmann, and Gernot Paasch. Comparative full-band Monte Carlo study of Si and Ge with screened pseudopotential-based phonon scattering rates. *Journal of Applied Physics*, 94(1):375–386, 06 2003. ISSN 0021-8979. doi: 10.1063/1.1579860. URL https://doi.org/10.1063/1.1579860.

[155] Jesse Noffsinger, Emmanouil Kioupakis, Chris G. Van de Walle, Steven G. Louie, and Marvin L. Cohen. Phonon-assisted optical absorption in silicon from first principles. *Phys. Rev. Lett.*, 108:167402, Apr 2012. doi: 10.1103/PhysRevLett.108.167402. URL https://link.aps.org/doi/10.1103/PhysRevLett.108.167402.

[156] S. Noor Mohammad. Electrical characteristics of thin film cubic boron nitride. *Solid-State Electronics*, 46(2):203–222, 2002. ISSN 0038-1101. doi: https://doi.org/10.1016/S0038-1101(01)00160-5. URL https://www.sciencedirect.com/science/article/pii/S0038110101001605.

[157] P. Norton, T. Braggins, and H. Levinstein. Impurity and lattice scattering parameters as determined from hall and mobility analysis in *n*-type silicon. *Phys. Rev. B*, 8:5632–5653, Dec 1973. doi: 10.1103/PhysRevB.8.5632. URL https://link.aps.org/doi/10.1103/PhysRevB.8.5632.

[158] K. Nose, H.S. Yang, and T. Yoshida. Electrical characterization of p-type cubic boron nitride/n-type silicon heterojunction diodes. *Diamond and Related Materials*, 14(8):1297–1301, 2005. ISSN 0925-9635. doi: https://doi.org/10.1016/j.diamond.2004.11.044. URL https://www.sciencedirect.com/science/article/pii/S0925963505000178. SMAC '04 Conference Proceeding S.I.

[159] M.A. Osman, M. Imam, and N. Nintunze. Diffusion coefficient of electrons in diamond. In Y. Tzeng, M. Yoshikawa, M. Murakawa, and A. Feldman, editors, *Applications of Diamond Films and Related Materials*, volume 73 of *Materials Science Monographs*, pages 611–614. Elsevier, 1991. doi: https://doi.org/10.1016/B978-0-444-89162-4.50099-3. URL https://www.sciencedirect.com/science/article/pii/B9780444891624500993.

[160] Mikael Östling, Reza Ghandi, and Carl-Mikael Zetterling. Sic power devices—present status, applications and future perspective. In *2011 IEEE 23rd International Symposium on Power Semiconductor Devices and ICs*, pages 10–15. IEEE, 2011.

[161] Jinsoo Park, Jin-Jian Zhou, Vatsal A. Jhalani, Cyrus E. Dreyer, and Marco Bernardi. Long-range quadrupole electron-phonon interaction from first principles. *Phys. Rev. B*, 102:125203, Sep 2020. doi: 10.1103/PhysRevB.102.125203. URL https://link.aps.org/doi/10.1103/PhysRevB.102.125203.

[162] Giovanni Pizzi, Valerio Vitale, Ryotaro Arita, Stefan Blügel, Frank Freimuth, Guillaume Géranton, Marco Gibertini, Dominik Gresch, Charles Johnson, Takashi Koretsune, Julen Ibañez-Azpiroz, Hyungjun Lee, Jae-Mo Lihm, Daniel Marchand, Antimo Marrazzo, Yuriy Mokrousov, Jamal I Mustafa, Yoshiro Nohara, Yusuke Nomura, Lorenzo Paulatto, Samuel Poncé, Thomas Ponweiser, Junfeng Qiao, Florian Thöle, Stepan S Tsirkin, Małgorzata Wierzbowska, Nicola Marzari, David Vanderbilt, Ivo Souza, Arash A Mostofi, and Jonathan R Yates. Wannier90 as a community code: new features and applications. *Journal of Physics: Condensed Matter*, 32(16): 165902, jan 2020. doi: 10.1088/1361-648x/ab51ff. https://doi.org/10.1088/1361-648x/ab51ff.

[163] Samuel Poncé, Elena R. Margine, and Feliciano Giustino. Towards predictive many-body calculations of phonon-limited carrier mobilities in semiconductors. *Phys. Rev. B*, 97:121201, Mar 2018. doi: 10.1103/PhysRevB.97.121201. URL https://link.aps.org/doi/10.1103/PhysRevB.97.121201.

[164] Samuel Poncé, Francesco Macheda, Elena Roxana Margine, Nicola Marzari, Nicola Bonini, and Feliciano Giustino. First-principles predictions of hall and drift mobilities in semiconductors. *Phys. Rev. Res.*, 3:043022, Oct 2021. doi: 10.1103/PhysRevResearch.3.043022. URL https://link.aps.org/doi/10.1103/PhysRevResearch.3.043022.

[165] Eric Pop, Robert W. Dutton, and Kenneth E. Goodson. Analytic band Monte Carlo model for electron transport in Si including acoustic and optical phonon dispersion. *Journal of Applied Physics*, 96(9):4998–5005, 10 2004. ISSN 0021-8979. doi: 10.1063/1.1788838. URL https://doi.org/10.1063/1.1788838.

[166] M.W. Pospieszalski. Modeling of noise parameters of mesfets and modfets and their frequency and temperature dependence. *IEEE Transactions on Microwave Theory and Techniques*, 37(9):1340–1350, 1989. doi: 10.1109/22.32217.

[167] P. J. Price. Intervalley noise. *Journal of Applied Physics*, 31(6):949–953, 1960. doi: 10.1063/1.1735782. URL https://doi.org/10.1063/1.1735782.

[168] P. J. Price. Transport properties of the semiconductor superlattice. *IBM Journal of Research and Development*, 17(1):39–46, 1973. doi: 10.1147/rd.171.0039.

[169] Peter J. Price. Chapter 4 monte carlo calculation of electron transport in solids. In R.K. Willardson and Albert C. Beer, editors, *Lasers, Junctions, Transport*, volume 14 of *Semiconductors and Semimetals*, pages 249–308. Elsevier, 1979. doi: https://doi.org/10.1016/S0080-8784(08)60267-7. URL https://www.sciencedirect.com/science/article/pii/S0080878408602677.

[170] P.J. Price. Calculation of hot electron phenomena. *Solid-State Electronics*, 21(1):9–16, 1978. ISSN 0038-1101. doi: https://doi.org/10.1016/0038-1101(78)90109-0. URL https://www.sciencedirect.com/science/article/pii/0038110178901090.

[171] M. B. Prince. Drift mobilities in semiconductors. ii. silicon. *Phys. Rev.*, 93:1204–1206, Mar 1954. doi: 10.1103/PhysRev.93.1204. URL https://link.aps.org/doi/10.1103/PhysRev.93.1204.

[172] A. Alberigi Quaranta, C. Jacoboni, and G. Ottaviani. Negative differential mobility in iii–v and ii–vi semiconducting compounds. *La Rivista Del Nuovo Cimento*, 1(4):445–495, 1971. doi: 10.1007/BF02747246. URL https://doi.org/10.1007/BF02747246.

[173] A. Alberigi Quaranta, V. Borsari, C. Jacoboni, and G. Zanarini. Electron diffusion in CdTe. *Applied Physics Letters*, 22(3):103–105, 02 1973. ISSN 0003-6951. doi: 10.1063/1.1654567. URL https://doi.org/10.1063/1.1654567.

[174] H D Rees. Numerical solution of electron motion in solids. *Journal of Physics C: Solid State Physics*, 5(6):641, mar 1972. doi: 10.1088/0022-3719/5/6/006. URL https://dx.doi.org/10.1088/0022-3719/5/6/006.

[175] H.D. Rees. Calculation of distribution functions by exploiting the stability of the steady state. *Journal of Physics and Chemistry of Solids*, 30(3):643–655, 1969. ISSN 0022-3697. doi: https://doi.org/10.1016/0022-3697(69)90018-3. URL https://www.sciencedirect.com/science/article/pii/0022369769900183.

[176] H.D. Rees. Hot electron effects at microwave frequencies in gaas. *Solid State Communications*, 7(2):267–269, 1969. ISSN 0038-1098. doi: https://doi.org/10.1016/0038-1098(69)90396-2. URL https://www.sciencedirect.com/science/article/pii/0038109869903962.

[177] J. B. Renucci, R. N. Tyte, and M. Cardona. Resonant raman scattering in silicon. *Phys. Rev. B*, 11:3885–3895, May 1975. doi: 10.1103/PhysRevB.11.3885. URL https://link.aps.org/doi/10.1103/PhysRevB.11.3885.

[178] B K Ridley. Specific negative resistance in solids. *Proceedings of the Physical Society*, 82(6):954, dec 1963. doi: 10.1088/0370-1328/82/6/315. URL https://dx.doi.org/10.1088/0370-1328/82/6/315.

[179] B K Ridley. Propagation of space-charge waves in a conductor exhibiting a differential negative resistance. *Proceedings of the Physical Society*, 86(3):637, sep 1965. doi: 10.1088/0370-1328/86/3/323. URL https://dx.doi.org/10.1088/0370-1328/86/3/323.

[180] B K Ridley and T B Watkins. The possibility of negative resistance effects in semiconductors. *Proceedings of the Physical Society*, 78(2):293, aug 1961. doi: 10.1088/0370-1328/78/2/315. URL https://dx.doi.org/10.1088/0370-1328/78/2/315.

[181] J. G. Ruch and G. S. Kino. Transport Properties of GaAs. *Phys. Rev.*, 174:921–931, Oct 1968. doi: 10.1103/PhysRev.174.921. URL https://link.aps.org/doi/10.1103/PhysRev.174.921.

[182] David W Runton, Brian Trabert, Jeffrey B Shealy, and Ramakrishna Vetury. History of gan: High-power rf gallium nitride (gan) from infancy to manufacturable process and beyond. *IEEE Microwave Magazine*, 14(3):82–93, 2013.

[183] E. J. Ryder. Mobility of holes and electrons in high electric fields. *Phys. Rev.*, 90:766–769, Jun 1953. doi: 10.1103/PhysRev.90.766. URL https://link.aps.org/doi/10.1103/PhysRev.90.766.

[184] E. J. Ryder and W. Shockley. Mobilities of electrons in high electric fields. *Phys. Rev.*, 81:139–140, Jan 1951. doi: 10.1103/PhysRev.81.139.2. URL https://link.aps.org/doi/10.1103/PhysRev.81.139.2.

[185] C. B. Samantaray and R. N. Singh. Review of synthesis and properties of cubic boron nitride (c-bn) thin films. *International Materials Reviews*, 50 (6):313–344, 2005. doi: 10.1179/174328005X67160. URL https://doi.org/10.1179/174328005X67160.

[186] Nocona Sanders and Emmanouil Kioupakis. Phonon- and defect-limited electron and hole mobility of diamond and cubic boron nitride: A critical comparison. *Applied Physics Letters*, 119(6):062101, 08 2021. ISSN 0003-6951. doi: 10.1063/5.0056543. URL https://doi.org/10.1063/5.0056543.

[187] Wataru Sasaki, Motoichi Shibuya, and Kanji Mizuguchi. Anisotropy of Hot Electrons in n-type Germanium. *Journal of the Physical Society of Japan*, 13(5):456–460, May 1958. doi: 10.1143/JPSJ.13.456.

[188] John R. Schaibley, Hongyi Yu, Genevieve Clark, Pasqual Rivera, Jason S. Ross, Kyle L. Seyler, Wang Yao, and Xiaodong Xu. Valleytronics in 2d materials. *Nature Reviews Materials*, 1(11):16055, 2016. doi: 10.1038/natrevmats.2016.55. URL https://doi.org/10.1038/natrevmats.2016.55.

[189] K.J. Schmidt-Tiedemann. Conductivity anisotropy of hot electrons in n-type silicon heated by microwave fields. *Philips Research Reports*, 18:338–360, 1963.

[190] Zoya Mehmood Shah and Alison Mainwood. A theoretical study of the effect of nitrogen, boron and phosphorus impurities on the growth and morphology of diamond surfaces. *Diamond and Related Materials*, 17(7):1307–1310, 2008. ISSN 0925-9635. doi: https://doi.org/10.1016/j.diamond.2008.03.028. URL https://www.sciencedirect.com/science/article/pii/S0925963508002604. Proceedings of Diamond 2007, the 18th European Conference on Diamond, Diamond-Like Materials, Carbon Nanotubes, Nitrides and Silicon Carbide.

[191] Wei Shen, Shengnan Shen, Sheng Liu, Hui Li, Zhiyin Gan, and Qiaoxuan Zhang. Monolayer cubic boron nitride terminated diamond (111) surfaces for quantum sensing and electron emission applications. *ACS Applied Materials & Interfaces*, 12(29):33336–33345, 07 2020. doi: 10.1021/acsami.0c05268. URL https://doi.org/10.1021/acsami.0c05268.

[192] Motoichi Shibuya. Hot electron problem in semiconductors with spheroidal energy surfaces. *Phys. Rev.*, 99:1189–1191, Aug 1955. doi: 10.1103/PhysRev.99.1189. URL https://link.aps.org/doi/10.1103/PhysRev.99.1189.

[193] W. Shockley and J. Bardeen. Energy bands and mobilities in monatomic semiconductors. *Phys. Rev.*, 77:407–408, Feb 1950. doi: 10.1103/PhysRev.77.407. URL https://link.aps.org/doi/10.1103/PhysRev.77.407.

[194] W Shockley, John A Copeland, and RP James. Quantum theory of atoms, molecules and the solid state. *New York: Academic*, 537, 1966.

[195] Poppy Siddiqua, Michael S. Shur, and Stephen K. O'Leary. Electron transport within bulk cubic boron nitride: A Monte Carlo simulation analysis. *Journal of Applied Physics*, 128(18):185704, 11 2020. ISSN 0021-8979. doi: 10.1063/5.0013183. URL https://doi.org/10.1063/5.0013183.

[196] A. Soltani, H. A. Barkad, M. Mattalah, B. Benbakhti, J.-C. De Jaeger, Y. M. Chong, Y. S. Zou, W. J. Zhang, S. T. Lee, A. BenMoussa, B. Giordanengo, and J.-F. Hochedez. 193nm deep-ultraviolet solar-blind cubic boron nitride based photodetectors. *Applied Physics Letters*, 92(5):053501, 02 2008. ISSN 0003-6951. doi: 10.1063/1.2840178. URL https://doi.org/10.1063/1.2840178.

[197] Christopher J. Stanton and John W. Wilkins. Nonequilibrium current fluctuations in semiconductors: A boltzmann-equation–green-function approach. *Phys. Rev. B*, 35:9722–9734, Jun 1987. doi: 10.1103/PhysRevB.35.9722. URL https://link.aps.org/doi/10.1103/PhysRevB.35.9722.

[198] Christopher J. Stanton and John W. Wilkins. Hot-electron noise in two-valley semiconductors: An analytic model. *Phys. Rev. B*, 36:1686–1695, Jul 1987. doi: 10.1103/PhysRevB.36.1686. URL https://link.aps.org/doi/10.1103/PhysRevB.36.1686.

[199] R A Stradling and R A Wood. The magnetophonon effect in III-v semiconducting compounds. *Journal of Physics C: Solid State Physics*, 1(6): 1711–1733, dec 1968. doi: 10.1088/0022-3719/1/6/330. URL https://doi.org/10.1088/0022-3719/1/6/330.

[200] Jiace Sun and Austin J. Minnich. Transport and noise of hot electrons in gaas using a semianalytical model of two-phonon polar optical phonon scattering. *Phys. Rev. B*, 107:205201, May 2023. doi: 10.1103/PhysRevB.107.205201. URL https://link.aps.org/doi/10.1103/PhysRevB.107.205201.

[201] Jifeng Sun, Hongliang Shi, Theo Siegrist, and David J. Singh. Electronic, transport, and optical properties of bulk and mono-layer pdse2. *Applied Physics Letters*, 107(15):153902, 2015. doi: 10.1063/1.4933302. URL https://doi.org/10.1063/1.4933302.

[202] N. Suntornwipat, S. Majdi, M. Gabrysch, and J. Isberg. Investigation of transferred-electron oscillations in diamond. *Applied Physics Letters*, 108 (21):212104, 05 2016. ISSN 0003-6951. doi: 10.1063/1.4952766. URL https://doi.org/10.1063/1.4952766.

[203] Nattakarn Suntornwipat, Saman Majdi, Markus Gabrysch, Kiran Kumar Kovi, Viktor Djurberg, Ian Friel, Daniel J. Twitchen, and Jan Isberg. A valleytronic diamond transistor: Electrostatic control of valley currents and charge-state manipulation of nv centers. *Nano Letters*, 21(1):868–874, 01 2021. doi: 10.1021/acs.nanolett.0c04712. URL https://doi.org/10.1021/acs.nanolett.0c04712.

[204] Takashi Taniguchi, Tokuyuki Teraji, Satoshi Koizumi, Kenji Watanabe, and Shinobu Yamaoka. Appearance of n-type semiconducting properties of cbn single crystals grown at high pressure. *Japanese Journal of Applied Physics*, 41(2A):L109, feb 2002. doi: 10.1143/JJAP.41.L109. URL https://dx.doi.org/10.1143/JJAP.41.L109.

[205] Takashi Taniguchi, Satoshi Koizumi, Kenji Watanabe, Isao Sakaguchi, Takashi Sekiguchi, and Shinobu Yamaoka. High pressure synthesis of uv-light emitting cubic boron nitride single crystals. *Diamond and Related Materials*, 12(3):1098–1102, 2003. ISSN 0925-9635. doi: https://doi.org/10.1016/S0925-9635(02)00330-8. URL https://www.sciencedirect.com/science/article/pii/S0925963502003308. 13th European Conference on Diamond, Diamond-Like Materials, Carbon Nanotubes, Nitrides and Silicon Carbide.

[206] Paul A. Temple and C. E. Hathaway. Multiphonon raman spectrum of silicon. *Phys. Rev. B*, 7:3685–3697, Apr 1973. doi: 10.1103/PhysRevB.7.3685. URL https://link.aps.org/doi/10.1103/PhysRevB.7.3685.

[207] P. Thomas and H. J. Queisser. Electron-phonon coupling in the barriers of gaas schottky diodes. *Phys. Rev.*, 175:983–984, Nov 1968. doi:

10.1103/PhysRev.175.983. URL https://link.aps.org/doi/10.1103/PhysRev.175.983.

[208] S.E. Thompson, M. Armstrong, C. Auth, M. Alavi, M. Buehler, R. Chau, S. Cea, T. Ghani, G. Glass, T. Hoffman, C.-H. Jan, C. Kenyon, J. Klaus, K. Kuhn, Zhiyong Ma, B. Mcintyre, K. Mistry, A. Murthy, B. Obradovic, R. Nagisetty, Phi Nguyen, S. Sivakumar, R. Shaheed, L. Shifren, B. Tufts, S. Tyagi, M. Bohr, and Y. El-Mansy. A 90-nm logic technology featuring strained-silicon. *IEEE Transactions on Electron Devices*, 51(11):1790–1797, 2004. doi: 10.1109/TED.2004.836648.

[209] Xiao Tong and Marco Bernardi. Toward precise simulations of the coupled ultrafast dynamics of electrons and atomic vibrations in materials. *Phys. Rev. Res.*, 3:023072, Apr 2021. doi: 10.1103/PhysRevResearch.3.023072. URL https://link.aps.org/doi/10.1103/PhysRevResearch.3.023072.

[210] J. Y. Tsao, S. Chowdhury, M. A. Hollis, D. Jena, N. M. Johnson, K. A. Jones, R. J. Kaplar, S. Rajan, C. G. Van de Walle, E. Bellotti, C. L. Chua, R. Collazo, M. E. Coltrin, J. A. Cooper, K. R. Evans, S. Graham, T. A. Grotjohn, E. R. Heller, M. Higashiwaki, M. S. Islam, P. W. Juodawlkis, M. A. Khan, A. D. Koehler, J. H. Leach, U. K. Mishra, R. J. Nemanich, R. C. N. Pilawa-Podgurski, J. B. Shealy, Z. Sitar, M. J. Tadjer, A. F. Witulski, M. Wraback, and J. A. Simmons. Ultrawide-bandgap semiconductors: Research opportunities and challenges. *Advanced Electronic Materials*, 4(1): 1600501, 2018. doi: https://doi.org/10.1002/aelm.201600501. URL https://onlinelibrary.wiley.com/doi/abs/10.1002/aelm.201600501.

[211] Steven A. Vitale, Daniel Nezich, Joseph O. Varghese, Philip Kim, Nuh Gedik, Pablo Jarillo-Herrero, Di Xiao, and Mordechai Rothschild. Valleytronics: Opportunities, challenges, and paths forward. *Small*, 14(38): 1801483, 2018. doi: https://doi.org/10.1002/smll.201801483. URL https://onlinelibrary.wiley.com/doi/abs/10.1002/smll.201801483.

[212] Cheng-Xin Wang, Guo-Wei Yang, Tie-Chen Zhang, Hong-Wu Liu, Yong-Hao Han, Ji-Feng Luo, Chun-Xiao Gao, and Guang-Tian Zou. High-quality heterojunction between p-type diamond single-crystal film and n-type cubic boron nitride bulk single crystal. *Applied Physics Letters*, 83(23):4854–4856, 12 2003. ISSN 0003-6951. doi: 10.1063/1.1631059. URL https://doi.org/10.1063/1.1631059.

[213] Shulong Wang, Hongxia Liu, Bo Gao, and Huimin Cai. Monte Carlo calculation of electron diffusion coefficient in wurtzite indium nitride. *Applied Physics Letters*, 100(14):142105, 04 2012. ISSN 0003-6951. doi: 10.1063/1.3700720. URL https://doi.org/10.1063/1.3700720.

[214] Jr. Wentorf, R. H. Cubic Form of Boron Nitride. *The Journal of Chemical Physics*, 26(4):956–956, 04 1957. ISSN 0021-9606. doi: 10.1063/1.1745964. URL https://doi.org/10.1063/1.1745964.

[215] Kongping Wu, Liyong Gan, Leng Zhang, Pengzhan Zhang, Fei Liu, Jing Fan, Liwen Sang, and Meiyong Liao. Generating robust two-dimensional hole gas at the interface between boron nitride and diamond. *Japanese Journal of Applied Physics*, 59(9):090910, sep 2020. doi: 10.35848/1347-4065/abb20c. URL https://dx.doi.org/10.35848/1347-4065/abb20c.

[216] D. Y. Xing, M. Liu, and C. S. Ting. Analytical approach to diffusion of hot carriers in n-type gaas with Γ-l-x band structure. *Phys. Rev. B*, 37: 10283–10294, Jun 1988. doi: 10.1103/PhysRevB.37.10283. URL https://link.aps.org/doi/10.1103/PhysRevB.37.10283.

[217] Mingfei Xu, Dawei Wang, Kai Fu, Dinusha Herath Mudiyanselage, Houqiang Fu, and Yuji Zhao. A review of ultrawide bandgap materials: properties, synthesis and devices. *Oxford Open Materials Science*, 2(1):itac004, 05 2022. ISSN 2633-6979. doi: 10.1093/oxfmat/itac004. URL https://doi.org/10.1093/oxfmat/itac004.

[218] Hangsheng Yang, Aili Chen, and Famin Qiu. Cubic boron nitride film residual compressive stress relaxation by post annealing. *Diamond and Related Materials*, 20(8):1179–1182, 2011. ISSN 0925-9635. doi: https://doi.org/10.1016/j.diamond.2011.07.003. URL https://www.sciencedirect.com/science/article/pii/S0925963511002226.

[219] Max N Yoder. Wide bandgap semiconductor materials and devices. *IEEE Transactions on Electron Devices*, 43(10):1633–1636, 1996.

[220] W. J. Zhang, X. M. Meng, C. Y. Chan, K. M. Chan, Y. Wu, I. Bello, and S. T. Lee. Interfacial study of cubic boron nitride films deposited on diamond. *The Journal of Physical Chemistry B*, 109(33):16005–16010, 08 2005. doi: 10.1021/jp0517908. URL https://doi.org/10.1021/jp0517908.

[221] X.W. Zhang. Doping and electrical properties of cubic boron nitride thin films: A critical review. *Thin Solid Films*, 544:2–12, 2013. ISSN 0040-6090. doi: https://doi.org/10.1016/j.tsf.2013.07.001. URL https://www.sciencedirect.com/science/article/pii/S0040609013011681. The 6th International Conference on Technological Advances of Thin Films & Surface Coatings.

[222] Jin-Jian Zhou and Marco Bernardi. Ab initio electron mobility and polar phonon scattering in gaas. *Phys. Rev. B*, 94:201201, Nov 2016. doi: 10.1103/PhysRevB.94.201201. URL https://link.aps.org/doi/10.1103/PhysRevB.94.201201.

[223] Jin-Jian Zhou, Jinsoo Park, I-Te Lu, Ivan Maliyov, Xiao Tong, and Marco Bernardi. Perturbo: A software package for ab initio electron–phonon interactions, charge transport and ultrafast dynamics. *Computer Physics Communications*, 264:107970, 2021. ISSN 0010-4655. doi: https://doi.org/10.1016/

j.cpc.2021.107970. URL https://www.sciencedirect.com/science/article/pii/S0010465521000837.

[224] M. Zhu, M. Matsubara, and E. Bellotti. Carrier transport in cubic boron nitride: First-principles and semiempirical models. *Phys. Rev. Appl.*, 20: 034055, Sep 2023. doi: 10.1103/PhysRevApplied.20.034055. URL https://link.aps.org/doi/10.1103/PhysRevApplied.20.034055.

[225] J.W. Ziman. *Electrons and Phonons: The Theory of Transport Phenomena in Solids*. Oxford University Press, Oxford, 1960.